

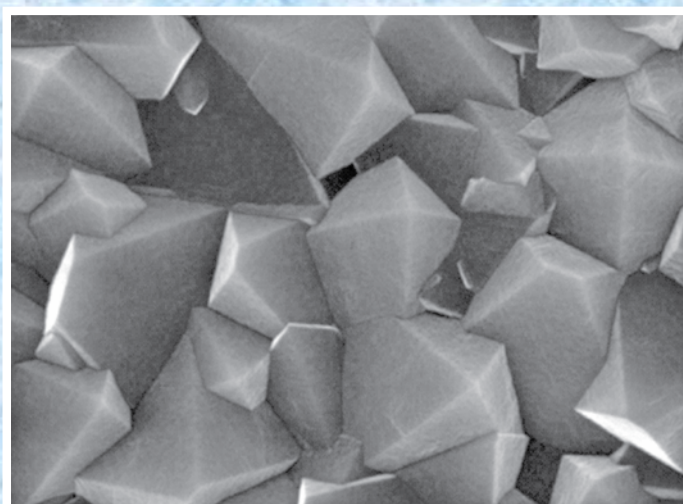
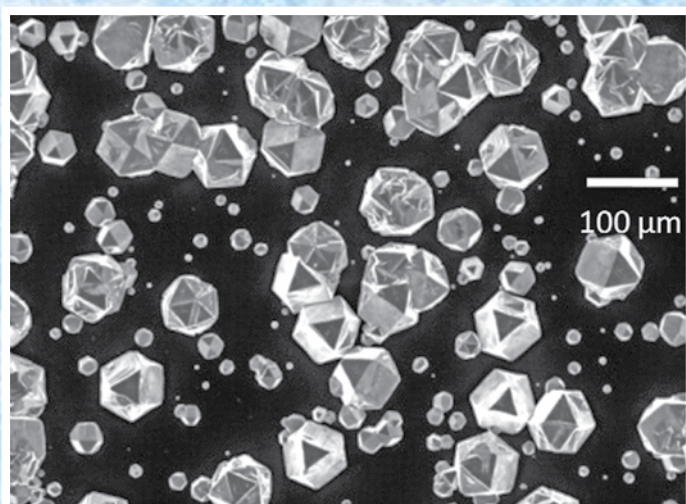
SMC Bulletin

A Publication of the Society for Materials Chemistry

Volume 5

No. 1

April 2014



Society for Materials Chemistry

Society for Materials Chemistry was mooted in 2007 with following aims and objectives:

- (a) to help the advancement, dissemination and application of the knowledge in the field of materials chemistry,
- (b) to promote active interaction among all material scientists, bodies, institutions and industries interested in achieving the advancement, dissemination and application of the knowledge of materials chemistry,
- (c) to disseminate information in the field of materials chemistry by publication of bulletins, reports, newsletters, journals.
- (d) to provide a common platform to young researchers and active scientists by arranging seminars, lectures, workshops, conferences on current research topics in the area of materials chemistry,
- (e) to provide financial and other assistance to needy deserving researchers for participation to present their work in symposia, conference, etc.
- (f) to provide an incentive by way of cash awards to researchers for best thesis, best paper published in journal/national/international conferences for the advancement of materials chemistry,
- (g) to undertake and execute all other acts as mentioned in the constitution of SMC.

Executive Committee

President

Dr. S. K. Sarkar

Bhabha Atomic Research Centre
Trombay, Mumbai, 400 085
sarkarsk@barc.gov.in

Vice-Presidents

Dr. V. K. Jain

Bhabha Atomic Research Centre
Trombay, Mumbai, 400 085
jainvk@barc.gov.in

Prof. Sandeep Verma

Indian Institute of Technology
Kanpur
sverma@iitk.ac.in

Secretary

Dr. P. A. Hassan

Bhabha Atomic Research Centre
Trombay, Mumbai, 400 085
hassan@barc.gov.in

Treasurer

Dr. Sandeep Nigam

Bhabha Atomic Research Centre
Trombay, Mumbai, 400 085
snigam@barc.gov.in

Members

Dr. K. Ananthasivan

Indira Gandhi Centre for Atomic Research
Kalpakkam, 603102

Dr. (Smt.) A. Banerjee

Bhabha Atomic Research Centre
Trombay, Mumbai-400085

Dr. K. Bhattacharya

Bhabha Atomic Research Centre
Trombay, Mumbai-400085

Dr. D. Das

Bhabha Atomic Research Centre
Trombay, Mumbai-400085

Dr. G. K. Dey

Bhabha Atomic Research Centre
Trombay, Mumbai-400085

Dr. P. Sujata Devi

CSIR Central Glass & Ceramic Research
Institute, Kolkata-700032

Dr. C. P. Kaushik

Bhabha Atomic Research Centre
Trombay, Mumbai-400085

Dr. T. Mukherjee

Bhabha Atomic Research Centre
Trombay, Mumbai-400085

Dr. M. C. Rath

Bhabha Atomic Research Centre
Trombay, Mumbai-400085

Dr. (Smt.) S. S. Rayalu

CSIR National Environmental
Engineering Research Institute, Nagapur

Prof. S. D. Samant

Institute of Chemical Technology
Mumbai

Dr. A. K. Tyagi

Bhabha Atomic Research Centre
Trombay, Mumbai-400085

Dr. R. K. Vatsa

Bhabha Atomic Research Centre
Trombay, Mumbai-400085

Co-opted Members

Prof. A. Ajayaghosh

CSIR – National Institute for
Interdisciplinary Science and Technology
Thiruvananthapuram
ajayaghosh@niist.res.in

Prof. A. K. Ganguli

Director, Institute for Nanoscience and
Technology
ashok@chemistry.iitd.ernet.in

Prof. S. Ram

Indian Institute of Technology - Kharagpur
sram @ matsc.iitkgp.ernet.in

Dr. A. K. Tripathi

Bhabha Atomic Research Centre
Trombay, Mumbai-400085
catal@barc.gov.in

Contact address

Society for Materials Chemistry

C/o Chemistry Division

Bhabha Atomic Research Centre, Trombay, Mumbai, 400 085, India

Tel: +91-22-25592001, E-mail: socmatchem@gmail.com

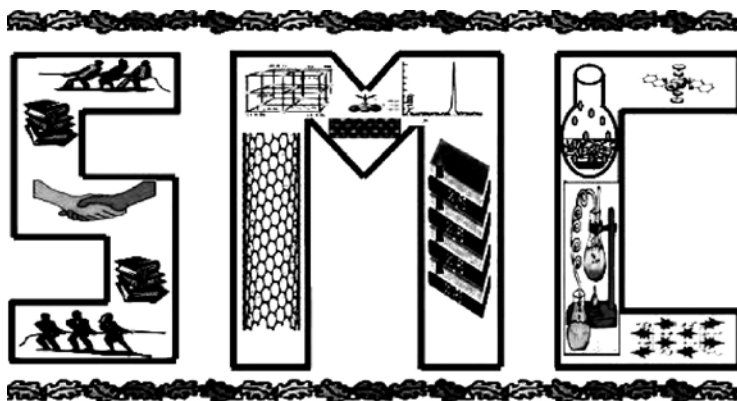
SMC Bulletin

A Publication of the Society for Materials Chemistry

Volume 5

No. 1

April 2014



SOCIETY FOR MATERIALS CHEMISTRY

SMC Bulletin

Vol. 5

No. 1

April 2014

Guest Editors

Dr. Ramani Venugopalan
Powder Metallurgy Division,
Bhabha Atomic Research Centre,
Trombay, Mumbai 400085
e-mail: rvg@barc.gov.in

Dr. V. Sudarsan
Chemistry Division
Bhabha Atomic Research Centre,
Trombay, Mumbai 400085
e-mail: vsudar@barc.gov.in

Editorial Board

Dr. Arvind Kumar Tripathi
Chemistry Division
Bhabha Atomic Research Centre
Trombay, Mumbai, 400 085
e-mail: catal@barc.gov.in

Dr. Shyamala Bharadwaj
Chemistry Division
Bhabha Atomic Research Centre
Trombay, Mumbai, 400 085
e-mail: shyamala@barc.gov.in

Dr. Manidipa Basu
Chemistry Division
Bhabha Atomic Research Centre
Trombay, Mumbai, 400 085
e-mail: deepa@barc.gov.in

Dr. Aparna Banerjee
Product Development Division
Bhabha Atomic Research Centre
Trombay, Mumbai, 400 085
e-mail: aparnab@barc.gov.in

Dr. Sandeep Nigam
Chemistry Division
Bhabha Atomic Research Centre
Trombay, Mumbai, 400 085
e-mail: snigam@barc.gov.in

Published by

Society for Materials Chemistry
C/o. Chemistry Division
Bhabha Atomic Research Centre, Trombay, Mumbai, 400 085
E-mail: socmatchem@gmail.com,
Tel: +91-22-25592001

Please note that the authors of the paper are alone responsible for the technical contents of papers and references cited therein

Front cover shows SEM micrographs of diamond crystals during nucleation and growth stage

Guest Editorial



Ramani Venugopalan



V. Sudarsan

As guest editors, we are extremely happy to be associated with this thematic issue of SMC bulletin on “Carbon based Materials”. Carbon is one of the most important elements in the periodic table as all the living organisms are made of carbon. There are many allotropic forms of carbon: diamond and graphite being the oldest known among them. The other allotropic forms include fullerenes, carbon nano-tubes (CNTs) graphene, mesoporus carbons etc. Wide difference in the physico-chemical properties of different allotropic forms of carbon is responsible for the significant interest in the field of carbon based materials by researchers all over the world. Considerable extent of work has been carried out on carbon based materials in the recent past. Applications of carbon based materials in the field of super-capacitors and hydrogen storage technology are of worth mentioning. Carbon based materials are going to find immense applications in upcoming nuclear reactors also, such as Compact High Temperature Reactors (CHTR).

Keeping in mind the current research activities on carbon based materials, this issue of SMC bulletin covers topics like use of carbon based materials for high temperature structural materials, porous carbon as adsorbent materials for gaseous and liquid molecules, synthesis and characterisation of diamond thin films, applications of silicon carbide and other novel carbon composites in nuclear technology. In addition to this, studies on fundamental aspects such as interaction of π - electrons of fullerene fragments like corannulene ($C_{20}H_{10}$) and sumanene ($C_{21}H_{12}$) with alkali/alkaline earth metal ions is covered in this bulletin. Since, Raman spectroscopic technique is extensively used to characterize carbon related materials, a chapter dealing with Raman spectroscopic studies on carbon based materials is also included in this bulletin. The editors thank all the authors of this bulletin for their valuable contributions.

From the desks of the President and Secretary



Dr. Sisir K Sarkar
President



Dr. P. A. Hassan
Secretary

Dear Fellow Members and Readers,

Greetings from SMC!

As you all know, the excellent tradition of periodic publication of thematic bulletins by SMC has received overwhelming appreciation from its fellow members and the chemistry community. Considering the importance of carbon in everyday life and the recent thrust in proliferating applications of new forms of carbon such as graphene, nanotubes etc, we decided to have an issue on “Carbon based Materials”. We take great pride in presenting this issue which has been edited by our colleagues Dr. V. Sudarsan and Dr. Ramani Venugopalan.

Carbon is omnipresent and a plethora of carbon allotropes such as fullerenes, nanotubes, graphenes etc., are gaining increasing attention in future technologies. Graphene is a single layer of graphite and is the newest member of the nanocarbon family. The continuous network of hexagonally arranged carbon atoms gives rise to some exceptional electronic, mechanical, and thermal properties, which could see the application of graphene in new generation electronic components, energy-storage materials such as capacitors and batteries, polymer nano-composites, transparent conducting electrodes, and mechanical resonators. The discovery of new forms of carbon and its composites with tunable properties has stimulated extensive research in this field. This issue brings together some of the recent advances in the area of carbon based materials with special emphasis on high strength composites, porous carbon materials, diamond thin films, silicon carbide materials, inorganic-organic cation- π complexes and finally carbon reinforced composite materials for nuclear applications. We put on record our sincere thanks to all contributing authors and guest editors for their dedicated efforts for timely publication of this issue.

We extend our gratitude to all SMC members for their support and cooperation.

(President)

(Secretary)

CONTENTS

	Feature articles	Page No.
1.	Carbon Composite Materials for high temperature Structural applications <i>L. M. Manocha</i>	1
2.	Micro to Macroporous Carbon Materials <i>Satish M. Manocha</i>	8
3.	Chemical Vapor Deposited Diamond Thin Films: A Brief Overview on Synthesis and Characterization <i>J. Nuwad, Dheeraj Jain, C. G. S. Pillai and V. Sudarsan</i>	15
4.	Raman Spectroscopic Studies of Carbon Related Materials <i>Dattatray J. Late and Mukesh Pandey</i>	26
5.	Silicon Carbide Research and Development in Nuclear Industry: Silicon Carbide on Graphite Rod by Induction Assisted Chemical Vapor Deposition process using Hexamethyldisilane (HMDS) as a Single Source. <i>J. Selvakumar, K. Ramadurai, D. Sathiyamoorthy</i>	35
6.	Novel Carbon Composites for Nuclear Application <i>Ramani Venugopalan, Kinshuk Dasgupta, Mainak Roy and A. K. Tyagi</i>	46
7.	Structures and energetics of alkali and alkaline earth metal ion complexes of sumanene and corannulene: A systematic understanding of cation-π interactions <i>Chinagandham Rajesh and Chiranjib Majumder</i>	52

Carbon Composite Materials for high temperature Structural applications

L. M. Manocha

Department of Materials Science, Sardar Patel University,

Vallabh Vidyanagar - 388120

E-mail: manocha52@rediffmail.com

Abstract

Carbon products are used for various applications in electrical, thermal and structural sectors. It has been possible because these solid carbons can be made in various forms from hard to ductile and with desired physical, surface, thermal and electrical properties by choosing appropriate raw materials, reinforcements and binders or controlling their microstructure at nano level or making them nanocrystalline materials. Even the thermal stability of the carbons can be enhanced through control of microstructure or by giving suitable coatings so that we have a series of carbon/carbon composites coated with ceramics or carbon-ceramics with high operating temperature capabilities for turbine engines and aircrafts. These aspects in the form of carbon-composites have enhanced the application sectors of current applications. Various types of solid carbon and carbon-ceramic composites have been illustrated.

Introduction

Carbon and graphite products in amorphous and polycrystalline form and in technical terms, engineered carbons are since long been used for applications in diverse sectors, especially as electrodes in metallurgy such as anodes for steel industry, cathodes for aluminium industries etc; high temperature dies, tribo components as brakes for aircrafts and heavy duty transports, mechanical carbons, electrodes for batteries, structural components for nuclear reactors, adsorbents and lubrication etc. [1]. These are also known for thermal applications relating heat conduction as well as thermal insulation, environmental applications in the form of activated carbon and biomedical applications as implants. This is because of its unique characteristics such as light weight, high temperature stability (without loss of strength) up to $\sim 2500^{\circ}\text{C}$ in non-oxidizing atmospheres, low coefficient of thermal expansion and controlled friction, good electrical and thermal conductivities and high thermal shock resistance. [2-4]

These types of carbons are produced industrially like ceramics in an artificial process. Fig. 1 shows the schematic of processing of engineering carbons. The bulk amorphous carbons and polycrystalline graphite consist of agglomeration of smaller graphite crystallites into a three dimensional mosaic network. The bulk properties of this material depend on the size of the crystallites, their orientation with respect to each other within the mosaic structure, and crystallite perfections. In fact, industrial carbons are a class of composite materials, usually composed of more than 10 different constituents categorized into four main classes: - binders, fillers, modifiers, and abrasives [5, 6]. Selection of the

constituents is often based on experience or a trial and error method to make new formulation. Phenolic resins and pitches are among the most commonly used binders in these materials. In the class of fillers, graphite powder, coke, fly ash etc are used. Abrasives like alumina, oxides, iron oxide, silica, SiC and boron carbide are incorporated to improve the mechanical properties [2, 7, 8]. Therefore, these are also called particulate carbon composites. The bulk properties of the material can be altered by modifying crystallographic parameters of any of these phases. As a result, the bulk properties can be tailored to fit specific needs.

Table 1. Properties of Pitch based carbon fibers used for carbon/carbon composites

Property	Low modulus	High modulus	Ultra-high modulus
Tensile modulus, GPa	170-241	380-620	690-965
Tensile strength, MPa	1380-3100	1900-2750	2410
Electrical Resistivity, $\mu \Omega \text{ cm}$	1300	900	220-130
Thermal Conductivity, W/mK	-	-	400-1100
Coefficient of thermal expansion in axial direction, 10^{-6} K	-	-0.9	-0.6
Density, gm/cc	1.9	2.0	2.2
Carbon content, %	+97	+99	+99

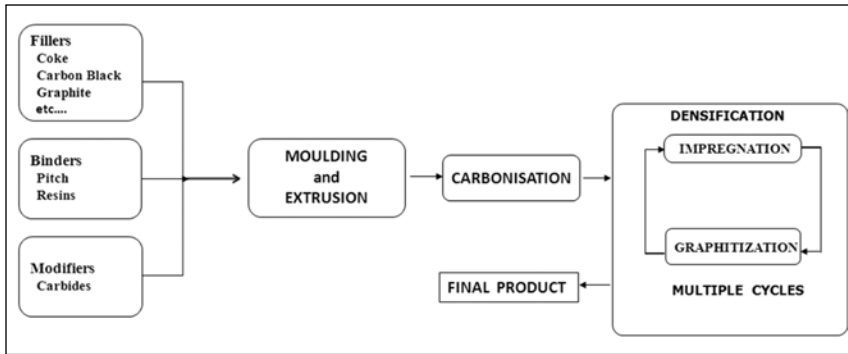


Fig.1. Processing of Industrial Solid Carbon products Pitch based carbons Phenolic resin based carbons

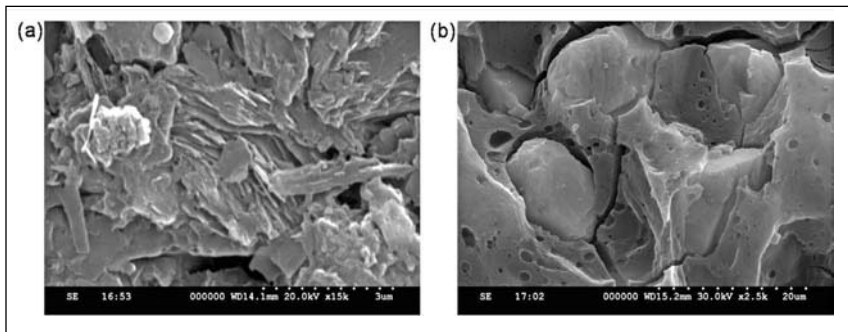


Fig. 2. Macrostructure Pitch/Resin based carbon products

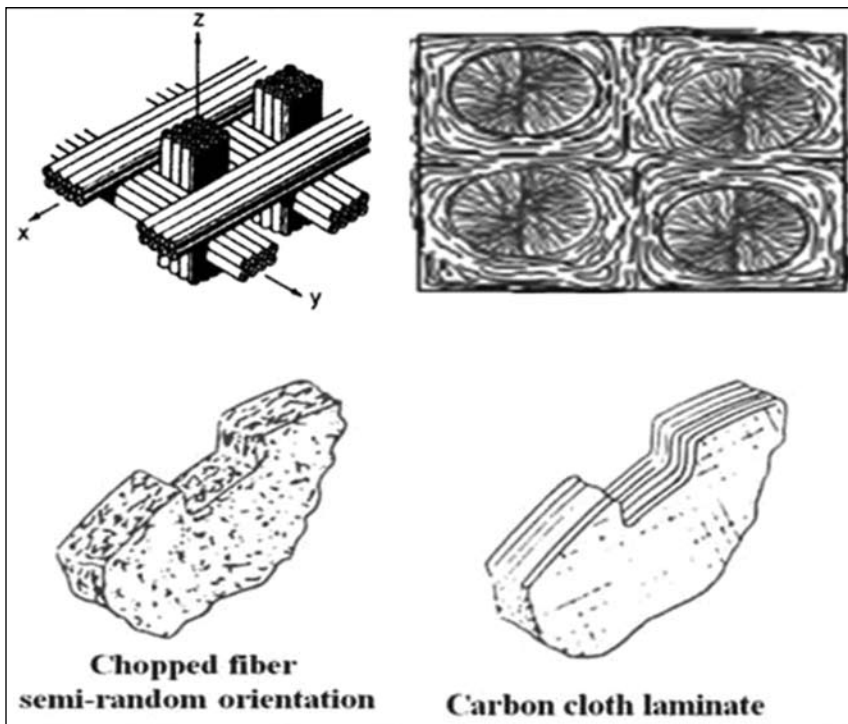


Fig. 3. Carbon fiber architecture and carbon matrix oriented around carbon fibers in Carbon/carbon composites

Macrostructure (density, porosity, filler distribution) and microstructure (crystallinity and anisotropy predominantly of binder carbons) predominantly depend on

the type of binder precursor (thermoplastic pitch or thermosetting phenolic resins) and heat treatment temperature. This is depicted in Fig. 2. Fig. 2a, the pitch based crystalline carbon materials possess high electrical and thermal conductivities than phenolic based carbons (Fig.2b). A lot of studies have been undertaken to develop different types of carbon based composites with different formulations their characterization with respect to mechanical and thermal properties and constituents to study the effect of above mentioned constituents on their microstructural properties [7-9].

Carbon Fiber Composites

Even with best choice of the fillers and binders, the normal bulk synthetic graphite products exhibit less than 2-4% of the theoretical strength. Therefore, since long there has been quest for the scientists to explore and achieve maximum possible strength in carbon materials. This coupled with the requirement of high performance reinforcing fibers for composite materials lead to the development of carbon fibers. This revolution in carbon history in late 1950s in the form of the development of carbon fibers revolutionized the composites industry and high performance materials structural applications [10]. Carbon fiber is a thin, about 5-10 micron diameter, long filament composed mostly of carbon atoms. The carbon atoms are bonded together in microscopic crystals that are more or less aligned parallel to the long axis of the fiber. The crystal alignment makes the fiber incredibly strong. Thousands of such filaments are put together in the form of roving or tow. Carbon composites initially intended for aerospace industries have moved rapidly to industrial sectors [11].

In order to make best use of their exciting properties, carbon fibers, both filament and fabric form, are usually combined with other materials to form a composite. When

combined with a plastic resin and wound or molded it forms carbon fiber reinforced plastic which has a very high strength-to-weight, extremely rigid, although somewhat brittle material. However, carbon fibers are also mixed

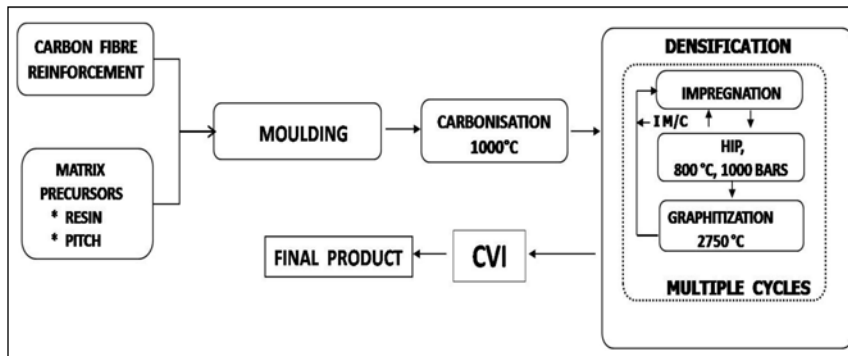


Fig.4. Schematic representation of processing of carbon/carbon composites

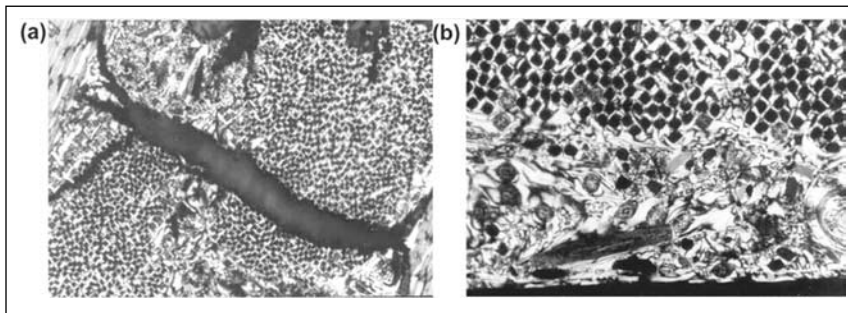


Fig.5. Optical Macrostructure of pitch derived carbon/carbon composites

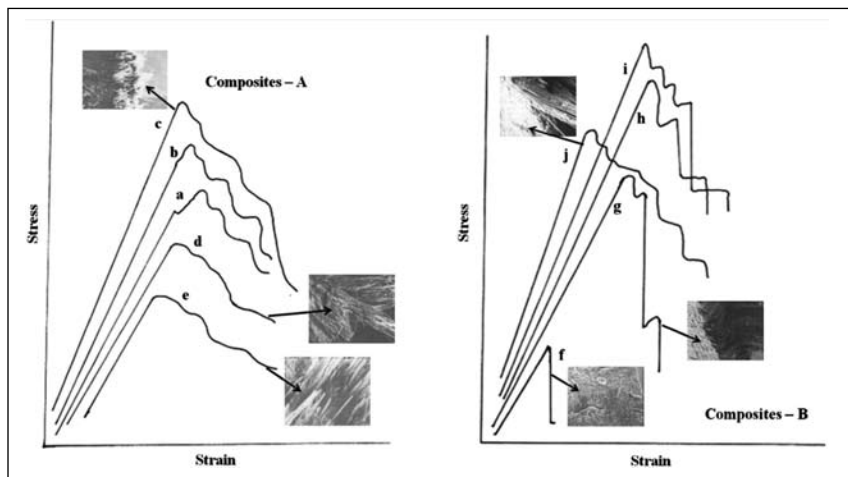


Fig. 6. Stress strain behavior and fracture of Carbon /Carbon composites heat treated to high temperatures made with (A) weak fiber/matrix bonding & (B) strong fiber/matrix bonding

with other materials, such as with graphite to form carbon-carbon composites, which have a very high heat tolerance [12-13]. Though carbon fibers are major reinforcements for polymeric, carbon and ceramic matrix composites, the present paper is restricted to carbon matrix composites.

Latest trends in carbon composites have been to alter the fiber/matrix interactions through incorporation of carbon nanomaterials, especially by using functional carbon nanotubes to develop nano-modified carbon composites with improved fracture toughness and reduced impact

damage. Furthermore, highly specialized processing techniques are necessary for fabrication of advanced composites.

Processing of Carbon-carbon composites

Carbon-carbon composites, as the name suggests, consist of highly-ordered carbon fibers embedded in a carbon matrix with carbon fibers used in different forms and layed in different direction as shown in Fig. 3. Like conventional carbon products, there are basic two routes to create carbon matrix in carbon-carbon composites: through gaseous route, i.e., chemical vapor deposition (CVD/CVI) and through carbonaceous precursors, i.e., a series of liquid impregnation and pyrolysis (LIP) steps using thermosetting resins (Phenolics, PFA etc.) or thermoplastic pitches (coal tar pitch or petroleum pitch) as carbon precursors (Fig. 4) [13,14].

For most of the carbon-carbon applications, 2D composites are made using layup techniques conventionally used in polymer composites. 2D structures are usually formed from several layers of woven carbon fabric with or without stitching or needle punching in third direction with carbon fibers to give structural strength as well as balanced thermal properties.

Chemical vapor infiltration/deposition (CVI/CVD) processing involves infiltration of gaseous hydrocarbons into the porous preforms followed by cracking of these gases resulting in densification of the porous carbon fiber preforms with carbon matrix. The densification of porous carbon composites structures can be achieved through vapor phase infiltration (CVI)

wherein the hydrocarbon gases such as methane, propane etc. infiltrate into porous fibrous structure heated to a temperature of 1000-1400°C and are made to crack therein. Commercially, isothermally heated stack of components are impregnated simultaneously in a large size furnace. In variance with the slow and complex conventional isothermal heating method, alternative methods of forced-flow/thermal gradient processes have been developed for building up the carbon matrix around carbon fibers. Carbon-bearing propylene, propane or methane is forced under pressure through the preform while it is heated in an oven at 1200°C [15].

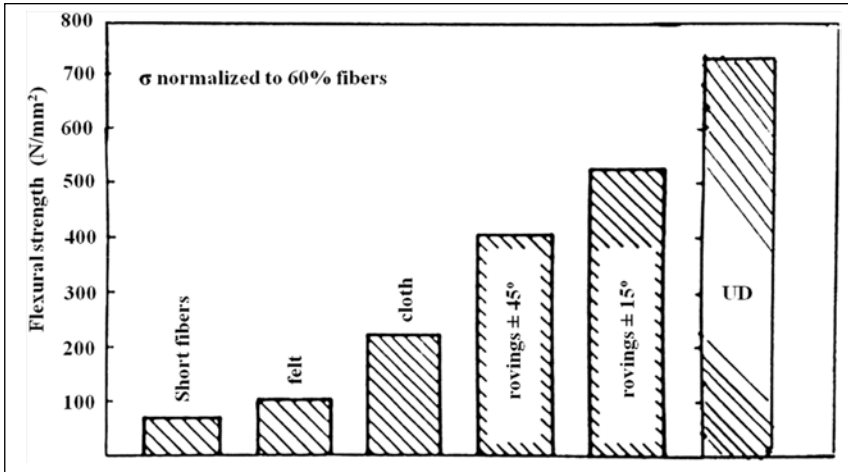


Fig. 7. Mechanical properties of densified Carbon/Carbon composites with different fiber architecture

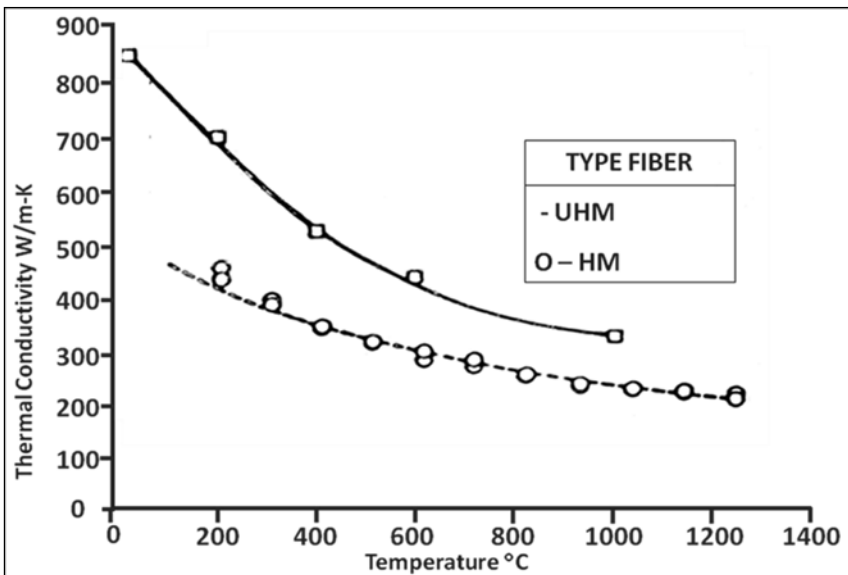


Fig. 8. Thermal conductivity of carbon/carbon composites with HM (high modulus) and UHM (Ultra high modulus carbon fibers)

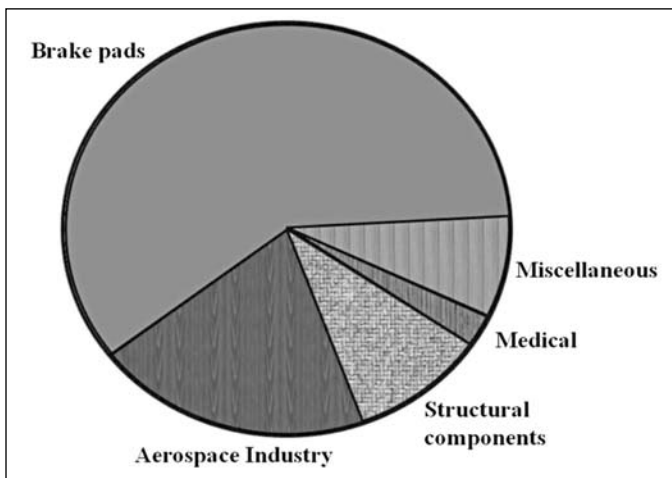


Fig. 9. General trend of carbon/Carbon composites applications

Porous structures can also be impregnated with liquid phase pitch/phenolic resin followed by carbonization and high temperature heat treatment (1000-2700°C). The porous fibrous performs or the porous carbonized composites are evacuated followed by infiltration with liquid resin/pitch and pressurized. The pyrolysis of the pitch /resin infiltrated composites is done either under normal pressure or high pressure (HIP). The interest got generated to develop C/Cs with these carbon nanomaterials as third-phase material. These combinations result in improved thermal properties of the composites in transverse directions as well. However, proper distribution of these nanomaterials in the resins/pitches is a major task.

Many times, a combination of processing routes (LIP & CVD) are used. These comprise fabrication of host composites using pitch or resin route followed by a number of densification cycles using HIP process and final pore sealing by CVD.

Structural aspects of Carbon-carbon composites

High strength, tough and highly conducting carbon/carbon composites can be processed through proper choice of reinforcing carbon fibers, carbon matrix precursor, density, macrostructure (type, size and quantities of defects i.e., defects, pores, crack etc.) and matrix microstructure (orientation of graphitic planes) of the composites. Some of these features are shown in Fig. 5. The voids and macrocracks are predominant in pitch derived C/C composites but can be reduced through processing using HIP route and become lower than in those made by CVD route or phenolic resin derived carbon route. The latter exhibit low densities. These features also control thermal transport mechanism in carbon-carbon composites. In order to have desired fiber/matrix bonding and to reduce cracking at the fiber/matrix interface, pyrolytic carbon coatings are also given on to the surface of the fibers [16].

The matrix microstructure (degree of graphitization) is also an important aspect governing the properties of carbon-carbon composites. From strength point of view, a semicrystalline or randomly oriented carbon matrix is



Fig. 10. Carbon/Carbon Composites products

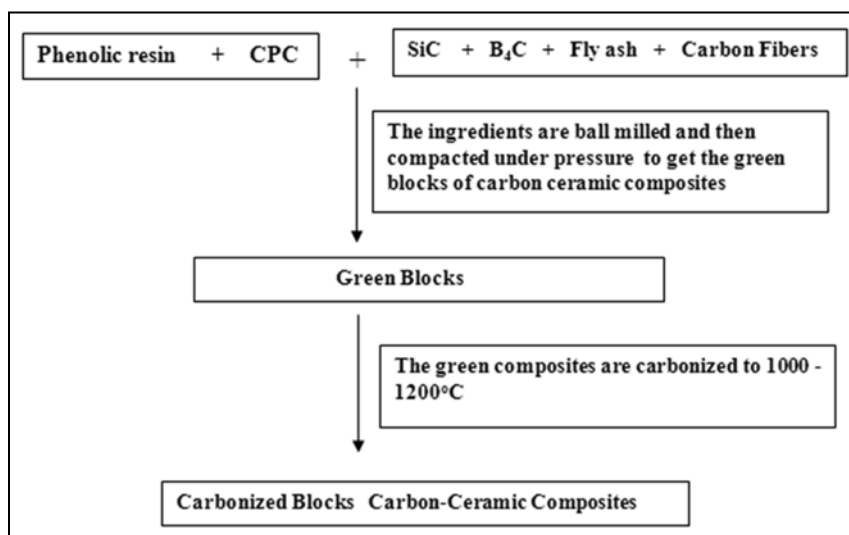


Fig. 11. Schematic representation of processing of Carbon-Ceramic composites

desired which can arrest crack propagation whereas for thermal and electrical properties, highly graphitic matrix is a prerequisite. These important aspects can be brought in by choosing appropriate fiber/matrix combinations and heat treatment temperatures. Fig. 6 Shows an example of this wherein very strong fiber/matrix bonding results in brittle fracture of the composites with low mechanical properties and adequate bonding achieved through carbon fiber surface chemistry or heat treatment temperature changes the fracture to non catastrophic failure with increased strength. Some of the most important and useful properties of carbon-carbon composites are light weight, high densities in the range 1.6-2.0 gm/cc, strength at high temperature (3000°C) in non oxidising atmosphere,

low coefficient of thermal expansion, high thermal conductivity (higher than that of copper and silver), high thermal shock resistance and low recession in high pressure ablation environments. Fig. 7 shows general trend of dependence of mechanical properties on type of fibers and carbon/carbon composites [3, 17-19].

All the properties of carbon/carbon composites are influenced by the type of the fibers used. Fig. 8 shows an example of dependence of thermal conductivity on type of carbon fibers.

Oxidation Protection of Carbon/carbon composites

Carbon is prone to reaction with oxygen at temperature of 450°C and above. For long time application of these composites at elevated temperature under normal environment, it is essential that these composites be protected against oxidation. Therefore a study on oxidation protection of carbon/carbon composites is as important as the development of the composites themselves [20]. Oxidation protection systems for carbon/carbon composites are based on (i) modification of matrix through addition of some oxidation inhibitors (like B, Si, Zr or their compounds) or/and (ii) deposition of ceramic coatings on the surface. These coatings are generally multilayer coatings of functionally gradient materials of carbides, nitrides and oxides of Si, Zr, Ta, Al etc.

Applications of Carbon/Carbon composites

C/Cs offers a large potential as high-performance engineering material. Therefore, in addition to the special defense, aircraft, and spacecraft applications, a steady interest is also growing in civil market segments. Based on the worldwide consumption, a general trend of carbon/carbon consumption is shown in Fig. 9. In terms of mass consumption and money, the main applications of C/Cs today are still in military, space, and aircraft industry, while those in the field of general mechanical engineering are picking up steadily.

With carbon-fiber reinforcement, the mechanical properties of carbon refractories can be further improved, thereby opening up new fields of industrial applications.

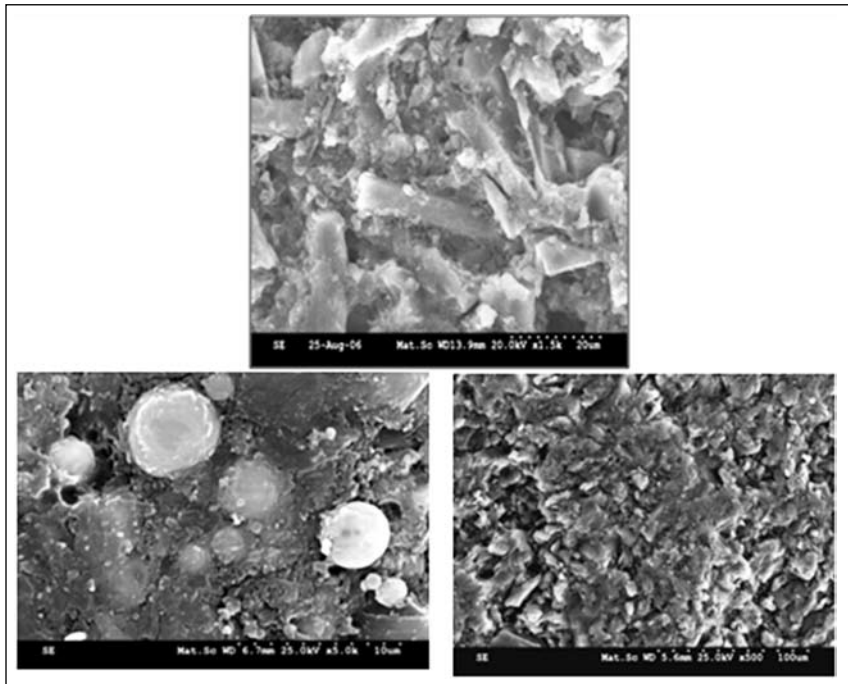


Fig. 12. Microstructure of carbon-Ceramic composites

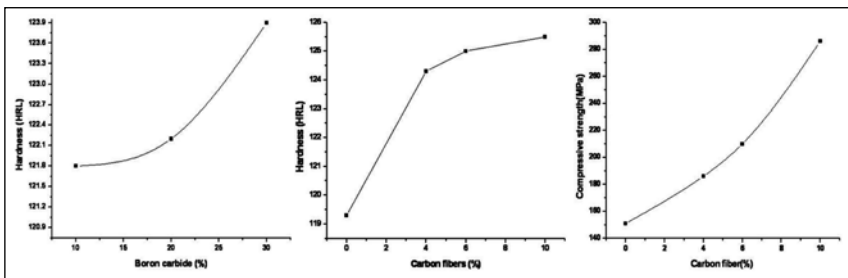


Fig. 13. Effect of addition of Carbon fiber and Boron carbide on mechanical behavior of carbon-ceramic composites heat treated at 1000oC

Carbon/carbon bolts, screws, nuts, and washers (Fig. 10) are used where high temperature and severe chemical condition are present [3]. Carbon and graphite are not wetted by molten glass. Therefore, carbon/carbon based materials are used as nonwetting crucibles for molten metals and in various parts of glass-container-forming machines. They are used in channeling systems to carry the gobbets of molten glass, as molds for crystal glass products, and as an asbestos replacement for hot-end glass contact elements for moving hot glassware articles. The latest applications of C/C structural materials are in advanced thermal management systems. These materials have potential for mechanical engineering applications in hot-load-bearing structure and corrosive surroundings, as substrates for electronics applications.

Carbon-Ceramic Particulate Composites

Another way of enhancing thermal stability capabilities of carbons is through addition of ceramic particulates in

bulk carbon and processing carbon-ceramic composites wherein major components are in particulate form in the form of carbon-ceramic composites. Fig. 11 shows schematic presentation of processing route for carbon-ceramic composites. These composites are generally prepared using phenolic resin as matrix precursor and silicon micro particles, graphite powder, carbon black, fly ash, and coke as reinforcement. All the constituents were mixed in predefined proportion using ball milling prior to hot pressing of mixture at 150°C temperatures and 200 kg. pressures. The prepared green composites are then carbonized at 1000 - 1500°C temperature in N₂ atmosphere with slow heating and cooling in order to avoid any crack formation or chipping of composites. On carbonization, green composites show increase in density with all compositions. Microstructural analysis as shown in Fig. 12 exhibit good packing of constituents. Addition of small amount of fibrous materials (5-10%) further improves physical properties of the composites. Ball milling technique results in homogeneity of carbon fiber with glassy carbon and other reinforcements [21, 22]

Mechanical Performance of Carbon-ceramic composites

Hardness is a resistance to penetration, wear, a measure of flow stress and resistance to cutting and scratching. As the percentage of carbon fiber increases hardness of the composites is found to increase (Fig. 13). It is found that increase in the carbon fiber content help to strengthen the interface bonding between the reinforced fiber and the resin matrix resulting in increase of the hardness and compressive strength of these composites.

These composites also exhibit better coefficient of friction since the reinforcing carbon fiber can effectively reduce the adhesion force and plough. Composites with 10% carbon fiber with 1 N load exhibit lowest coefficient of friction. The addition of carbon fibers strengthened the combination of interface between the carbon matrix and increased the strength of the composites. The composites filled with lower amount of carbon fibers, exhibits higher friction coefficient. Finally, with increasing applied load the friction coefficients increases. These composites find applications mainly as engineering and technical

carbons for Metallurgical, foundry and friction and wear applications and as seals etc.

References

1. H. Marsh, E.A. Heintz, F. Rodriguez-Reinoso., (Eds), Introduction to Carbon Technologies, Spain: University of Alicante, 1997.
2. T. Ishikawa, T. Nagaoki, (Eds) (Lewis IC, English editor), Recent Carbon Technologies, Japan, JEC Press, 1983.
3. E. Fitzer., L. M. Manocha. Carbon Reinforcements and Carbon /Carbon Composites, 1998, Springer, ISBN 3-540-62933-5.
4. M. Inagaki, New carbons: control of structures and functions., Elsevier; 2000.
5. D. Timothy Burchell "Carbon Materials for Advanced Technologies", 1999, Pergamon, ISBN 0-08-042683-2
6. E. Fitzer. Carbon, 1 25(1987) pp. 163-190.
7. K.S. Mazdidasni, (Ed). Fiber reinforced ceramic composites. Park Ridge, NY: Noyes; 1990.
8. F. Thevenot, Boron carbide-A comprehensive review, Journal of European Ceramic Society; 6 (1990) No.4, pp 205-225,
9. H.J. Hwang, S.L. Jung, K.H. Cho, Y.J. Kim, H. Jang, Tribological performance of brake friction materials containing carbon nanotubes, Wear; 268 (2010) pp519-525,
10. J.D. Buckley. Ceramic Bulletin,67(1988)364.
11. G. Savage. Carbon-carbon composites, New York: Chapman & Hall; 1993.
12. L.M. Manocha. Carbon fibers in encyclopaedia of materials: science and technology. In: Jurgen Buschow KJ, et al.,(Eds). Elsevier; 2001, p. 906-16.
13. C. R. Thomas. In: in Thomas CR, (Ed). Essentials of carbon-carbon composites. Royal Society of Chemistry; 1993. p. 1-36
14. J. D .Buckley, D.D. Edie. Carbon-carbon materials and composites, Noyes Pub; 1993.
15. W.V. Kotlensky In: Chemistry & Physics of Carbon, Walker PL jr (Ed),1973,Vol. 9, p 151.
16. E. McAllister, Lachman WL. Multidirectionally carbon/carbon composites, Kelly A, Milieko ST, (Eds). Handbook of composites, vol. 4. Elsevier; 1983
17. H.O. Pierson. Handbook of carbon, graphite, diamond and fullerenes Noyes Publication; 1993.
18. L.M. Manocha. Carbon 32(1994)213.
19. L.M. Manocha Mater Sci Eng A;412(2005)27-30.
20. D.W. Mckee, Oxidation protection of carbon materials In Thrower PA, (Ed) Chemistry and Physics of Carbon, 1991, New York: Marcel Dekker, Vol. 23: pp. 173
21. L.M. Manocha., Guddu Prasad, S.M. Manocha, Structural, Mechanical and Frictional studies of Carbon-Fly ash-Ceramic composites, Transaction of Indian ceramic society, 71 (2012), No. 2, pp. 99-107
22. L.M. Manocha, Guddu Prasad, S. M. Manocha, Effect of carbon fiber addition on phenolic based carbon-ceramic composites, Eurasian Chemico-technological journal, 13 (2011), No.1-2, pp. 49 - 57



Dr. Lalit Mohan Manocha, F.N.A.Sc, FGSA, is Professor and Head of the Department of Materials Science at Sardar Patel University, Gujarat. Prior to this, he was a senior Scientist at National Physical Laboratory, New Delhi. After his basic degrees in Physics from Kurukshetra University, he obtained his Ph.D. in Science in 1976 from Delhi University for his work on Development and Characterization of carbon Fibers, the work he did at National Physical Laboratory, New Delhi. His first Post Doctoral was at Institut Chemische Technik, University of Karlsruhe Germany during 1977-78 as Alexander von Humboldt Fellowship wherein he worked on Development of Carbon-Carbon composites. Later on he had JSPS Fellowship at Tokyo Institute of Technology during 1985-86, Foreign Professor at TIT during 1998, UNIDO Expert to S.Korea in 1991, NSF visits to Clemson University since 2003 and so on. He has undertaken many National (DST, DRDO, DAE, UGC etc.) as well as International projects (DST-NSF, IFCPAR, DST-BMBF, DST-RFBR etc) in the area of Advanced Carbon materials and composites. His current Research & Development interests are in the field of Carbon fibers and carbon-carbon composites for strategic and Industrial applications; Processing, Structure, properties relationship; Development of carbon nanomaterials, Porous carbons and carbon nanocomposites for structural, thermal and energy applications; carbon based ceramics and composites; high temperature ceramics and ceramic matrix composites. Dr. Manocha also served on a highly influential five-member Task Force under the chairmanship of the former Indian president, Dr. A.P.J. Abdul Kalam, to develop advanced composite. He has organized several National/International Technical meetings on carbon, ceramics and composites. He is on the advisory board of several National/International organization. He is Fellow of NASI and GSA. He is recipient of many awards including CSIR Technology Award, Homi J Bhabha Award (UGC) Vikram Sarabhai Award, MRSI Medal 1995, Superconductivity and Materials Size Prize 2011, and 2011 Bridge Building Award of Engineering Ceramic Group of American Ceramics Society.

Micro to Macroporous Carbon Materials

Satish M. Manocha

University School of Basic & Applied Sciences, Guro Gobind Singh Indraprastha University

Sector 16-C Dwarka, -110078

E-mail: sm_manocha@rediffmail.com

Abstract

Porous carbon materials having nano to micron range porosity are predominantly amorphous carbon materials with highly developed internal surface area, interconnected porous structure and high degree of surface reactivity. These unique characteristic properties make porous carbon materials a versatile adsorbent for separation of both gaseous and liquid phase molecules. The separation by the process of adsorption is very specific process and depends on pore size, pore shape and pore size distribution for separation of different sizes of molecules from liquids and gaseous phase. Advantages of porous carbon materials as adsorbents are simple design and operation those can be easily adopted. Natural precursors such as wood, seeds, biowastes result in activated carbons with high surface area of the order of 700-1000 m²/gm but with wide pore size distribution. As the size of molecules vary from nano meter to micrometer, need exists to develop porous carbon with appropriate pore size and pore size distribution. This has been achieved by selection of modified synthetic methods such as template method wherein pores size is dictated by the size of the template or by polymer blend method. These methods result in activated carbons with narrow pore size distribution in nanorange and high surface area up to 2000 m²/gm.

Introduction

Porous carbon are nongraphitic form of carbon, with varying porous structures, pores varying from micron size to nanosize and characterized by internal surface areas ranging from 100-3000 m² per gram [1]. The word pore is derived from the Greek word meaning passage, and distinguishes it from an isolated void and hence depending on shape and size of pores, these are broadly classified into two groups, foams with predominantly large pores and porous carbons with more of small size and interconnected pores [2-7]. Latter are also called activated carbon and have been in use for thousands of years. Their applications in water purification can be dated back to 2000BC. And currently varieties of carbons as such or with other additives are being used in water purification for removing organic, inorganic and biological impurities. The major development of activated carbon began during World War I, when activated carbon were used in gas masks. Now porous carbons are finding applications both for gas and liquid phase adsorptions. Porous carbons are versatile adsorbents because of large surface areas available both on the surface as well as inside the interconnected pores. Porosity in carbons has disadvantages in addition to advantages. In nuclear graphite, for example, porosity is undesirable as it allows for gasification within the carbon structure, resulting in corrosion and loss of mechanical strength, whereas, its presence in activated carbon accounts for usefulness as for adsorption application in porous solids. Porous carbon can be grouped in to two categories:

(i) activated carbon consisting of porous carbon with added active surface chemical groups, (ii) carbon foams with desired architecture of pores for structural and thermal applications. Recently these have been used as templates for making ceramics. The processing of activated carbon includes: raw materials selection, (ii) pyrolysis and (iii) activation. Various types of raw materials are used for preparation of porous carbon which includes both natural occurring and synthetic polymers. For the selection of an appropriate raw material for preparation of porous carbon, several factors are taken into consideration. Industrially, inexpensive material with high carbon content and low inorganic (i.e. low ash) contents is preferred as raw materials for the activated carbon. High density of precursor and sufficient volatiles contents are of considerable importance. Evolution of volatiles during pyrolysis results in porous char, essential for making activated carbon, while, high density contribute to enhanced structural strength of the carbon essential to withstand particle crumble. Varieties of raw materials have been used belonging to categories of (i) natural biowastes, (ii) coals and (iii) polymers.

Porous carbon from cellulosic materials:

The nature of precursor and method of activation, both have strong influence on the porous structure and adsorption capacity of resulting carbon. The feed stock of biological origin are still the major raw materials for commercial activated carbon. Wood is most abundantly available cellulosic materials obtained from all types of plants. In some cases, it is hard while in other cases it is of

Table I: Surface properties of pyrolysed and activated chars from different precursors

S. No	Sample	HTT, (°C) (heat treatment temperature)	Yield, %	Surface area, m ² /g	Activation temp, °C	Activation Time, min	Burn off, %	Surface area, m ² /g	Average Pore diameter, nm	Total pore volume, cc/gm
1.	Castor Oil Plant	650	29.58	323	700	60	32	590	1.9	0.289
2.	Castor Oil Plant	650	29.58		750	60	35	631	1.93	0.305
3.	Castor Oil Plant	650	29.58		750	120	62.5	863	2.1	0.445
4.	Bagasse	650	28.9	314	700	60	16	480	1.9	0.234
5.	Bagasse	650	28.9		750	60	20	511	1.88	0.24
6.	Bagasse	650	28.9		750	120	30	620	2.0	0.3
7.	Pine	650	26.32	--	800	45	85	1370	3.3	1.14
8.	Babool	650	34.20	201	700	240	33.68	687	1.6	0.31
9.	Babool	650	34.20		750	240	90	842	3.1	0.66
10.	Babool	650	34.20		800	45	70	987	2.02	0.51
11.	Babool	650	34.20		800	120	75	1226	2.2	0.70
12.	Babool	650	34.20		800	180	98.5	--	--	--
13.	Babool	650	34.20		800	240	ash	--	--	--

soft texture and highly porous. Whatever may be the type of wood, on pyrolysis, porous char is obtained. In general the char is not reactive and reactivity is incorporated by activation and thus char is converted into activated carbon. Castor oil plant wood, babool, sugarcane bagasses and pinewood were used for the research work carried out [8]. The pyrolysis of these samples was carried out in a programmed way followed by activation with steam at 700-800°C. The yield obtained was from 24-27% and that of carbon was 24-26%. The surface characteristics of pyrolysed and activated chars from different precursors are given in Table I.

Surface areas of all samples were measured by nitrogen adsorption at liquid nitrogen temperature. All the adsorption isotherms obtained were of type I showing

micro porous nature of solids. On activation, the surface area of all samples increased irrespective of nature of wood. By comparing the surface characteristics above in the table, one finds that temperature of activation has more pronounced effect on the development of surface area and pore size. With increase in the activation temperature, the surface areas are found to increase for all samples. Further, the activation time also plays an important role. With every increase in the activation time, the surface area was also found to increase with corresponding increase in the pore size. The surface morphological results showed that all these chars have different pore morphology. As seen from Fig. 1, the pore size distribution of these activated carbons are very wide and hence these carbons are of mixed porosity.

Porous carbon from Polymeric Materials (Template Method) :

Microporous carbon with narrow pore size distribution have been synthesized by using Template method [9]. Fig.2 shows schematic representation of the template method used for synthesis of porous carbons. The hydrolysed and calcined silica were used as template and phenol formaldehyde resin as carbon precursor. Phenol formaldehyde-silica micro composites were prepared by solution route. The microcomposites were

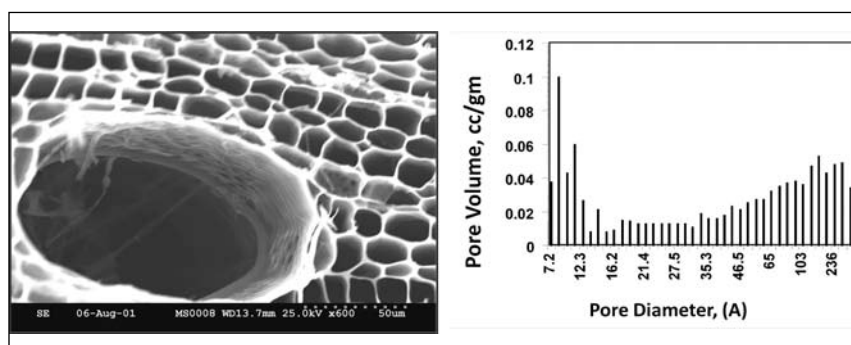


Fig. 1. SEM Micrograph and pore size distribution in a typical activated carbon prepared from Natural precursor (wood).

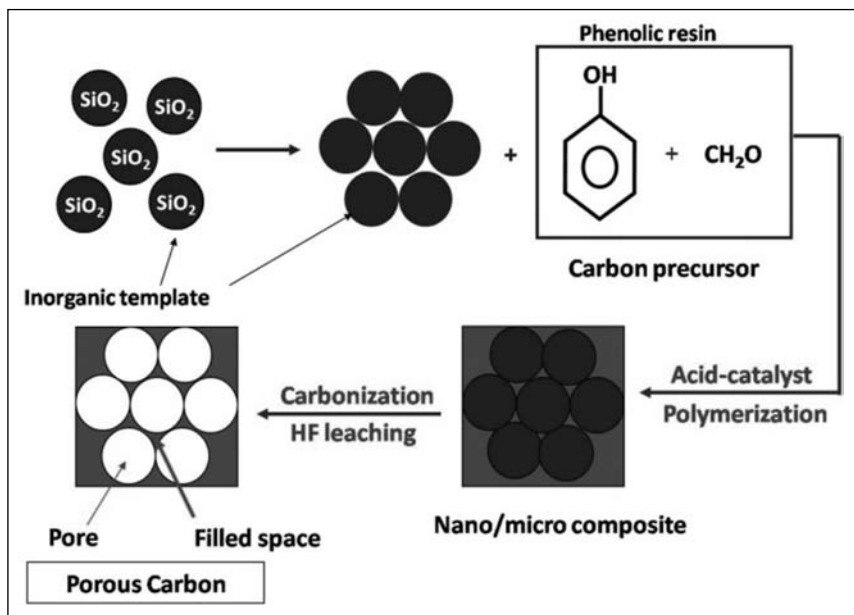


Fig. 2 Schematic of Development of Porous Carbons using Template method

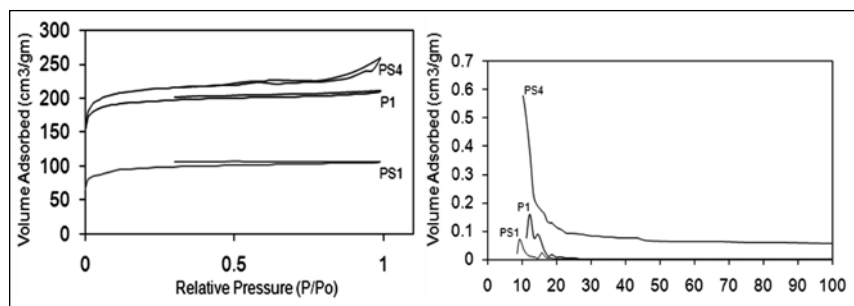


Fig. 3 : (a) BET Isotherms and (b) Pore size distribution in template derived porous carbons

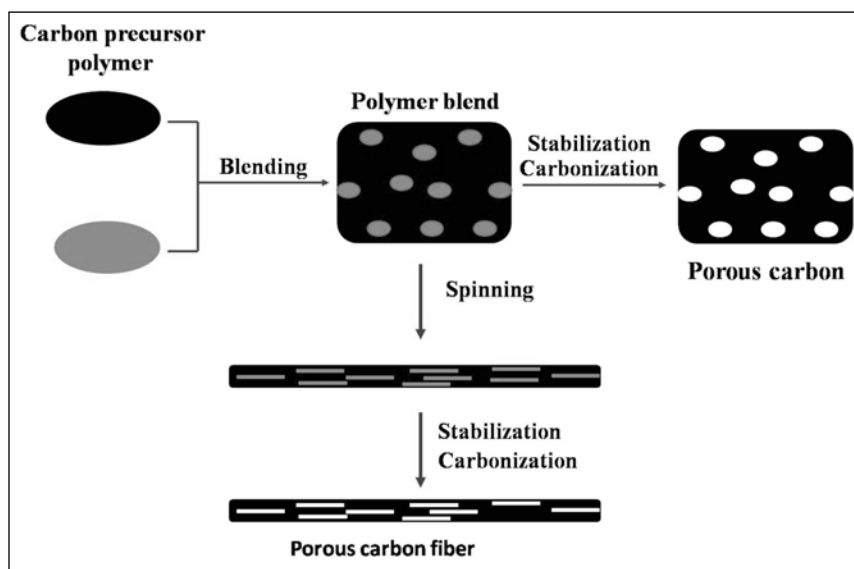


Fig. 4. Schematic of Processing of Porous carbons using Polymer Blend method

heat treated at 450^o in nitrogen atmosphere and subsequently, silica templates were removed by HF leaching. The carbon after dissolution of silica were steam activated at 850^oC. To see the effect of the template on the formation of porosity, blank samples were also prepared.

The porous carbon were characterized for their surface characteristics by nitrogen adsorption-desorption isotherm, SEM, FTIR, TGA analysis. The adsorption characteristics were measured and are given in Table II

Adsorption isotherms of porous carbon prepared with calcined silica as templates are of type I isotherm with 88% pores of size < 2nm while porous carbon prepared by using hydrolysed silica are microporous with 89% microporosity. These also show hysteresis loop at high relative pressure indicating the presence of some mesoporosity in samples. Fig.3 below shows the pore size distribution of the carbon.

It can be seen in the Fig 3(b) that very narrow pore size distribution could be obtained lying in the range of 1-2nm. Thus by selecting template of appropriate size and shape, carbon having desired porosity can be developed.

Porous carbon from Polymeric Materials (Polymer Blend Method) : The microporous activated carbon were also prepared by polymer blend method [11]. The technique involves two polymers components, a carbon precursor polymer component and a pore former polymer component. In this technique, the pore former polymer component is dispersed and stabilized into the matrix of carbon precursor polymer component. Upon subsequent heat treatment, the pore former polymer component is completely decomposed, leaving behind pores and carbon from the carbon precursor polymer component. This technique provides very good dispersion of the pore former polymer component into the matrix of the carbon precursor polymer component. The carbonized samples were then steam activated to enhance the porosity of the samples. The schematic diagram of the method used is given below in fig 4.

Table II: Pore characteristics of microporous carbon prepared with and without template

Template	Samples	S_{BET} , m ² /gm	V^b , cm ³ /gm	S_{Mi} , m ² /gm	V_{Mi} , cm ³ /gm	% S_{Mi}	Iodine number	Residue Silica, %
Without Template	P1	766	0.326	689	0.265	89.25	753	--
Template A (Calcined silica)	PS1	1062	0.474	953	0.372	89.81	1037	2.4
Template B (Hydrolysed Silica)	PS4	920	1.437	796	0.312	86.4	908	1.70

Table III: Surface Properties of Activated Carbons prepared by Polymer blend method

	S_{BET} (m ² /gm)	Micropore Area (m ² /gm)	Total Pore Volume (cm ³ /gm)	Micropore Volume (cm ³ /gm)	% Micropore Area	% Micropore Volume	Ave. Pore Dia. (A)
800°C/1hr.	813	763	0.3371	0.2924	93.85	86.74	16.57
800°C/2hrs.	1017	858	0.4573	0.4055	84.36	88.67	17.98
850°C/1hr.	848	764	0.3765	0.2984	90.09	79.26	17.74
850°C/2hrs.	949	866	0.4008	0.3378	91.25	84.28	16.89
950°C/1hr.	2114	1060	1.0447	0.4520	50.14	43.26	19.76

The activated carbon samples so prepared were characterized for their surface characteristics by nitrogen adsorption at liquid nitrogen temperature. The results are given in Table III:

The results show that activated carbon prepared under different activation time and temperatures have different characteristics. With increasing the activation temperature and time, surface area is found to increase and a maximum value of 2000m²/g could be achieved. Similarly as the activation time is increased, though an increase in surface area took place but due to severity in heat treatment mesoporosity become more and a decrease in microporosity took place. A close look at the pore size

distribution diagram (Fig. 5) show a very narrow pore size distribution of 1-1.5 nm could be achieved by controlling the processing parameters.

Carbon Foams: Another class of porous materials are the carbon foams. Carbon foams have attracted great attention recently because of their light weight and potential tailorability of their physical properties over a wide range [11–15]. Because of their structure, carbon foams display a rather unique combination of properties, such as low density, low thermal conductivity, high specific strength, high permeability, high porosity, high wear resistance, high resistance to chemical corrosion and high porosity of flow paths, making them indispensable for various engineering applications [16]. The porosity of foams lies in terms of hundreds of microns. The applications of carbon foams involve thermal managements, electrodes, catalyst supports and filters owing to their novel features such as adjustable thermal-conductivity and electrical conductivity, high porosity, low thermal expansion coefficient, high-temperature tolerance, etc. [17–19].

Most of carbon foams properties are very sensitive to physical properties such as density, number of cells per inch, cell wall thickness, shape of cell and connectivity of porous structure, etc. But the important thing is that whether the carbon from which they are made is graphitic or not, the transport properties may be very different. Especially, almost thermally insulating foams are expected with glass-like carbon and their applications are listed above,

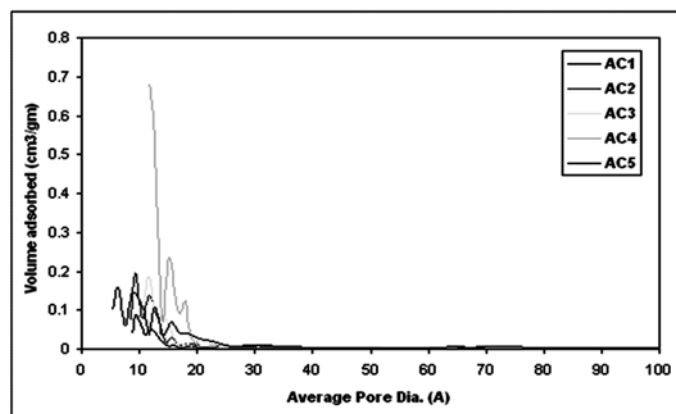


Fig: 5 Pore Size distribution of activated carbons prepared by Polymer blend method

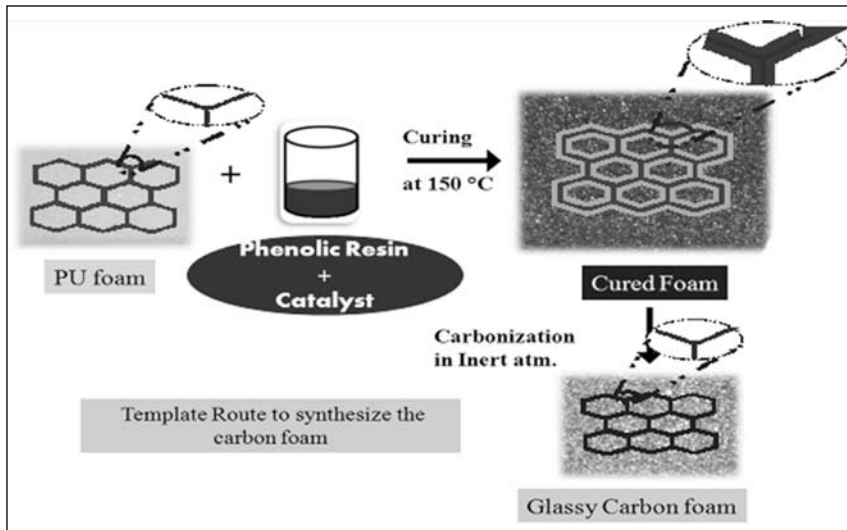


Fig. 6. Template route to synthesize carbon foam

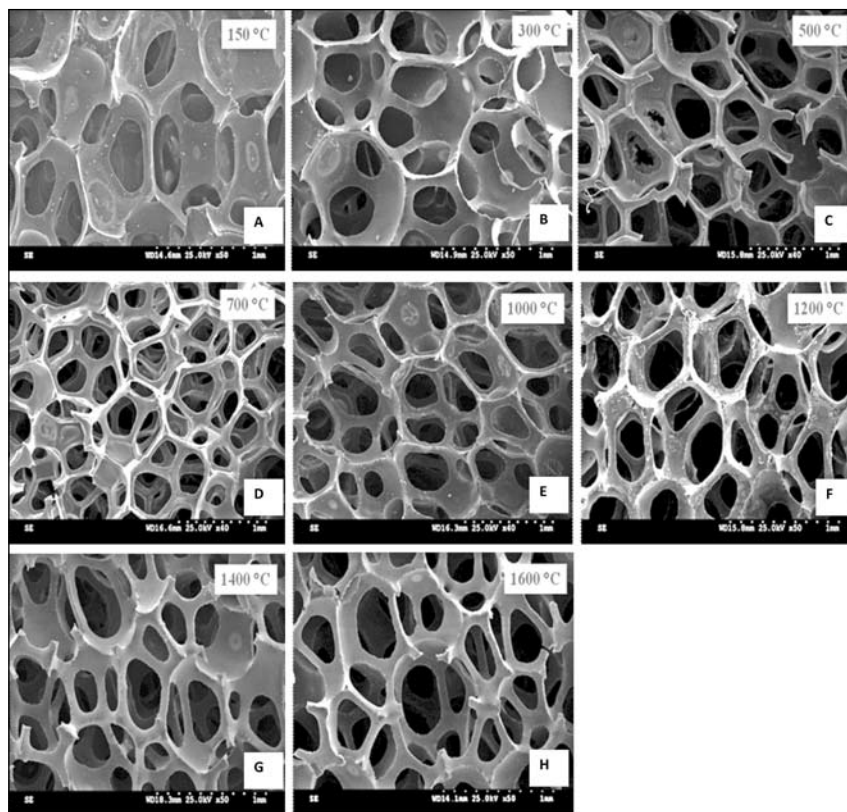


Fig 7: SEM images of Cured Foam heat treated at A) 150 °C , B)300 °C, C)500 °C, D) 700 °C, E) 1000 °C, F)1200 °C, G)1400 °C, and H)1600 °C

whereas graphitic foams are best suitable for applications as heat exchangers, heat sinks evaporative cooling and phase change devices, and may also be relevant to high temperature friction and nuclear application. The nearly isotropic properties and ability to conform to diverse net shapes make carbon foam a good candidate to be used as a core material in sandwich structures and as 3-D preforms that can be infiltrated with various matrices.

Several processing routes using replica, sacrificial template, or direct replica, nowadays available for the production of macroporous ceramics. The techniques differ greatly in terms of processing features and final microstructures/properties achieved. The polymer replica technique is an easy and well-established method to prepare open cellular structures with pore sizes ranging from 200 mm to 3 mm at porosity levels between 40% and 95%. The rheology of the impregnating resin and its adhesion on the polymeric sponge are the most crucial steps in this method.

Reticulated vitreous carbon foams were synthesized by impregnating commercially available polyurethane foams by phenolic resin. Figure 6 gives schematic view of processing of Carbon foams whereas the detailed method has been described elsewhere [6]. The cured foams were heat treated in an inert atmosphere at different temperature up to 1600°C to study the pyrolysis behavior of foam. Up to 1000oC the foams were heat treated in N2 atmosphere at slow heating rate 25°C/hr and that up to 1600oC were heat treated in Ar atmosphere at heating rate of 100°C/hr after 900oC.

The very crucial step is to coat phenolic resin on the PU foam uniformly. By controlling the density or viscosity of phenolic resin one can achieve the uniform coating. There are different solvents like methanol, acetone, ethanol, furfuryl alcohol, etc. to control the density of phenolic resin and we have used methanol as a solvent. The presence of extra resin in the sample may close some pores or having dead end at the bottom which results into the anisotropic properties in the final carbon foam structure.

The micrographs of carbon foams prepared by template methods show presence of interconnected pores. All the pores are of the same size and shape as the initial polyurethane foams.

Surface morphology of carbon foam

The 3-D interconnecting network of the carbon foam scaffold is revealed by the SEM image shown in Fig. 4.

Table IV: Properties of carbon foam

Characteristics	Our results	Duocel RVC Foam [26]	ULTRAMET, Advanced materials Solutions [27]	KFOAM, a product of KOPPERS [30]		
				Carbon Foam Grade L1	Carbon Foam Grade L1a	Carbon Foam Grade D1
Density, g/cc	0.11 (1000 °C)	0.049	0.045	0.38	0.34	0.48
Porosity, %	78 % (By kerosene porosity method)	-	-	70	78	72
Specific heat, cal /g.°C	0.3	0.29	0.3	-	-	-
Coefficient of thermal expansion, ppm/°C	1.41 (50 - 800 °C)	1.8 (100 - 1000°C)	1.65 (0 - 1000 °C)	3.0 (650 °C)	1.72 (650 °C)	0.69 (650 °C)
Average pore size, μm	100 to 600 (by SEM)	-	-	600	500	650
Compressive strength, MPa	0.58 (1000 °C)	(0.103-0.52)	0.62	3.4	1.7	2.5
BET surface area, m^2/g	30.2137(1000 °C) 23.7183(1600 °C)	-	-	-	-	-
Oxidation resistance	(550 °C) Air (more than 1600°C) Inert	(315°C) Air (1000°C) Inert	(350°C) Air (3500°C) Inert	-	-	-

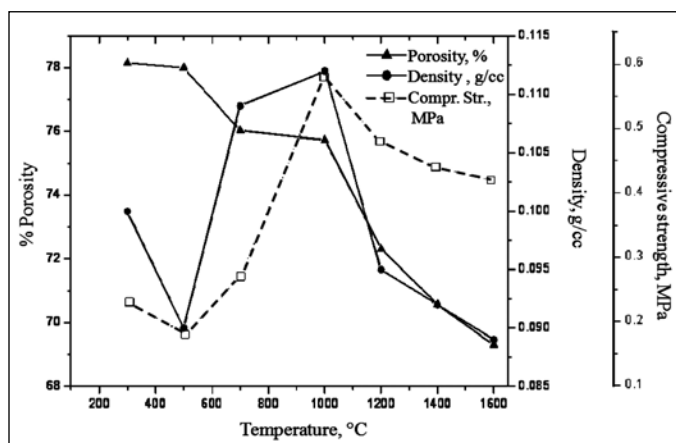


Fig.8. Density, porosity and compressive strength of carbon foam at different

SEM image shows that the pore diameter varies from approximately 100 μm to 600 μm . The pore wall thickness varies between 60 μm to 100 μm . As the temperature increases the volatiles present on the pore wall get removed resulting in shrinkage of the cells. Its 3-D interconnecting struts are ideal interfaces for the self assembly. After carbonization at different temperature, the SEM images of carbon foam also show its 3-D macrostructure exactly replicates the skeleton of the PU foam template. The interconnecting macropores are well retained except for some shrinkage. The size of the solid struts is reduced with increase in heat treatment temperature due to the uniform

framework shrinkage during the carbonization process. The uniform thickness of the mesostructured composite suggests that the coating process occurs homogeneously at the interfaces in different directions. The cells are made of pores and struts. Fig. 7, presenting the carbon foam at different temperature, indeed shows the open cell and well organized cell structure without any cracks and stress-induced failure in the carbon foam. The pores are uniformly distributed throughout the structure.

The SEM images also show that the pores are broken during sample preparation or machining. At higher temperature it is also possible that the small pore may start to collapse and create new bigger pores.

Fig. 8 shows the changes observed in density, porosity and compressive strength of carbon foam at different heat treatment temperatures. The density and compressive strength of carbon foam decrease up to 300°C and it increase up to 1000°C and then it again starts to decrease with raise in temperature. The porosity of carbon foam decreases as the heat treatment temperature increases because with increase in temperature the entire foam structure gets shrunk and some of the pores may get blocked with vitreous carbon.

The carbon foam shows a brittle failure mode undergoing successive cell wall fractures. The higher value of compressive strength obtained was 0.58 MPa for 1000°C heat treated carbon foam. The compressive strength

increases with the relative density. The increase of relative density implies an increase of the thickness of cell wall or decrease of the length of the cell edge. A thicker cell wall and shorter cell edge promote higher compressive strength. However, for the foam derived from different types of precursors, this relation is not followed very well. In addition, the strength of carbon foam is also related to the type of porosity and interconnected network of porous structure. It is also seen in Fig. 8 that the increase in temperature leads to more shrinkage resulting in decrease in the compressive strength after 1000 °C.

The carbon Foams prepared were characterised for their physical and mechanical properties. The comparison of the properties with commercial foams is shown in the Table IV. The density obtained was an intermediate while the thermal properties were well comparable with the available foams . Pore diameters could be controlled by controlling the initial properties of the precursor foams.

From these results, it could be concluded that porous carbon and carbon foams having highly interconnected porosity can be prepared by any of the procedure described above. Looking at the application of the resulting carbon, the selection of precursor and processing condition of pyrolysis and activation can be optimized to control the pore size, pore shape, total porosity and above all pore size distribution to develop carbon for a specific application.

References:

1. Manocha SM, Porous Carbon, Sadhana, 28 (1& 2): 2003, 335-48.
2. Burchell T. Carbon Materials for Advanced Technologies, 1999, Pergamon
3. Bansal RC. Active Carbon, 1988, Dekker, New York
4. Daley M.A. et.al ; Porosity in Carbon ‘Characterisation and application’ (Ed) J.W. Patric, London: Edward Arnold, pp 227.
5. Inagaki M. Sunahara M., Tanso, 183: 1998, 146.
6. Inagaki M. New carbon: control of structure & function, Elsevier, 2000, pp 126-146.
7. Patrick JW. Porosity in Carbon. Characterisation and Applications, 1995 ,Edward Arnold, London.
8. Manocha SM, Chauhan VB, Manocha LM. Studies on Development of Porosity in Carbon from Different Types of Bio-wastes, Carbon Science, 3(1): 2002, 1-5.
9. Manocha S, Movaliya N. Studies on Pore Characteristics of Microporous Carbon Prepared with Different Types of Silica Templates, Carbon Science,3(1): 2002, 17-24.
10. Manocha S, Brahmabhatt A. Development of microporous activated carbon using a polymer blend technique and its behavior towards methylene blue adsorption, Carbon Letters, 12(2): 2011, 85-89.
11. Gibson LJ. & Ashby M F. Cellular solids, structure and properties, 2nd Edn. Cambridge, UK: Cambridge University Press’1999.
12. Colombo P. Conventional and novel processing methods for cellular ceramics, Phil. Trans. R. Soc. A 364: 2006, 109-124.
13. Wang X, Zhong J, Wang Y, Yu M. A study of the properties of carbon foam reinforced by clay. Carbon 44(8): 2006, 1560-4.
14. Mehta R, Anderson DP, Hager JW. Graphitic open-celled carbon foams: processing and characterization. Carbon;41(11): 2003, 2174-6.
15. Chen C, Kennel EB, Stiller AH, Stanberry PG, Zondlo JW. Carbon foam derived from various precursors, Carbon;44(8): 2006, 1535-43.
16. Mattis DC. Theory of ferromagnetism in carbon foam, Phys Rev B: Condens Mater, 71(14): 2005, 144424/1-4/5.
17. Klett JW, Hardy R, Romine E, Walls C, Burchell T. High-thermal conductivity, mesophase-pitch-derived carbon foams: effect of precursor on structure and properties, Carbon;38(7): 2000, 953-73.
18. Yang J, Shen Z, Xue R, Hao Z. Study of mesophase-pitch-based graphite foam used as anodic materials in lithium ion rechargeable batteries, J Mater Sci;40(5): 2005, 1285-7.



Dr. (Mrs.) Satish Manocha obtained her Ph.D. Degree from I.I.T. Delhi and Master degree from Delhi University. Her 32 years experience include teaching, research and science management at Institutions like Sardar Patel University, I.I.T. Delhi, N.P.L. Delhi, C.S.I.R. Delhi, D.S.I.R. and D.S.T, Delhi. She has done significant research work pertaining to activated carbon, carbon based ceramics and composites, development of inorganic nanomaterials and nanocomposites, nanoclays, polymer nanocomposites, nanosilver reinforced HA composite for medical application, carbon and ceramic based materials from waste materials under sponsored research projects from DAE, DRDO, DST, CSIR, AICTE and UGC. Her work has been recognised by awards and honours such as Academician- 2013, Asian Pacific Academy of Materials (APAM) ; International Sardar Patel Award for Excellence in Technology Development-2012, MRSI-Medal 2012, Elected Fellow of Gujarat Science Academy -2003, Visiting Researcher, Tokyo Institute of Technology 1998-2003. She has published more than 80 papers in peer reviewed journals and a chapter in Sadhna-INSA, Delhi. To her credit is one patent on Smectite Nanoclays from Indian Clays. She has developed several processes which have been transferred to Industries, e.g. nanoclays, carbon and ceramic from Banana stem, porous carbon and carbon foams for high end application and inorganic-carbon hybrid nanomaterials. Consultancies have been given to companies in USA, Japan and India. 13 students have been awarded Ph.D. degree under her guidance and currently 6 more are working. She has delivered more than 25 Invited talks and key note addresses in International and national Conferences.

Chemical Vapor Deposited Diamond Thin Films: A Brief Overview on Synthesis and Characterization

J. Nuwad, Dheeraj Jain, C. G. S. Pillai and V. Sudarsan
 Chemistry Division, Bhabha Atomic Research Centre, Mumbai 400085, India.
 E-mail: vsudar@barc.gov.in

Abstract

This article provides a brief account of information towards synthesis and characterization of polycrystalline diamond (PCD) thin films using chemical vapor deposition (CVD) methods. Main emphasis has been given on two widely used deposition techniques namely, hot filament chemical vapor deposition (HFCVD) method and microwave plasma chemical vapor deposition (MPCVD) method. A comparative overview is presented for these two methods to gain a better understanding of their potential and inherent challenges. Detailed results on synthesis of high quality PCD films using MPCVD method have been presented. Scope of several characterization techniques such as scanning electron microscopy (SEM), X-ray diffraction (XRD), Raman spectroscopy and optical emission spectroscopy (OES) for characterizing these PCD films is also discussed. Finally, effect of few of the growth parameters on quality of as-deposited diamond films is highlighted.

Introduction:

Diamond; an important allotrope of elemental carbon is a unique material from both fundamental as well as applied interest. From researchers to common public, it has been a material of immense importance. Structurally, it is formed by three-dimensional extended network of covalently bonded sp^3 -hybridized carbon atoms in tetrahedral geometry crystallizing in face centered cubic lattice, which can be visualized as an interpenetrating combination of two individual FCC array of carbon atoms displaced along the [111] direction by a quarter of the body diagonal ($\sqrt{3}a/4$, a = lattice constant). Similar structure is found for next two group IV elements (Si, Ge) of the periodic table.

From scientific point of view, the unique applications of diamond stem from its distinct properties. These applications span over optical, mechanical, electronic and thermal domains. Being a wide band gap (5.45 eV) semiconductor, it has prospects in electronic devices, sensors, etc. The optical transparency of diamond over wide range of electromagnetic spectrum entails its possible use as transparent windows for special applications where common window materials stand inferior or unusable. The highest thermal conductivity of diamond ($\sim 15\text{-}20\text{ W/cm-K}$ at ambient temperatures, ~ 20 times better than copper, the best known metallic heat conductor) among all so far known bulk materials, in combination with its electrically insulating nature makes it one of the best candidates for heat dissipation in miniaturized and/or high performance electronic devices. Being the hardest known material with low friction coefficient, diamond finds its place in wide

range of mechanical application such as wear resistant coatings, tools for cutting/machining hard materials, etc. Apart from above applications, the excellent chemical inertness and radiation hardness of diamond brings in the potential use of diamond-based devices under extreme environments such as high temperatures, radiation fields, corrosive chemical environments, etc.

Given the potential of diamond in such a wide range of applications as mentioned above vis-à-vis its scarce natural availability in desired quality and quantity, it is but obvious to see extensive research in the direction of synthesizing diamond in laboratory. Our group has also been working for past few years in this direction, with special emphasis on preparing high quality diamond thin films for radiation sensing application. This article provides a brief mention of different synthetic methods of diamond preparation. A detailed account of synthesis and characterization of diamond thin films prepared through plasma assisted CVD route is also given in this manuscript.

Methods of diamond synthesis:

In nature, diamond is usually found (in single crystalline form) in coal mines and other deep geological deposits. These diamonds are formed under high-pressure & high-temperature conditions persisting in these deep mines/deposits over extended time periods. On the other hand, in laboratory conditions, diamond can be synthesized from various types of carbon sources (0-D to 3-D structures). Based on the choice of carbon source, these synthesis methods differ from high pressure synthesis route to chemical vapor deposition (CVD)

methods [1,2]. Figure-1 gives a schematic representation of different methods (along with the type of carbon source structure used there) for synthesizing diamond in bulk as well as thin film forms. It is important to mention here that the properties of laboratory synthesized diamond are almost similar to naturally occurring single crystal diamonds [3].

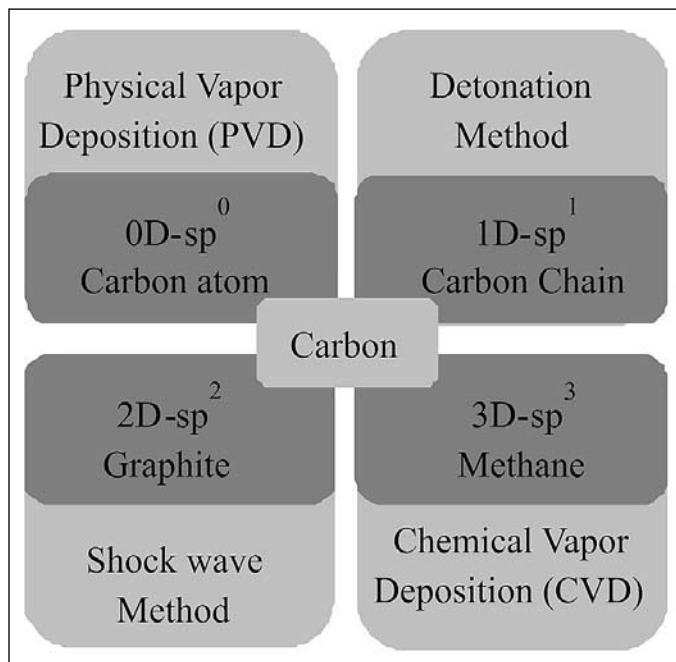


Fig.1: Methods of diamond synthesis using different carbon sources.

Synthetically, diamond in single crystal form can be prepared by mimicking its natural growth conditions (high temperatures up to 2000 K and high pressures ~6-15 GPa, where diamond is thermodynamically stable phase of carbon) inside the laboratory. This method is popularly known as high pressure high temperature (HPHT) method of diamond synthesis. However, the diamonds grown by this method invariably contain many crystal defects and impurities [4]. Use of CVD methods; on the other hand, is advantageous for reproducible growth in terms of impurity content and quality of diamond, as compared to other method. A major limitation of CVD method is that the grown films are polycrystalline in nature unless a single crystal diamond itself is used as the substrate. In practice, majority of CVD methods use heterogeneous substrates (c.a., Si, Mo, etc.) as getting single crystal diamond substrate in desired size is very difficult. In the following sections, we shall elaborating more on CVD methods.

CVD methods of diamond synthesis

Using the novel CVD approach, diamond can be artificially produced under entirely different conditions

than those required for its natural growth (HPHT). Historically dating; in 1953, W.G. Eversole successfully grown diamond for the first time at low pressures using CVD approach [5]. In principle, the CVD method involves decomposition of suitable carbonaceous precursors (c.a., methane, acetylene, etc.) in highly reducing atmosphere (H_2 in abundance) using different activation methods (c.a., thermal activation, electromagnetic or electric activation, etc.). Upon suitable activation, these precursors get decomposed into highly reactive smaller fragments, which eventually migrate and deposit over a suitable pre-heated substrate (Si, Mo, etc.). Under these conditions of high temperature and sub-atmospheric pressures where graphite is the thermodynamically stable phase of carbon, metastable growth of diamond occurs, mainly due to excessive presence of atomic hydrogen in the reaction medium. Abundance of atomic hydrogen ensures that the graphitic phase is minimized and defect-free polycrystalline diamond is continuously grown over the substrate. On suitable substrates (Si, Mo, etc.), the film growth starts at random locations (nucleation) and the crystals grow with different crystallographic orientations eventually leading to poly crystalline nature of the as-grown diamond film.

Types of CVD methods

CVD methods can be mainly classified on the basis of activation route adopted for dissociation of carbonaceous gaseous precursors. The popularly used CVD methods are plasma torch CVD [6], hot filament chemical vapor deposition (HFCVD) [7] and microwave plasma chemical vapor deposition (MPCVD) [8], etc. Depending upon the application of interest, different quality diamond films can be grown on a verity of substrates by using one of these methods. For example, HFCVD or MPCVD route can be easily employed for growing uniform thickness, small (~few mm²) to large (~few inches²) area planer films. On the other hand, plasma torch methods can be used for coating large and irregular surfaces with diamond films. One of the main parameters for growth of diamond films in CVD methods is relative concentration of the carbonaceous precursor (usually hydrocarbon gases) used with respect to hydrogen. Methane gas is one of the best candidates among different possible precursors [9] such as acetylene (gas), CO_2 (gas), CH_3COCH_3 (liquid), etc. [10]. Several studies have been reported to outline the possible growth mechanism of diamond prepared by CVD methods. Among them, the one popularly referred is given by Setka *et al.*, [11] for diamond growth using a mixture of methane and hydrogen and is schematically given in figure 2.

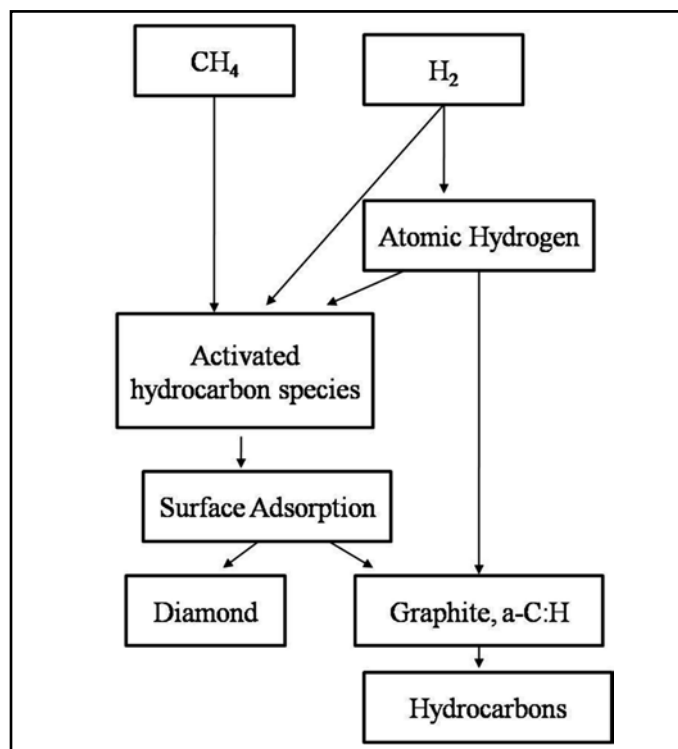


Fig.2 Schematic of the diamond film growth process in CVD [11]

In the following section, we shall describe the basic principle and operational methodology of two popularly used CVD methods namely HFCVD and MPCVD, as we have worked with them in our laboratory for growing PCD films. The carbonaceous precursor is methane in both the methods and atomic hydrogen is major reducing species.

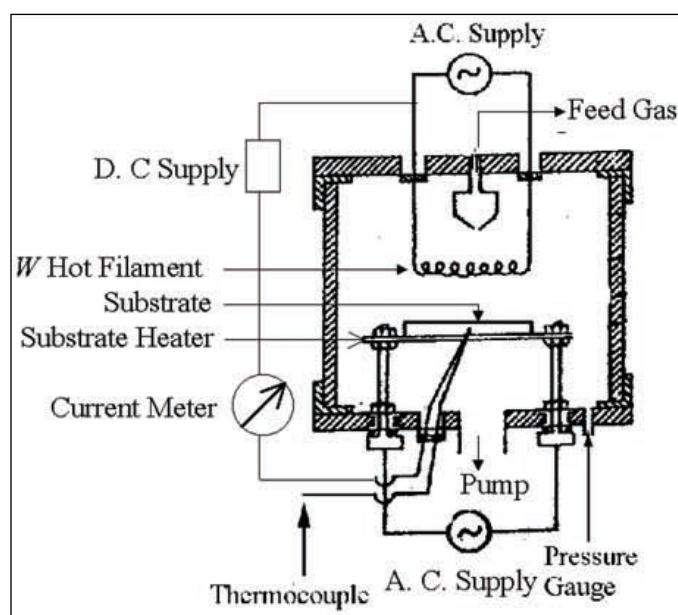


Fig.3 Schematic representation of a typical HFCVD reactor.

Hot filament chemical vapor deposition (HFCVD) method

Figure-3 shows the schematic of a typical HFCVD reactor. In this method, the feed gases (H_2 and CH_4) flow into the reaction chamber in desired proportion are thermally dissociated over a heated filament (2173 to 2773 K), which is kept above the pre-heated substrate (Si, Substrate temperature \sim 673 to 1373 K). The distance between the filament and substrate is usually kept around 2-8 mm. The filament is usually made-up of refractory metals (c.a., W, Re, Ta, etc.) [12]. Apart from dissociating the carbonaceous precursor into smaller fragments, these heated filaments also form metal carbides by reacting with carbon source during HFCVD operation. The carbide formation catalyzes the hydrogen dissociation and thereby improves the process. On the other hand, with constant usage, this leads to mechanical deterioration of filament due to swelling, bending, cracking and eventually making it brittle. This is one of the major disadvantages of HFCVD method.

Microwave plasma chemical vapor deposition (MPCVD) method

In this method, microwave radiation is used to create high energy plasma by utilizing the time varying electric field of the radiation having sufficient power to ionize the gas/gas mixture inside the reactor chamber. The range of the microwave radiation used in industrial processes such as microwave oven, etc. is used here. The plasma so generated can be defined as a combination of partially ionized gases, a mixture of electrons, atomic ions, molecular ions, neutral atoms, molecules, molecular fragments, etc. in their ground as well as excited states. The electron density in the plasma is highest at the centre and reduces as we proceed away from the centre. Further, in plasma, the electron impact dissociation is the main route for generation of reactive gaseous precursors/fragments, which are essential for diamond growth. Therefore, the dynamic situation is quite favourable for diamond deposition inside the microwave plasma containing reactive carbonaceous species and excess of atomic/molecular hydrogen in the vicinity of suitable substrates. The electrons absorb energy through the oscillating electric field of microwave radiation and reaches up to 5273 K while the gas (neutral species) temperature remains around 1073 K [13] in low pressure synthesis methods. Usually, the microwave radiation is impinged in a direction perpendicular to the substrate surface. The most commonly used microwave frequencies are 2.45GHz [14] and 915 MHz [15]. Based the microwave power and gas pressure inside the reactor, the plasma deposition can be classified into following two categories:

Table 1. Typical process parameters used in HFCVD and MPCVD methods for diamond synthesis.

Parameters	HFCVD	MPCVD
Substrate temperature	~673 K - 1373 K	~873 K - 1373 K
Typical Gas Mixture (CH ₄ :H ₂)	1:99	1:99 or 2:98
Total gas flow rate	400-1000 sccm	100-500 sccm
Temperature of Gas dissociation area	473 K - 2773 K	< 1773 K at low pressure > 6273 K at high pressure
Deposition area	~800 cm ²	~70 cm ² at low pressure ~1-5 cm ² at high pressure
Achievable Growth rates	0.1 - 9 μm/h	0.1 - 0.3 μm/h at low pressure 1 - 50 μm/h at high pressure
Advantages	<ul style="list-style-type: none"> • Simple setup. • Large area deposition is possible (1-10 torr). • Coating of irregular 3D object is possible. 	<ul style="list-style-type: none"> • Large area deposition at low pressure (1-40 torr). • Excellent film quality at high pressure (100-200 torr).
Disadvantage	<ul style="list-style-type: none"> • Contamination by filament material. • Poor filament stability. 	<ul style="list-style-type: none"> • Low deposition rates at low pressure/power. • Substrate temperature control is difficult at high pressure and high power.

Low pressure plasma: When the pressure inside the reactor is low, the electron mean free path becomes larger. As a result of this, collision frequency among the electrons and the gas molecules decreases and the thermal energy transfer is not very efficient. Therefore, notable temperature difference exists between neutral gaseous species (gas) and electrons in low pressure plasma and the gases are relatively cooler.

High pressure plasma: When the pressure inside the reactor is higher, the electron mean free path decreases. As a result of this, collision frequency among electrons and gas molecules, increases leading to the less imbalance in their temperatures in high pressure plasma. The absolute concentration of the atomic hydrogen and the atomic & molecular radicals therefore becomes quite higher in such systems. [16].

Use of MPCVD method over other known CVD methods (HFCVD, plasma torch, etc.) has the advantages of (i) High density of charged particles and reactive gaseous species compared to other methods (ii) deposition of large area films at lower pressure growth (iii) better homogeneity in the as-grown films, etc. The important process parameters typically used for diamond film synthesis using HFCVD and MPCVD methods are summarized in table 1.

MPCVD Setup: The main components

Figure-4 shows the overall view {Fig. 4(a)} and the various components {Fig. 4(b)} of MPCVD setup (M/s

Seki Technotron, Japan) used in our lab for synthesis of diamond films. The setup mainly consists of following parts as labeled in figure 4 (b):

1. Microwave power generator (magnetron head)
2. Wave guide
3. Stub tuner (to adjust the forward & reflected microwave power)
4. Deposition chamber (substrate stage, view ports, substrate height adjuster, etc.)
5. Substrate temperature measurement assembly (optical pyrometer)
6. Gas flow and circulation system (gas feed through, flow controllers, etc.)
7. Controlled temperature water circulator (chiller)
8. Vacuum system

Diamond film deposition by MPCVD method: experimental procedure

In typical experimental run on MPCVD system for diamond film deposition, a magnetron (6 kW maximum output power) is used to generate the microwave radiation. These microwaves are brought inside the deposition chamber through a rectangular waveguide. A dielectric quartz window isolates the wave guide from the deposition chamber kept at low pressures (~ 90 - 150 torr). High purity

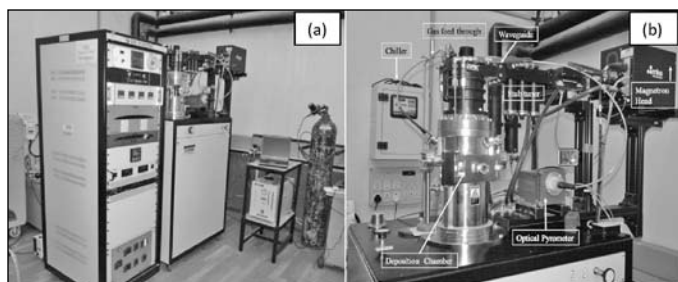


Fig. 4 (a) Microwave Plasma Chemical Vapor Deposition Setup (MPCVD) used for the diamond film synthesis (b) Various components of MPCVD system.

hydrogen (H_2), methane (CH_4), nitrogen (N_2) and oxygen (O_2) are used in required proportions (controlled by digital mass flow controllers) for growing micro or nanocrystalline diamond films. Gases are thoroughly mixed in the mixing chamber before introducing into the deposition chamber through a ring shaped sprinkler having small holes in the circular circumference. Appropriately treated (physically & chemically) single crystal Silicon substrate is placed over the Molybdenum substrate holder (2" diameter). The substrate holder is continuously cooled by water circulation. Prior to deposition, the system is evacuated up to $\sim 1.2 \times 10^{-2}$ Torr followed by flushing with hydrogen (~ 100 sccm, for ~ 30 min.) to insure the removal of trace amounts of residue atmospheric gases from the deposition chamber. After thorough flushing, the pressure inside the deposition chamber is allowed to stabilize followed by which the plasma is generated. Stub tuners are used to optimize the forward and reflected microwave power from the deposition chamber. The system is brought to desired diamond growth conditions (microwave power, chamber pressure and gas composition) slowly in incremental manner after the plasma is stabilized. The substrate temperature is measured in-situ using a two-color optical pyrometer during the deposition. After the completion of deposition for the desired time duration, the microwave power and pressure is slowly brought down, plasma is put off, system is cooled to ambient temperatures and sample is removed for further characterization.

In MPCVD method, the substrate can be heated mainly by two methods. (1) Heating by plasma itself without any additional heating arrangement for substrate. Here, the substrate holder is continuously cooled by the flowing water. The net substrate temperature therefore is result of net effect of these heating and cooling actions. This method has been used for all the results reported in this article. (2) Alternatively, the substrate can be heated by an external induction heater, called the heated stage MPCVD. In these systems, diamond can be grown at lower microwave power as well as lower pressures.

The substrate temperature is influenced by chamber pressure and the microwave power. However, the effect of the pressure is more prominent. At lower pressures, the plasma size is large and deflated, which is desirable for large-area film deposition. However, the substrate temperature is lower in this case. On the other hand; at higher pressures, the plasma confines to smaller volume thereby leading to increased substrate temperature. For optimal growth condition, we therefore need to choose the pressure so as to balance between large-area deposition and suitable substrate temperature. Alternatively, one can apply higher microwave power to increase the plasma size without altering the pressure much. But this can lead to undesired increase in substrate temperature resulting into inhomogeneity in the as-deposited films.

Diamond deposition by CVD methods: choice of substrates

The choice of substrate for diamond film deposition using CVD methods mainly depends upon the following criterion:

1. Minimum lattice parameter mismatch between substrate and diamond leading to lesser stress in the as-grown film.
2. Closely matching thermal expansion coefficient so as to avoid film delamination.
3. Suitable melting point, higher than the deposition temperature, etc.
4. Nature of application intended with deposited diamond films

Based on the above, it is imperative that the ideal substrate for diamond film deposition would be diamond itself. However, highly polished single crystalline/poly crystalline diamond substrates in the required size are not easily available. Therefore, several other substrates are routinely used. The most commonly used substrates are Mo and Si with $\sim 13\%$ and $\sim 20\%$ structural mismatch at ambient temperatures, respectively. Several other substrates (c.a., Ni, Cu, Quartz, etc.) have also been successfully used [17, 18, 19] for specific applications.

Diamond film deposition: Nucleation and growth mechanisms

Diamond Nucleation: In CVD process, the nucleation and growth steps eventually determine the film quality and morphology. Also, since the surface energy of diamond (~ 6 J/m²) is quite high [20], a lower nucleation density ($< 10^6$ cm⁻²) would lead to high energy barrier for nucleation formation. It is therefore very important to achieve

widespread uniform nucleation on a heterogeneous substrate surface. Diamond nucleation possibly starts with the adsorption of the sp^2 -bonded gaseous carbon species such as polycyclic aromatic hydrocarbons (PAHs) [21] or CH_3 radical [22]. PAHs are formed by hydrogen abstraction from carbonaceous precursors in the gas phase. Once these species are absorbed on the substrate surface they can either be etched by atomic H or form a diamond nuclei via conversion of sp^2 -site to sp^3 -site through hydrogen addition. This saturated carbon species will have lesser surface energy as compared to sp^2 -bonded species, thereby forming a stable nuclei. Also, CH_3 radical is a direct site for diamond nucleation. Once bonded to active site, it maintains the spatial tetrahedral configuration and further hydrogen abstraction leads to diamond network formation.

Methods of enhancing diamond nucleation: Silicon is the most frequently used substrate for deposition of diamond thin films using CVD method. This is obvious as it is omnipresent in entire semiconductor industry and is easily as well as economically available in large single crystal wafers. However, being polished to optical grades, the diamond nucleation on these pristine silicon surfaces is very slow and highly localized thanks to very high surface energy of diamond. In order to improve the nucleation density on such substrates, few substrate pretreatment methods are available and regularly being employed. Using these methods, desired nucleation densities (10^8 cm^{-2} to 10^{13} cm^{-2}) can be achieved on different substrates. In view of the fact that substrate pretreatment strongly influences nucleation density and average grain size of the as-deposited films [23], few of the commonly used methods are listed below.

1. Nucleation enhancement by mechanical polishing: In this method, the Si substrate is carefully polished with diamond paste (particle size ~ 100 nm to 10 μm) [24] impregnated in micro-polishing cloth. Nucleation density around 10^{8-10} sites/ cm^2 can be achieved.
2. Nucleation enhancement by ultrasonic treatment: This includes ultrasonication of substrate immersed in slurry of diamond powder dispersed in alcohol [25]. This method helps in achieving uniform nucleation density $\leq 10^{10}$ sites/ cm^2 .
3. Bias enhanced Nucleation (BEN): Here, the Si substrate is kept at negative DC bias to enhance the nucleation density up to $\sim 10^{7-11}$ sites/ cm^2 [26, 27].

Diamond films growth process: After nucleation; depending upon the growth parameters, small diamond crystals randomly grow on the nucleation sites. With continuous deposition, these crystals grow larger until they come in contact with each other and eventually coalesce to form a continuous polycrystalline diamond film as shown in figure-5 (a) & (b). With no scope left for lateral growth, these crystals starts growing vertically afterwards. During this process, morphology of those grains having fastest growth rate in vertical direction governs the final morphology of the diamond film. In short, we can say that the film morphology is a result of competition among different crystallographic planes. This vertical growth results into columns of diamond, increasing in size from the substrate surface towards the growth surface. This is known as 'columnar growth' and is shown in fig 5 (c).

Also, depending on the growth parameters, smaller crystallite can also grow in between the micro crystals; a process referred as 'secondary nucleation'. While continuing the growth process, these small grains fuse together to grow a well defined larger grain in between the micro crystals, which continuously grow in large size [28].

Growth of oriented diamond film

An important attribute of polycrystalline diamond films is the presence of grain boundaries. These grain boundaries influence several properties of diamond in comparison of single crystal diamond. For example, they act as a trap centers for charge carriers (electrons and

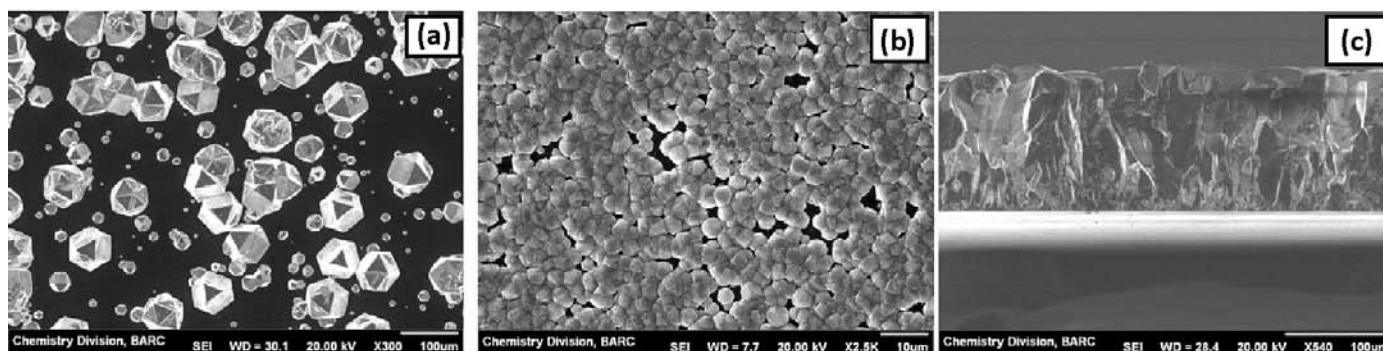


Fig. 5 (a) & (b) Represents the nucleation and growth of the diamond film (c) Columnar Growth of diamond film

holes), reduces their mobility and thereby affecting the electrical properties of the film. These grain boundaries can be minimized either by growing (i) single crystal films or (ii) oriented films. With extensive research efforts gone in this direction, it is now possible to grow well aligned diamond films with orientation of (100) and (111) faces parallel to the substrate surface. This can be achieved by (i) using substrates with a well defined orientation or (ii) by using carefully optimized growth parameters (pressure, temperature, gas flow rate, etc.).

Role of atomic hydrogen in nucleation and growth:

The atomic hydrogen that is produced by in-situ dissociation of H_2 molecule inside the deposition chamber (under plasma or heated filament conditions) plays an important role in diamond film growth process. It preferentially etches the non-diamond carbon phases thereby minimizing the incorporation of graphite content in as-grown films [29]. Several research efforts have been dedicated, both theoretically and experimentally to understand the effect of atomic hydrogen during CVD diamond synthesis under meta stable growth conditions [30, 31, 32, 33]. Few of the conclusions towards the possible role of atomic hydrogen during nucleation and growth of the films are listed below.

1. Generation of reactive gas-phase precursors like methyl radical (necessary for diamond growth)

from hydrocarbons through hydrogen abstraction reaction.

2. Hydrogenation of unsaturated carbon species on substrate surface.
3. Reduction of critical nuclei size and stabilizing diamond nuclei against graphite nuclei.
4. Destruction of gas-phase graphite precursors and preferential etching of sp^2 -bonded carbon species.
5. Hydrogen abstraction form surface hydrocarbons to create active surface sites for diamond growth.
6. Prevention of the growth surface reconstruction via hydrogen termination.

In hydrogen abstraction reaction, hydrogen atom reacts with another hydrogen atom bonded either to a carbon or to the growth surface. This can be schematically written as follows:



Where, ' C_d^* ' is an activated surface site.

Characterization of CVD grown diamond films

Several experimental techniques are routinely being used for the characterization of CVD grown diamond films.

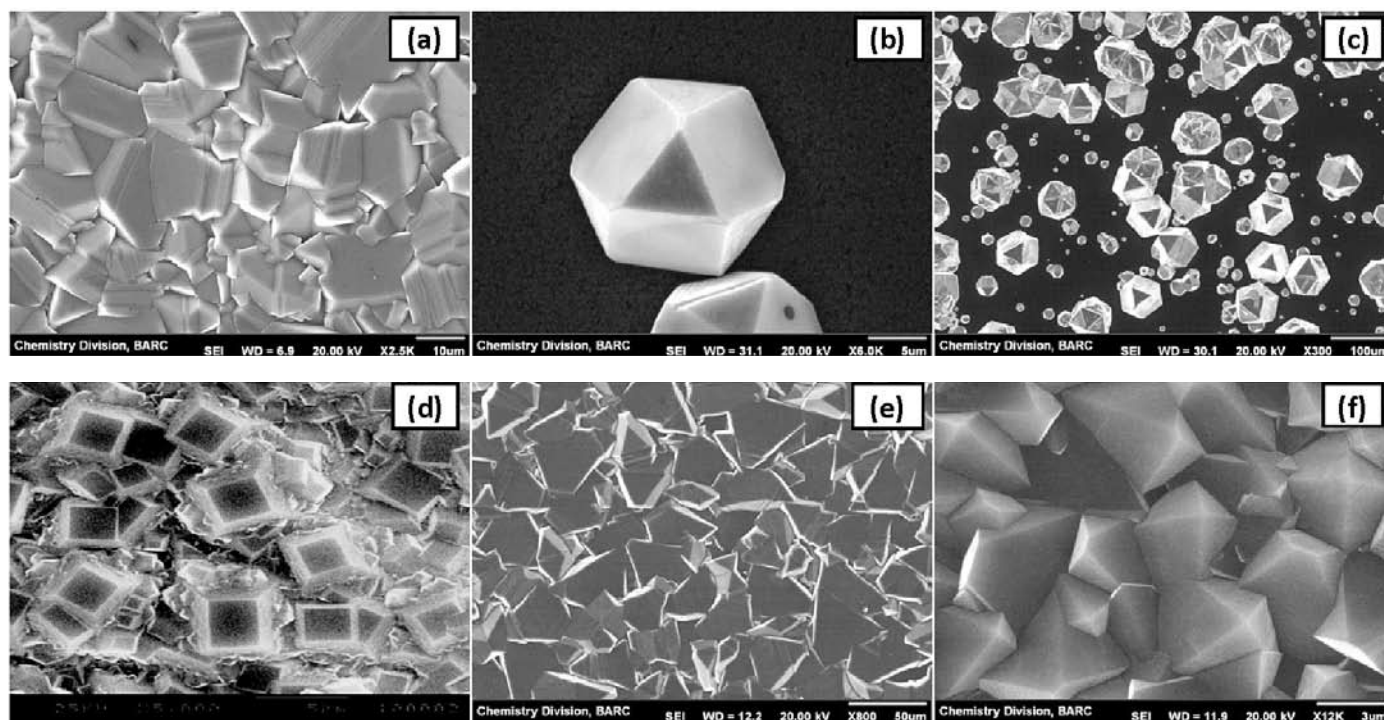


Fig. 6: SEM images of various CVD diamond films grown in author's lab (a) a typical randomly oriented poly crystalline diamond film, (b) a diamond crystal during nucleation stage, (c) several diamond nuclei during initial growth stage, (d) (100) oriented diamond film, (e) (111) oriented diamond film and (f) (110) oriented diamond film.

Important among them are the techniques like Scanning electron microscopy (SEM), X-ray diffraction (XRD) and Raman Spectroscopy. A brief account of the potential of these techniques along with representative results is presented in the following section:

Scope of scanning electron microscopy (SEM)

SEM is mainly useful towards characterizing the topography, surface morphology, uniformity and thickness of the as-grown film. CVD grown diamond films, being crystalline in nature usually shows well faceted crystallites. As most of the grown films are polycrystalline in nature, one can observe randomly oriented crystallites in the film as shown in figure-6 (a). Continuous or discontinuous pattern of films during their initial growth period can also be understood as represented in figure-6 (b) and (c). Depending upon the growth parameters, these films can be grown in preferred orientation and SEM comes as a very useful tool to characterize them as shown in figure-6 (d), (e) and (f) for (100), (111) and (110) oriented films, respectively. Cross sectional SEM is used for measuring the thickness of the grown film. For thickness measurement, films are cut in half and placed perpendicular in the SEM substrate stage. A look at the morphology of the fracture surface (or cross section) can throw light on the 'columnar growth' pattern of the films.

Scope of X-Ray diffraction (XRD)

Since most of the CVD grown diamond films over heterogeneous substrates are polycrystalline in nature having randomly oriented crystallites, X-ray diffraction becomes an obvious first hand tool towards the bulk characterization of these films. X-Ray diffraction measurements confirm the presence of various crystallographic planes by observing the corresponding reflections from them at expected diffraction angles (2θ). For bulk diamond, these reflections occurs at $2\theta = 43.9^\circ$, 75.4° , 91.6° and 119.9° corresponding to (111), (220), (311) and (400) planes, respectively [referred from JCPDS card no.: 02-1248]. Presence of these reflections confirms the presence of diamond phase as shown in the XRD pattern of an as-grown PCD film in our lab (figure-7). The other reflections as seen in figure-7 are from the silicon substrate. Further, presence of any non-diamond crystalline phase such as graphite, crystalline chemical impurity, etc. can also be identified by diffraction measurements. For example, graphite phase can be identified by peak positioned at $2\theta \sim 26.5^\circ$ corresponding to (002) reflection [referred from JCPDS no.: 08-0145]. Another important information that can be derived from diffraction studies is the preferred orientation of films, which is reflected in the anomalous

enhancement of the intensity of diffraction peaks from planes lying parallel to the substrate planes. Also, the peak broadening in XRD pattern indicates the presence of smaller crystallite size and/or lattice strain present in the as-grown film.

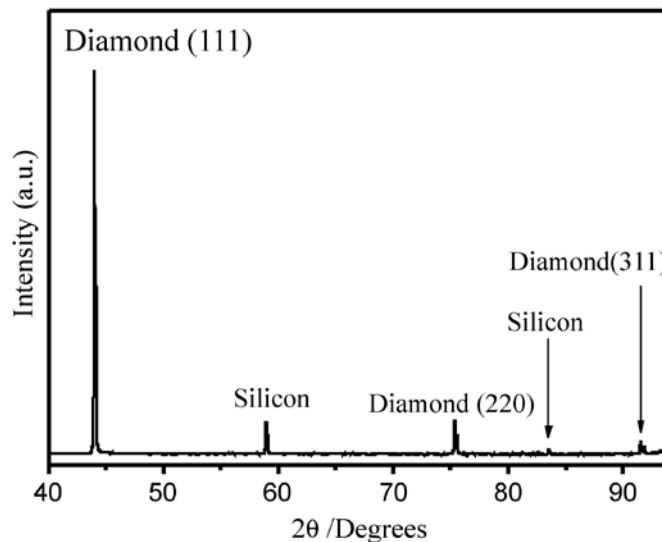


Fig. 7: Typical X-ray diffraction pattern of randomly oriented PCD film deposited over Silicon substrate.

Scope of Raman spectroscopy

Raman spectroscopy is one tool that plays a very crucial role in characterization of CVD grown diamond films and related materials. Using Raman spectroscopy, we can investigate the bonding structure in various carbon-based films. This technique can be used to distinguish bonding type, domain size in the carbon films and it is sensitive to internal stress in amorphous and nano crystalline films [34]. Crystalline diamond shows a single sharp Raman peak at 1332 cm^{-1} [35] as shown in figure 8 (a). On the other hand, a highly oriented polycrystalline graphite shows a single sharp peak located at 1580 cm^{-1} corresponding to E_{2g} -mode of the perfect graphite crystal known as 'G-band' [36]. Disorder in graphite network gives rise to another peak at 1350 cm^{-1} , called 'D-band', which is a zone edge A_{1g} -mode. The intensity of 'D-band' increases with (i) increasing fraction of unorganized carbon in the sample and (ii) with reduction in graphite crystallite size [36] as shown in figure 8 (b). 'D-band' is present in all the disordered graphitic carbons such as glassy carbon, etc. Apart from peak identification, the shape as well as width of diamond's characteristic Raman peak provides information about the quality of diamond film. Lesser the peak width; better is the quality of as-deposited diamond. The peak width should always be measured after proper Rayleigh correction. Apart from this, Raman spectroscopy also provides very useful information regarding the various

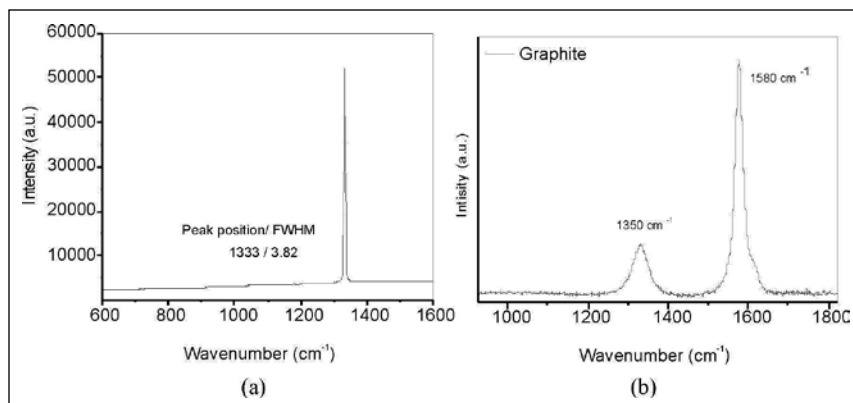


Figure 8: Raman spectra of (a) poly crystalline diamond film (b) polycrystalline Graphite

impurity/defect centers present in the films by means of corresponding fluorescence signature associated with such impurity/defect centers, which may appear along with the expected Raman signal of diamond.

Scope of Optical Emission Spectroscopy

In optical emission spectroscopy, one can measure the wavelengths of the photons emitted by different species such as atoms, ions, molecular fragments, etc. during their transition from excited state to ground state or lower energy state inside the plasma. Though not a fully comprehensive technique, yet it is quite useful to identify the various optically active species present in the plasma during the diamond deposition experiment. One example of usefulness of OES is identifications of species originating from nitrogen contamination of the feed gases while depositing highly pure, electronic-grade diamond films. A representative OES spectrum recorded during the deposition of such a film is presented in figure-9 ($\text{CH}_4/\text{H}_2/\text{N}_2$ plasma) where the nitrogen content in the methane gas were found unusually higher. OES spectra consists of Balmer lines from atomic hydrogen (H_α , H_β and H_γ at 656.2, 486 and 433 nm, respectively), peak related to CH (~433 nm) and C_2 swan-bands (~473.7 & 516.5 nm). Apart from them, a significant peak around 389 nm is seen, which corresponds to optical emission band of CN species, thereby indicating the presence of nitrogen in the otherwise intended $\text{CH}_4\text{-H}_2$ plasma. Such information has been quite useful in developing proper film growth methodologies during our research activities. Further, OES can also be used to estimate the relative concentration of various species (C_2 , CH, CN, etc.) by systematic studies with varying growth parameters.

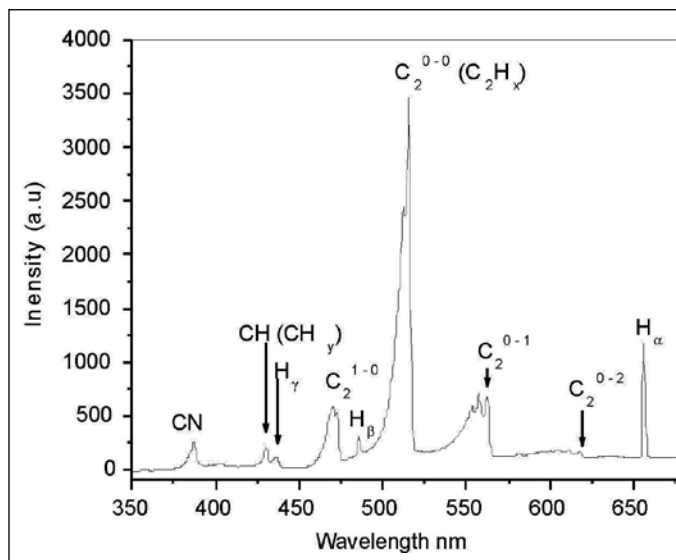


Figure-9: OES spectra of plasma recorded during diamond deposition experiment.

research activities. Further, OES can also be used to estimate the relative concentration of various species (C_2 , CH, CN, etc.) by systematic studies with varying growth parameters.

Effect of experimental parameters on diamond growth

Effect of experimental parameters on diamond growth

In order to develop diamond films with desired properties, a careful optimization of different experimental parameters is very essential. These include optimization of microwave power, feed gas ratio and flow rates, addition of oxidizing/reducing gases, deposition pressure, duration of deposition, large-area/small-area growth, substrate type and its pre-treatment, etc. Each of the above parameter needs to be carefully optimized depending upon the quality of films required for a particular application. As a representative of this, we present the effect of variation of methane concentration in the feed gas on the as-grown

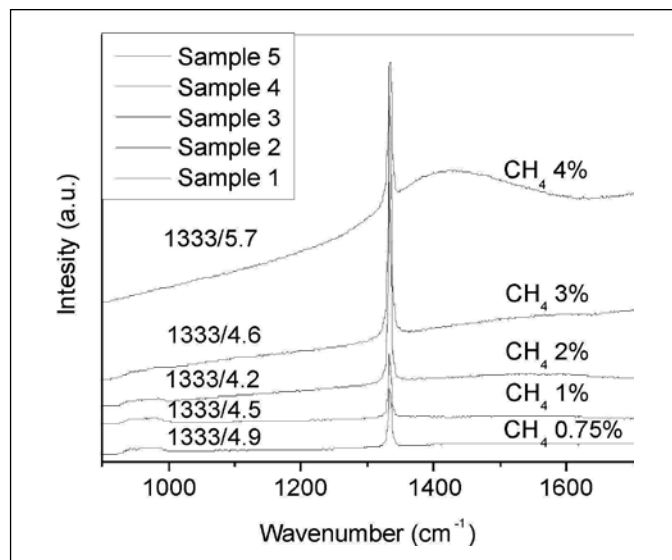


Figure-10: Raman spectra of the diamond films grown with varying methane concentration

diamond properties. Raman spectroscopy is taken as the characterization tool for the same. Figure-10 shows the Raman spectra recorded on films grown with varying methane concentrations while the other deposition parameters (H_2 /pressure/power/duration = Remaining of methane/115torr/4kW/6Hrs) were kept invariant. It can be seen from figure-10 that all the films show the characteristic Raman line of bulk diamond positioned at 1332cm^{-1} . However, it can also be noted that as CH_4 content increases in the feed gas, (i) Peak intensity of 1332cm^{-1} line increases (ii) Broad band $\sim 1400\text{-}1600\text{ cm}^{-1}$ related to sp^2 -carbon phase appears (iii) Luminescence background also increases and (iv) FWHM of line at 1332 cm^{-1} initially decreases and later increases.

These observations can be interpreted in the following manner: The Intensity of 1332 cm^{-1} peak increases with increasing CH_4 concentration and this could be due to increase in the availability of the diamond growth precursors. Rapid growth takes place with increase in carbon concentration as growth precursors are available in abundance for adsorption at activated sites. Further, when availability of growth precursor increases, the etching efficiency of atomic hydrogen reduces, which lead to co-deposition of sp^2 -phase. This results in increase in defect concentrations, which is responsible for increased luminescence background and appearance of sp^2 -carbon related phase. A further, initial decrease in Raman peak width (FWHM) indicates improvement in diamond film quality. Upon still higher methane concentrations, the defect growth takes place leading to increased phonon scattering from these defect sites as well as grain boundaries thereby showing an increasing trend in peak width corresponding to poor film quality at much higher methane concentrations. In conclusion, a balance between etching of non diamond phase and growth of diamond phase is required as improper etching will lead to the incorporation of defects.

Conclusion:

Preparation, characterization and properties of CVD grown diamond films are discussed in this manuscript. Among the different CVD techniques, emphasis is mainly given to describe the hot filament and microwave plasma based CVD methods (HFCVD and MPCVD). Different experimental parameters involved in both HFCVD and MPCVD techniques and their effect on nature of diamond films have been discussed in detail. The information provided by characterization techniques such as XRD, SEM and Raman spectroscopy are also briefly discussed.





Acknowledgements:

Authors are thankful for Dr. V. K. Jain, Head, Chemistry Division, BARC for his constant encouragement and keen interest in the presented work.

References:

1. P.W. Chen, Y.S Ding, Q Chen, F.L Huang, S.R Yun, *Diam. Relat. Mater.* 9 (2000) 1722.
2. H. Sumiya *Comprehensive Hard Materials* 3 (2014) 195.
3. H. Liu, D. S. Dandy, *Diam. Relat. Mater.* 4 (1995) 1173.
4. A. Yelisseyev, Y. Babich, V. Nadolinny, D. Fisher, B. Feigelson, *Diam. Relat. Mater.* 11 (2002) 22.
5. W. G. Eversole, U.S. Patents 3030187 and 3030188 (1962).
6. L. Abello, G. Lucazeau, B. Andre, Th. Priem, *Diam. Relat. Mater.* 1 (1992) 512.
7. A. K. Sikder, A. P. Jacob, T. Sharda *Thin Solid Films* 332 (1998) 98.
8. J. Wagner, C. Wild, W. M. Seibert, P. Koidl, *Appl. Phys. Lett.*, 61 (1992) 1284.
9. S. Jin, T. D. Moustakas, *Appl. Phys. Lett.* 63, (1993) 2354.
10. T. H. Chein, Y. Tzeng, *Diam. Relat. Mater.* 8 (1999) 1393.
11. N. Setka, *Hyomen Surface* 22 (1984) 110 .
12. T. Anthony, *Materials Research Society, Fall Meeting, Boston, 30th November to 5th December 1985.*
13. W. L. Hsu, *J. Appl. Phys.* 72 (1992) 3102.
14. M. Kamo, Y. Sato, S. Matsumoto, N. Setaka, *J. Cryst. Growth* 62 (1983) 642.
15. A. K. Mallik, K. S. Pal, N. Dandapat, B. K. Guha, S. Datta, D. Basu, *Diam. Relat. Mater.* 30 (2012) 53.
16. F. Silva, K. Hassouni, X. Bonnin, A. Gicquel, *J. Phys. Condens. Matter* 21 (2009) 364202.
17. S. Rey, F. Le Normand, *Thin Solid Films*, 519 (2011) 4426.
18. X. Liu, Q. Wei, H. Zhai, Z. Yu, *Transactions of Nonferrous Metals Society of China*, 23 (2013) 667.
19. M. Noda, A. Marui, T. Suzuki, M. Umeno, *Diam. Relat. Mater.* 14 (2005) 1757.
20. J. E. Field, *The Properties of Diamond*, Academic Press, London, 1979.
21. M. Sunkara, J. C. Angus, C. C. Hayman, F. A. Buck, *Carbon* 28 (1990) 745.
22. S. J. Harris, *Appl. Phys. Lett.* 56 (1990) 2298.
23. J. G. Buijnsters, L. Vázquez, J. J. ter Meulen, *Diam. Relat. Mater.* 18 (2009) 1239.
24. K. Mitsuda, Y. Kojimna, T. Yoshida, K. Akashi, *J. Mater. Sci.* 22 (1987) 1557.
25. M. P. Everson, M. A. Tamor, *J. Mater. Res.* 7 (1992) 1438.
26. Y. H. Lee, P. D. Richard, K. J. Bachmann, J. T. Glass, *Appl. Phys. Lett.* 56 (1990) 620.
27. B. R. Stoner, G. H. M. Ma, S.D. Wolter, J. T. Glass, *Phys. Rev. B* 45 (1992) 11067.
28. K. Kobashi, K. Nishimura, Y. Kawate, T. Horiuchi, *Phys. Rev. B* 38 (1988) 4067.

29. J. C. Angus, H. A. Will, W. S. Stanko, J. Appl. Phys. 39 (1968) 2915.
30. M. Frenklach, J. Appl. Phys. 65, (1989) 5142.
31. W. L. Hsu, J. Vac. Sci., 6 (1988) 1803.
32. W. Banholzer, Surf. Coat. Tech. 53 (1992) 1.
33. B. V. Spitsyn, L L. Bouilov, B. V. Derjaguin, J. Cryst. Growth 52 (1981) 219.
34. P. R. Chalker, Characterization of diamond and diamond like films, in: R. E. Clausing (Ed.), diamond and Diamond-like films and coating, Plenum Press, New York, 1991, pp 127-150.
35. R. E. Shroder, R. J. Nemanich, J. T. Glass, Phys. Rev. B, 41 (1990) 3738
36. F. Tuinstra, J. L. Koenig, J. Chem. Phys. 53 (1970) 1126.

	<p>Shri Jitendra Nuwad joined BARC in 2002 after completing his graduation from MDS University, Ajmer, Rajasthan. Since joining the department, he has been working on synthesis and characterization of novel carbon-based materials such as CVD diamond thin films, nanocrystalline diamond, diamond like carbon (DLC), CN_x thin films and other materials such as nanocrystalline semiconductors (II-VI system), nanodendrites, etc. These works have been published in international peer reviewed journals. He has extensively worked on both, hot filament (HFCVD) and microwave plasma (MPCVD) chemical vapor deposition (CVD) technique and developed a methodology for growing high quality polycrystalline diamond thin films using these techniques. He is also involved in development of diamond-based radiation detectors for applications under harsh chemical environments. His areas of interest include CVD methods for diamond synthesis, electron microscopy, vacuum science, thermophysical characterization of solids, etc. Currently he is pursuing M.Sc. in chemistry by research from Mumbai University, Mumbai.</p>
	<p>Shri Dheeraj Jain joined BARC in 2004 after graduating from 47th batch of BARC Training School in Chemistry discipline. Since then he has been pursuing his research activities in the field of thermophysical characterization of thorium-based nuclear fuels and related materials, investigation of sintering kinetics of nanomaterials, solid-state chemistry, etc. His current research activities include assessment of thermophysical properties of uranium and thorium-based metallic fuels, development of CVD diamond thin film-based radiation detectors to be used under harsh chemical environments, solid-state chemistry and electrical characterization of oxides using ac-impedance spectroscopy. He has been associated with teaching activities in BARC Training School since joining the department. He has been the recipient of TA-ITAS Young scientist award (2012) in recognition of his work in the area of thermal analysis.</p>
	<p>Dr. C.G.S. Pillai joined BARC in 1975 after graduating from 19th batch of BARC Training School. He obtained his Ph.D. (Physics) from University of Bombay in 1987. During his research career spanning over nearly four decades, he has significantly contributed in the area of thermophysical characterization of solids, especially nuclear materials. One of his notable achievements has been indigenous development of an apparatus for thermal conductivity measurement of solids from 300 to 1200 K, for the first time in BARC. He has also worked extensively towards development of CVD-based diamond thin films and their application for radiation sensing in highly corrosive environments. His other research interests included development of materials for solid-state hydrogen storage applications, solid-state chemistry, etc. Apart from his research activities, he has extensively contributed towards human resource development activities of the department throughout his career. He superannuated from BARC in 2012 as Head, Materials Chemistry Section, Chemistry Division, BARC. Presently, he is involved in teaching activities at Mumbai University and Centre of Excellence in Basic Sciences, Mumbai.</p>
	<p>Dr. V. Sudarsan joined Chemistry Division of BARC in the year 1994 after graduating from the 37th batch of the training school. He received his Ph. D degree in Chemistry from Mumbai University in the year 2002 for his work on the structural aspects of inorganic glasses. Subsequently he worked for a period of two years at the University Of Victoria, British Columbia, Canada in the area of structural aspects and luminescence of lanthanide ions doped in nanoparticles of inorganic hosts. Currently he is working on the optical properties of nanoparticles and glassy materials</p>

Raman Spectroscopic Studies of Carbon Related Materials

Dattatray J. Late^{1*} and Mukesh Pandey^{2*}

¹Physical & Materials Chemistry Division, CSIR-National Chemical Laboratory, Dr. Homi Bhabha Road, Pashan, Pune 411008, India

²High Pressure and Synchrotron Radiation Physics Division, Bhabha Atomic Research Center, Trombay, Mumbai 400 085, India

e-mail: dj.late@ncl.res.in, mpandey@barc.gov.in

Abstract:

Raman spectroscopy has been employed widely for the structural investigation of variety of carbon related materials, which includes, disordered and amorphous carbons, fullerenes, nanotubes, diamonds, carbon chains and poly-conjugated molecules etc., as it can identify unwanted by-products, structural damage, functional groups and chemical modifications (introduced during the preparation and processing). Carbon existing in the form of sp^3 , sp^2 and sp hybridization has attracted attention from scientific community due to the potentially exotic scientific and technological prospects in various fields. In its different structural forms, carbon has unusual electrical, magnetic, optical, mechanical properties. Thus, to achieve progress in carbon related materials, one has to adopt a method / procedure, which can characterize in a fast and precise manner. Raman spectroscopy offers a technique in this regard, and has been utilized to characterize carbon related material. In this review article we discuss Raman spectroscopy to probe the structural aspects of carbon materials in its different forms.

Keywords: Carbon related materials, Raman spectroscopy, and Structural investigation.

1. Introduction:

It is known that carbon can have three different types of bonding, namely, sp , sp^2 and sp^3 hybridization. Carbon atoms in sp^3 hybridization makes it a perfect diamond, while sp^2 makes perfect graphite. In nanotubes, the graphene sheets are rolled over to make a one dimensional structure. Raman spectroscopy is highly sensitive to the type of bonding and thus in principle it can be used for identifying unwanted by-products, structural damage, functional groups and chemical modifications (introduced during the synthesis and processing) in variety of carbon related materials, including disordered and amorphous carbons, fullerenes, nanotubes, diamonds, carbon chains and poly-conjugated molecules etc. Carbonaceous materials (i.e. diamond in the form of 3-dimensional, graphene sheets in 2-dimensional, nanotubes in 1-dimensional) have a good combination of properties such as high hardness, high optical transparency in visible and infra red regions, high electrical resistivity, chemical inertness, high thermal conductivity, low electron affinity and low coefficient of friction with metal surfaces. Because of these properties, these materials have wide range of applications such as wear resistant, optical, biomedical, low friction coefficient coatings, electroluminescence, field emission devices etc. [1-8].

The precise and non-destructive characterization during growth is therefore very important to understand

the role of different growth parameters and in controlling the impurities during synthesis. The growth parameters can be varied to produce materials of desired properties depending on the specific area of application. Raman spectroscopy is a very sensitive technique and is non-destructive in nature. Moreover, it does not require preparation of sample in specific form, which otherwise could have lead to complications in the analysis. In this paper we deal with Raman spectroscopy for probing CVD diamond films, where the presence of non-diamond component can be very precisely identified. Here one has non-diamond in the form of sp^2 hybridization as an impurity in the sp^3 bonded diamond matrix. Raman studies can probe both the compositions present. Graphene sheet have a perfect sp^2 character, and any defect introduces changes in its phonon spectrum, reflected accurately in its Raman spectrum. Nanotube, which is a perfect rolled structure of the graphene sheet, can be functionalized only when defects are introduced [9-17]. These structural defects are thus very important aspects, which are again probed very precisely using Raman spectroscopy. In addition, a- and c-axis coherence lengths (L_a , L_c respectively) and the d_{002} interplanar spacing affect the Raman spectrum of these materials, and hence provide its functional information and the various properties. Till date papers related to research on various forms of carbon nanomaterials such as zero-dimension (0D) carbon quantum dot (also known as graphene quantum dot and fullerene i.e.

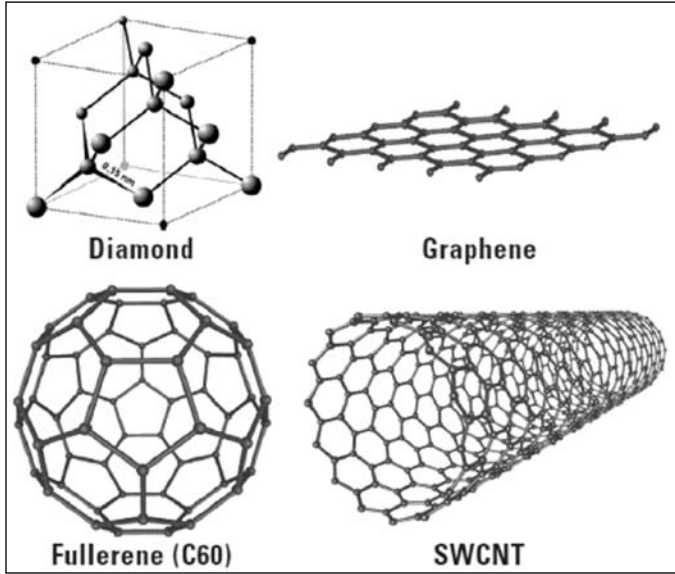


Figure 1. Structure of various carbon polymorphs. Graphene, a mother of all graphitic forms, is a 2D building block material for different carbonaceous materials, varying in all dimensionalities. It can be wrapped up to form 0D buckyballs, rolled into 1D nanotubes or it can stack into each other to form 3D graphite [21]. (Taken with permission from Thermo Scientific Application Note 51901, 2010).

(C_{60} , C_{70}), one-dimensional (1D) carbon nanotubes, two-dimensional (2D) sheet of carbon atom (graphene) and three-dimensional (3D) bulk graphite, diamond [18-21], as denoted in Figure 1 has been reported. In this review we make an attempt to summarize these results and report the characteristic Raman features of various forms of carbon. Also we describe the various modes of vibrations responsible for the Raman spectrum pertaining to these phases.

2. Basic principle of Raman spectroscopy:

Raman scattering refers to inelastic scattering of light, which in its quantized form consists of photons emanating from the fluctuating component of polarization. Photons entering a medium either lose energy to the medium or gain energy from the medium. In the former case it is called Stokes process, while in the latter case it is called anti-stokes process. Raman scattering is often expressed in the terms of excitations or de-excitations of the elementary quantized excitations of the medium, which include optical phonons in condensed matter and vibrations in molecules. In addition to Raman scattering, Brillouin scattering is also an inelastic process and propagates as acoustic waves or sound waves in its quantized form. This is observed in the frequency range which is less than 5 cm^{-1} . There is another form of scattering i.e. Rayleigh scattering, which is quasi elastic in nature. It may be noted that the most commonly encountered is the spontaneous Raman

process and its intensity is nearly $\sim 10^{-5}$ times that of Rayleigh scattering.

Raman scattering is a coherent two-photon process, in which the photon scatters only in presence of incident photon. This process is different from sequential absorption of a photon followed by its emission, as this is the case with fluorescence. It may be noted that in Raman scattering, the interaction of incident photon (with energy $\hbar\omega_L$) with the crystal, momentarily raise its energy from its ground electronic state (with energy E_{GS}) to a quasi-electronic state ($\hbar\omega_L + E_{GS}$). In general, ($\hbar\omega_L + E_{GS}$), does not correspond to a stationary state, therefore the system is said to be in a virtual level. Once the photon realizes that the system has no stationary state of energy $\hbar\omega_L + E_{GS}$, it leaves this unstable situation. In this process the photon can lose part of its energy in the interaction process, thus exiting the sample with a lower energy $\hbar\omega_L - \hbar\omega_{SC} = \hbar\Omega$. Since the sample has to return to a stationary state, the energy loss must correspond to a phonon energy. This corresponds to the Stokes process. If the incoming photon finds the sample in an excited vibrational state, and after the interaction the system returns to its ground level, the photon can leave the crystal with an increased energy $\hbar\omega_L - \hbar\omega_{SC} = \hbar\Omega$. This corresponds to the Anti-Stokes process. Since, Stokes processes are the most probable, vast majority of Raman spectra in literature are Stokes spectra, and the measurements are carried out by plotting the intensity of the scattered light as a function of the difference between incident and scattered photon energy, i.e. the "Raman shift". Even though the Raman shift units should be those of energy, it is historically plotted in cm^{-1} . These can be converted in meV using the relation $1 \text{ meV} = 8.0655447 \text{ cm}^{-1}$. The intensity ratio of Stokes to anti-stokes spectra depends very strongly on the sample temperature, hence this is a very popular method to monitor in-situ the temperature of the sample.

According to quantum mechanics, when the solid undergoes Raman scattering, the induced dipole moment describing its response to the incident electromagnetic radiation undergoes momentary changes during the vibrations. In matrix notation, the polarization is described as:

$$\begin{pmatrix} P_x \\ P_y \\ P_z \end{pmatrix} = \begin{pmatrix} \alpha_{xx} & \alpha_{xy} & \alpha_{xz} \\ \alpha_{yx} & \alpha_{yy} & \alpha_{yz} \\ \alpha_{zx} & \alpha_{zy} & \alpha_{zz} \end{pmatrix} \begin{pmatrix} E_x \\ E_y \\ E_z \end{pmatrix}$$

The first column on the right hand side is called the polarizability tensor. In normal Raman scattering process, this tensor is symmetric i.e. $\alpha_{xy} = \alpha_{yx}$, $\alpha_{xz} = \alpha_{zx}$, $\alpha_{yz} = \alpha_{zy}$. To first order of approximation, α can be expanded as $\alpha = \alpha_0 + \left(\frac{\partial \alpha}{\partial Q}\right)_{Q=0} Q$. The vibrations from state v'' having irreducible

representation $\Gamma_{v'}$ of the space group of the crystal under consideration to state v' with representation $\Gamma_{v'}$ are Raman allowed only when the direct product $\Gamma_{v'}^* \times \Gamma_{\alpha} \times \Gamma_{v'}$ contains the totally symmetric representation. Γ_{α} is the representation generated by the components of second rank polarization tensor α . It may be noted that since the ground state vibration is totally symmetric, only those vibrational species $\Gamma_{v'}$ for which $\Gamma_{\alpha} \times \Gamma_{v'}$ is totally symmetric will be Raman active. Thus, a vibrational transition is Raman allowed only if the normal coordinate describing its atomic displacements (Q_{α}) has same symmetry as any of its polarization components. Once the symmetry of the system is known, the symmetry of various modes of vibrations can be obtained from the character table of that particular group. Thus, the group theoretical selection rules prove very handy for complicated systems, and can decisively tell whether a particular vibration is going to be Raman active or not. Below we give the description of vibrational modes of different carbonaceous materials.

3. Vibrational analysis:

The different carbonaceous materials are broadly classified as modifications of either 2-dimensional graphene sheets (sp^2) or a 3-dimensional graphite (sp^2) and diamond (sp^3). Similarly, carbon nanotubes are rolled up graphene sheets, again with pentagons at the closed end of the tube. In the present section we describe the vibrational motion in these basic units, namely, graphene sheets, graphite and diamond.

Diamond crystallizes in cubic form and belongs to O_h^7 space group. It has eight atoms in the crystallographic network consisting of covalently bonded sp^3 hybridized network with one set of 4 atoms forming a face centered cubic cell, while another set of 4 atoms forming another face centered cubic displaced by $1/4^{\text{th}}$ the body diagonal. One can reduce this representation into a two atom representation (primitive lattice), whose basis vectors are [22]:

$$a_1 \perp a_2 \perp [a_3 - 1/2 (a_1 + a_2)]; |a_1| = |a_2| \text{ and}$$

$$\left| a_3 - 1/2 (a_1 + a_2) \right| = |a_1| / \sqrt{2} \quad [22].$$

The normal modes of cubic diamond at the Brillouin zone centre Γ : $T_{2g}(R) + T_{1u}(ac)$, ac is acoustic mode, R is Raman active mode, where the T_{1u} modes are classified as acoustic modes and T_{2g} modes are the only optically active Raman modes [23]. This mode of vibration as shown in figure 3(a), is a triply degenerate mode and can broadly

be viewed as the motion of two sub-lattices of diamond (consisting of the two interpenetrating FCC lattices) vibrating out of phase with respect to each other while maintaining the inversion symmetry.

Graphene belongs to D_{6h}^1 space group and has two atoms per unit cell, thus six normal modes at the Brillouin zone centre Γ : $A_{2u}(ac) + B_{2g}(i.a) + E_{1u}(ac) + E_{2g}(R)$ [24]; IR is infrared active mode, i.a. is optically inactive mode, R is Raman active mode and ac is acoustic mode. E_{2g} mode is a Raman active degenerate in-plane optical mode, and B_{2g} mode is out-of-plane optical mode, which is infrared as well as Raman inactive. Since graphene has two equivalent atoms in the unit cell, it does not have any infrared active mode. The different modes of vibrations in graphene are shown in Figure 3 (b). Graphite, forming a three dimensional lattice has four atoms per unit cell, but since only half the carbons have fourth neighbors that either lie directly above or below in adjacent layers, it has only two atoms of the unit cell in each layer those are now inequivalent, with the space group changed to D_{6h}^4 . This doubles the number of optical modes, and the optical modes become Davydov-doublets: The E_{2g} phonon generates an infrared-active E_{1u} phonon and a Raman-active E_{2g} phonon, the B_{2g} phonon goes into an infrared-active A_{2u} phonon and an inactive B_{2g} phonon. The antisymmetric combinations of the acoustic modes are transformed into the optically inactive B_{2g} and the Raman active E_{2g} rigid layer modes, as shown in Figure 3 (b, c). The symmetric combinations of the acoustic modes remain A_{2u} and E_{1u} . Thus, for graphite there are 12 normal modes at the Brillouin zone centre $\Gamma = A_{2u}(IR) + B_{2g}(i.a) + E_{1u}(IR) + E_{2g}(R) + A_{2u}(ac) + B_{2g}(i.a) + E_{1u}(ac) + E_{2g}(R)$; IR is infrared active mode, i.a. is optically inactive mode, R is Raman active mode and ac is acoustic mode [24]. There are now two Raman active E_{2g} modes, each doubly degenerate. Thus, one of the Raman active modes (1580 cm^{-1}) is the stretching modes within the sheets, while the other one ($\sim 42 \text{ cm}^{-1}$) is the shear mode between the adjacent sheets.

Single wall carbon nanotubes (SWCNT) are the rolled up modification of graphene sheets capped with half the fullerene molecule. The basic structure of nanotubes consists of one or usually more graphitic sheets wrapped around one another with a hollow core. The caps are usually closed by the presence of carbon pentagons. Consequently, the tubes contain no dangling bonds. This is an intrinsic difference to graphite where open bonds are present at the edges. Due to this difference and due to the curved nature of the graphitic sheets in the tubes characteristically different vibrational properties can be expected. However, for tube with more than a few

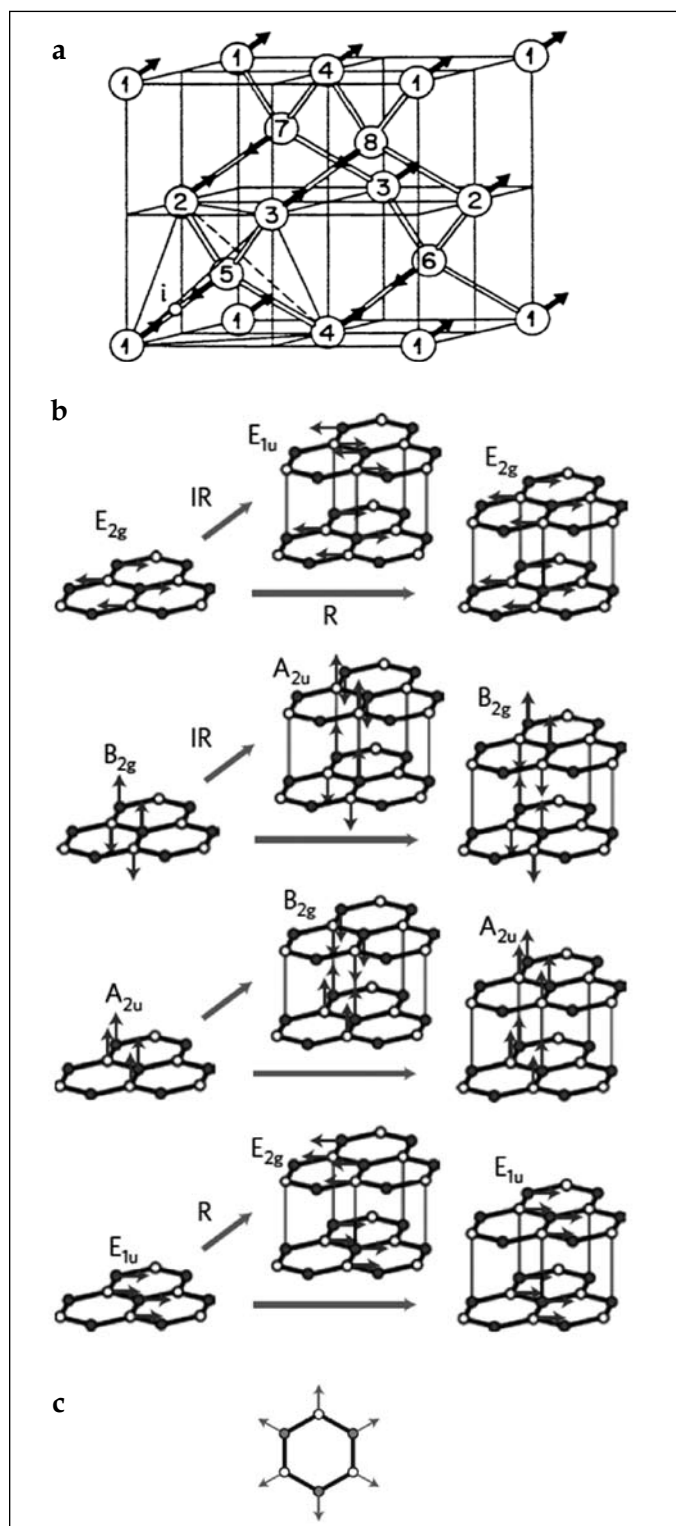


Figure 3. Modes of vibrations in (a) diamond [23] and (b) 2-dimensional graphene (left) and 3-dimensional graphite (right) [24]. Disorder activated six member ring breathing mode observed in sp^2 bonded carbonaceous materials (graphene, graphite and nanotubes) is shown in (c). [From Andrea C. Ferrari and Denis M. Basko, *Nat. Nanotechnol.*, 8 (2013) 235, with permission from Right's link copyright center with License Number: 3375300255183].

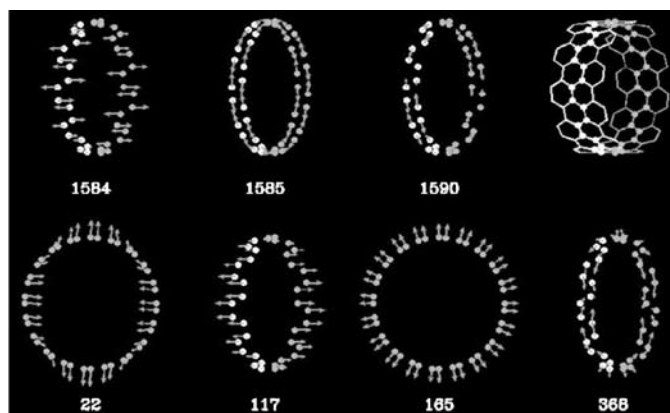


Figure 4. Raman-active normal mode eigenvectors and frequencies of a chiral nanotube. The red arrows indicate the magnitude and direction of the appropriate C-atom displacements, and the eigenvectors shown correspond to the seven most intense modes. The unit cell (blue atoms) is shown schematically in the upper right-hand corner [17]. (From A.M. Rao et al. *Science* 75, 187 (1997). with permissions from Right's Link copyright with License Number: 3375310553130).

nanometer diameter the deviation from planarity is low and therefore, the vibrational analysis of SWCNT is nearly the same as that of a graphene sheet. However, depending upon how the graphene sheet is rolled up one has arm chair, zig-zag or chiral tubes and correspondingly their symmetry is also altered. For details about the symmetry of the various kinds of carbon nano-tubes, one can refer to article by Eklund et al. [26]. The symmetry classification of the phonon modes in armchair and zigzag tubules have been studied in ref. [26] under the assumption that the symmetry group of these tubules is isomorphic with either D_{nd} or D_{nh} depending upon n is odd or even. If one considers an infinite tubule with no caps, the relevant symmetry group for armchair and zigzag tubules would be the group D_{2nh} . For armchair tubules described by the D_{nd} group there are, among others, $3A_{1g}(R)$, $6E_{1g}(R)$, $6E_{2g}(R)$, $2A_{2u}(IR)$, and $5E_{1u}(IR)$ optically active modes with nonzero frequencies; consequently, there are 15 Raman and 7 IR-active modes. All zigzag tubules, under D_{nd} or D_{nh} symmetry group have, among others, $3A_{1g}$, $6E_{1g}$, $6E_{2g}$, $2A_{2u}$ and $5E_{1u}$ optically active modes with non-zero frequencies; thus again there are 15 Raman and 7 IR active modes. The chiral nanotubes have $6A_1$, $6E_1$ and $6E_2$ optically active modes, out of which two of A_1 and one of E_1 modes have vanishingly frequencies at the Brillouin zone centre Γ . The A_1 and E_1 and E_2 modes are Raman active, while A_1 and E_1 modes are infrared active; i.e. A_1 and E_1 are Raman as well as infrared active modes. Thus, there are 15 Raman active modes and 9 infrared active modes. For the three tube types (armchair, chiral, and zig-zag) a common

general behavior is observed for both the IR-active (a) and Raman-active (b) modes. The highest frequency modes exhibit much less frequency dependence on diameter than the lowest frequency modes. Taking the large-diameter tube frequencies as reference, one observes that the four lowest modes stiffen dramatically ($150 - 400 \text{ cm}^{-1}$) as the tube diameter approaches $\sim 1 \text{ nm}$. Conversely, the modes above 800 cm^{-1} in the large-diameter tubules are seen to be relatively less sensitive to tube diameter. It should also be noted that, in contrast to armchair and zig-zag tubules, the mode frequencies in chiral tubules are grouped near 850 cm^{-1} and 1590 cm^{-1} . In case of nested tubules, the E_{2g} mode observed is observed to be split into two, one at 1592 and another at 1566 cm^{-1} . Figure 4 shows the atomic displacement as seen in the different modes of vibrations in the chiral nanotubes. Also shown in this figure is the atomic arrangement of carbon atoms in the unit cell of the nanotube [17].

4. Raman spectroscopy of typical carbonaceous materials

The Raman spectroscopic analysis of different allotropic forms of carbon is presented in this section. This includes

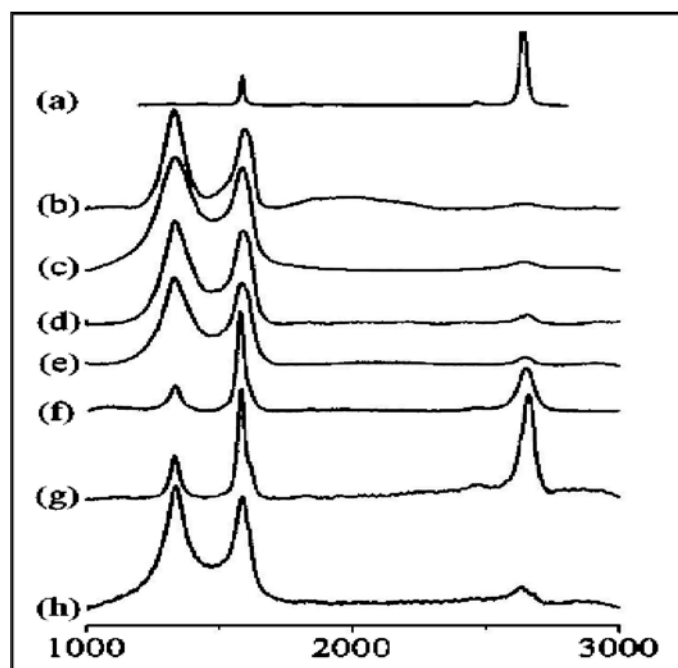


Figure 5. Room temperature Raman spectra of (a) single-layer graphene (SLG) from mechanical exfoliation of graphite, (b) reduced graphene oxide (RGO), (c) six-layer graphene (EG) from exfoliation of graphite oxide, (d) two-layer graphene nanoribbon, (e) six-layer graphene nanoribbon, (f) three-layer graphene (HG) from arc discharge of graphite in hydrogen, (g) nitrogen-doped HG and (h) boron-doped HG [7]. (Taken with permission from D. J. Late et. al. *J. Phys.: Condens. Matter* 23 (2011) 055303 from IOP Publication).

carbon nanotubes, (including single wall, double wall and multiwall), 2 dimensional graphene, 3-dimensional graphite and diamond including (CVD diamond and nano-diamond which has impurity of sp^2 carbon in the sp^3 carbon network. Below we give description of the spectral analysis of each of these types.

4.1 2D graphene and 3D graphite:

Graphene is the two-dimensional building block for sp^2 carbon allotropes of every other dimensionality. It can be stacked into three-dimensional graphite, rolled into one-dimensional nanotubes, or wrapped into zero-dimensional fullerenes. Thus, the Raman structure of graphene is very much similar to other sp^2 bonded carbon based materials e.g. graphite, carbon-nanotubes etc. The spectra of all carbon-based materials show quite a few prominent features, regardless of the final structure. However, the shapes, intensities and positions of these peaks give a considerable amount of information, often comparable to that obtained by other competing techniques that are more complicated and destructive in nature. Figure 6(a) shows the Raman spectra of single-layer graphene, prepared by mechanical exfoliation of graphite which depicts the G band at 1584 cm^{-1} and an intense G' band at 2635 cm^{-1} , as can be seen from spectrum. It however, does not exhibit the defect-related D band (please refer below for explanations) indicating highly crystalline sample. This is a characteristic feature of single layer graphene (as seen in Fig. 6(a), where G' band is present without the D band. The Raman spectrum of Single-layer RGO as shown in Figure 6(b), has a G band at 1591 cm^{-1} , D band at 1329 cm^{-1} and a weak G' band at 2644 cm^{-1} . Additionally, broad band at $\sim 2000 \text{ cm}^{-1}$, whose origin is not very clear, is also observed. The six-layer graphene (EG) sample prepared by thermal exfoliation of graphite oxide exhibits the G band at 1583 cm^{-1} , the D band at 1333 cm^{-1} and the G' band at 2640 cm^{-1} , as depicted in figure 5(c)). The two- and six-layer graphene nano-ribbon synthesized by using unzipping of double-walled and multi-walled nanotubes show the G band at 1585 cm^{-1} and 1581 cm^{-1} respectively and a D band around 1329 cm^{-1} (see seen in the Raman spectra figure 5(d) and figure (e)). Figure 5 (f) shows the Raman spectra of three-layer graphene synthesized from arc discharge of graphite in hydrogen (HG). Figure 5(g) shows Raman spectra of nitrogen-doped HG and (h) shows Raman spectra of boron-doped HG sample.

It may be noted that the Raman spectrum of graphite and multilayer graphene mainly consists of two fundamentally different sets of peaks; one such as D, G, G' (present also in SLG) due to in-plane vibrations; and others, such as the shear (C) modes and the layer-breathing modes

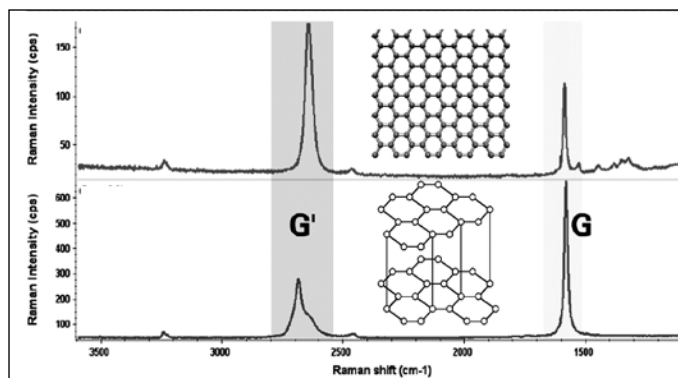


Figure 6: Comparative Raman spectra of single-layer Graphene and bulk graphite [21]. (with permission from Thermo Scientific Application Note 51901, 2010).

(LBMs), due to relative motions of the planes themselves, either perpendicular or parallel to their normal. The low-frequency E_{2g} mode in graphite is observed at $\sim 42 \text{ cm}^{-1}$ [19], and is often called as mode C. It is however noticed that this mode scales with the number of layers. The absence of the C peak is in principle the most direct evidence of SLG, but most often the C-peak frequency is well below the notch and edge filter cut-off of many spectrometers, particularly those used for production-line monitoring. Moreover, it is not warranted to use the absence of a particular peak as a characteristic of SLG, because one can never be sure why something is absent; on the contrary one can always justify the presence of a peak. G' peak, as observed in the above spectra is a D peak overtone, also often called as 2D peak, and is related to the two dimensionality of graphene sheet, originating from a process where momentum conservation is satisfied by two phonons with equal and opposite wave vectors, where no defects are required for its activation. It is for this reason that Raman spectrum of single layer graphene and single crystal graphite (as will be discussed below) has 2D peak even when D peak is absent. As will be seen later, it is observed in most of the sp^2 bonded carbonaceous materials.

The Raman spectrum of bulk graphite has several bands in the spectrum and the G band appears at $\sim 1582 \text{ cm}^{-1}$. The graphite is composed of sp^2 bonded graphene layers stacked together by weak van der Waals forces between the planar sheets. A comparative spectra showing the Raman features of single layer graphene and bulk graphite is shown below in Figure 6. There is a significant change in the shape and intensity of the G' peak of graphene compared to the bulk graphite. The G' peak in bulk graphite consists of two components G'_1 and G'_2 latter changing with roughly $1/4$ and $1/2$ of the height of the G peak, respectively. Graphene has a sharp G' peak roughly four times more intense than the intensity of G peak [27].

For more than five layers, the Raman spectrum becomes hardly distinguishable from that of bulk graphite. Thus, Raman spectroscopy can clearly distinguish between a single layer, bi-layer and a FLG (few layer graphene (less than five)). This is so, because the Raman mechanism that gives rise to this peak is closely linked to the details of the electronic band structure; the latter changing with N , and the layers relative orientation. Also, the Layer-breathing modes are observed in the Raman spectra of upto few layers in graphene, through over-tones and combination modes appearing in the range $80\text{--}300 \text{ cm}^{-1}$ (not shown). The C peak and LBMs are a direct probe of N (the number of layers), as these vibrations represents out of plane motion.

4.2 Carbon nanotubes:

Due to their unique mechanical, electrical and thermal properties, carbon nanotubes are one of the most active research areas in the field of nanoscience and nanotechnology. As mentioned before, carbon nanotubes are basically rolled up graphene sheets of carbon atom that have been sealed to form hollow tubes, and can be categorized into single wall, double wall and multi wall carbon nanotubes. The single-wall carbon nanotubes (SWCNT) are cylindrical tubes with a outer wall diameter in the range $\sim 1\text{--}2 \text{ nm}$, the double-wall carbon nanotubes (DWCNT) has a second layer of graphene wrapped around an inner-wall carbon nanotube and the multi-wall carbon nanotubes (MWCNT) are made up of many such layers of graphene wrapped around the core tube [21]. The Raman spectrum of a SWCNT is very much similar to that of graphene, which is not too much unexpected as it is basically a rolled up graphene sheet. Figure 7 shows the Raman spectrum of a SWCNT with well defined G (in-plane vibration mode), G' and D bands as it is also present in graphene and graphite. One clearly observes

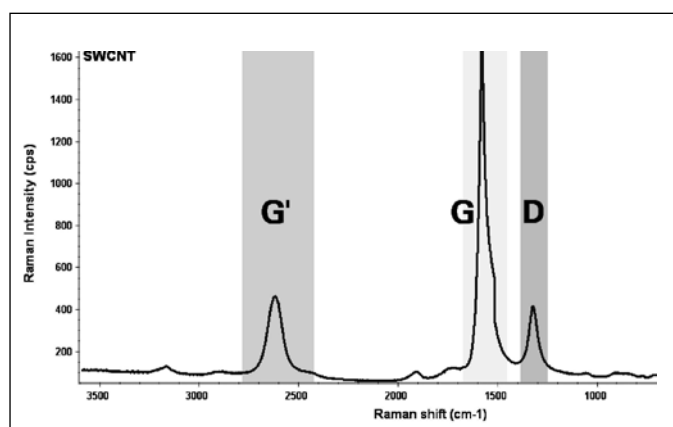


Figure 7: Raman spectrum of SWCNTs with various prominent bands labeled [21]. (With permission from Thermo Scientific Application Note 51901, 2010).

a shoulder peak near G band, which is due to stresses generated due to curved surface of graphene sheet. The doubly degenerate E_{2g} mode, as described in the section above, gets split into two components, one parallel to the strain axis and another perpendicular to it (some people denote it by G^+ and G^-). The extent of splitting depends on the curvature, which is largest when the tubes under consideration are single wall carbon nanotubes [25]. The disorder band or defect band around 1350 cm^{-1} (D band) is also very prominent. This peak is due to the breathing mode of six atom ring and requires defects for its activation, and indicates the presence of disorder in graphene sheet, as mentioned earlier. The position of this peak is highly dispersive and its position varies strongly with the excitation energy of the incident photon. The intensity of D band relative to G band is often used to determine the quality of nanotubes. The peak at 2700 cm^{-1} (also known as G' band) is also quite often used to quantify the defects. There is another sequence of bands which appear at the low frequency end of the spectrum which is known as Radial Breathing Mode or RBM bands. The atomic displacement associated with this mode is described in the lower panel of Figure 4 discussed in section-3. This RBM band is very unique to SWCNTs and its frequency is inversely proportional to the diameter; it can be used to determine the nanotube diameter d using the following relation:

$$d\text{ (nm)} = 248/\omega = 248/184 = 1.3\text{ (nm)}$$

The MWCNTs shows similar spectra as those of SWCNTs, difference being only the absence of RBM modes and a more prominent D band in MWCNTs (Fig. 4). The RBM mode is absent because atomic displacement associated with outer nanotubes cancel out contributions associated with the inner nanotubes. A comparison of the D band indicates that the intensity is very high in MWCNT compared to SWCNT, indicating the extent of disorder in

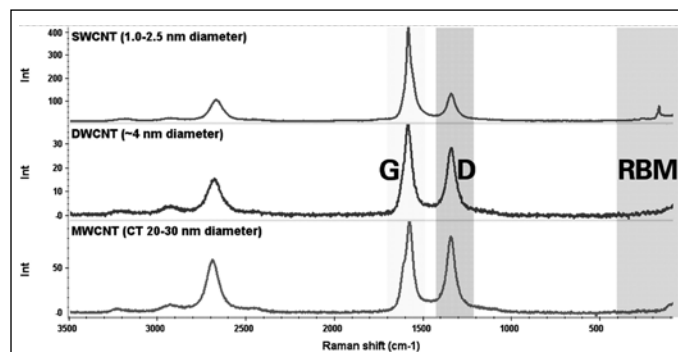


Figure 8 Comparison of Raman spectra of SWCNTs, DWCNTs, and MWCNTs (With permission from Thermo Scientific Application Note 51901, 2010).

the MWCNT is also more. Figure 8 shows the comparative Raman spectra of samples of SWCNTs, DWCNTs, and MWCNTs. It is clearly observed that the RBM mode completely disappears in both the DWCNT and MWCNT and more importantly the G band gets split into two peaks (the extent of splitting is different in all these tubes) and G' bands get equally intense with larger number of layers.

4.3 Diamond:

Diamond has four fold coordinated sp^3 carbon atoms forming an extended 3D network. Raman spectroscopy, as mentioned previously, shows only one mode, which appears $\sim 1332\text{ cm}^{-1}$. It is this peak which can decisively tell whether the material under consideration is diamond or not. It is because of this very peak that Raman spectrometer is commonly used by many people including gemologist. In research, the impurity free diamond for industrial application is synthesized using chemical vapour deposition, where one cracks methane under abundance of hydrogen. However, the concentration zone of gases used in this process is very much limited. A slightly higher concentration of methane, which is a precursor gas for diamond growth, may lead to non-diamond growth [28]. Figure 9 (a) shows the Raman spectra of CVD diamond grown under 20, 40 and 60 torr pressure, while for those grown at pressure of 80 and 120 torr are shown in figure 9 (b). The 1332 cm^{-1} peak, which is a characteristics for pure diamond is present in all the samples. However, for samples grown at higher pressure (say 80 and 120 torr) the peak at 1380 and 1530 cm^{-1} due to the non-diamond contribution are also observed. This non-diamond is mainly coming from the simultaneous growth of sp^2 bonded carbonaceous matter. While comparing these spectra with those with the sp^2 bonded carbon samples discussed above, we notice two differences. One is that the G-peak is split into two peaks, and another is that the G-position is down shifted considerably. Though the intensity of G-peak is quite high, the Raman scattering efficiency of sp^3 bonded carbon is at least 50 higher than that of sp^2 bonded carbon [29]. Due to this reason even small concentration of sp^2 bonded carbon present in CVD diamond shows very strong signal. It may be quite possible that the splitting of G-band is due to the strain generated in the sp^2 bonded clusters present between the sp^3 bonded diamond crystallites. The lower position of G-peak again is quite interesting. For an increasing number of defects, including bond length and angle disorder at the atomic scale, present in this case, the phonon modes will soften, particularly the G peak [27]. If this is the case, then the intensity of D-peak should have been very strong. However, as may be noted that for more disorder, clusters become smaller and smaller and the rings getting fewer

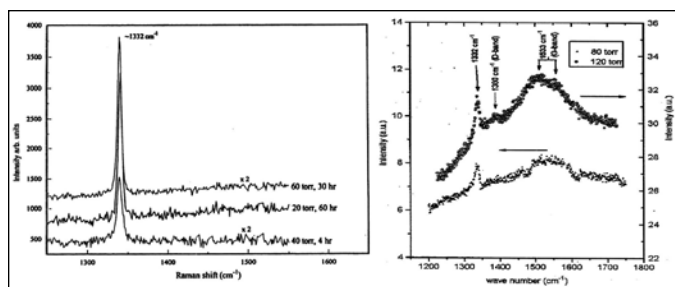


Figure 9. Comparative Raman spectra of CVD diamond films deposited at different deposition pressure [28]. (From M. Pandey et al., *J. Alloys Compd.* 333 (2002) 260 with permission from Right's Link copyright centre; License Number: 3355200480869).

and more distorted, until they begin to open up. Thus, the D peak strength is now proportional to the probability of finding a sixfold ring in the cluster, i.e. to the cluster area [19]. In the CVD grown diamond, the non-diamond component in the form of D-peak and the G-peak therefore behaves exactly opposite to the case of graphite. The Raman spectrum for nanocrystalline diamond, as shown in Figure 8, is very much different from that of CVD grown diamond discussed above. In addition to peak at 1332 cm^{-1} , one observes an additional shoulder peak at slightly lower frequency. The Raman peak in hexagonal diamond is observed to vary from 1315 cm^{-1} to 1326 cm^{-1} depending on the size of the particles. The shoulder peak is therefore possibly due to the presence of hexagonal diamond, which may also be present in the nanophase materials. The broad band at $\sim 500\text{ cm}^{-1}$ is indicative of amorphous sp^3 bonded carbon. The finite-size effect in the nanocrystalline

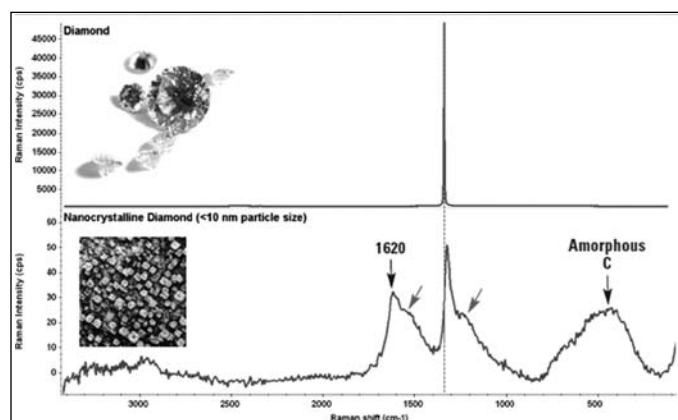


Figure 10: Comparative Raman spectra of diamond and bulk nanocrystalline diamond [21]. (Taken with permission from Thermo Scientific Application Note 51901, 2010).

diamond results in additional density of states responsible for this peak. Even the non-diamond contribution, showing a strong peak at 1620 cm^{-1} and a shoulder at 1530 cm^{-1} . The shoulder peak is nearly at identical position to what

is observed for the non-diamond signal in case of CVD grown diamond samples indicates sp^2 bonded carbon at surfaces. The peak at 1620 cm^{-1} is possibly due to the sp^2 bonded carbon in the form of chains [19].

5. Conclusions:

Raman spectroscopy is a very powerful technique to characterize carbon related materials and offers a precise and non-destructive technique to identify various kinds of carbonaceous materials. This is only possible because different polymorphs have different characteristic vibration frequencies observed in the respective Raman spectrum. Thus, Raman spectrum is well suited to detect even small changes in structural morphology of carbon based materials making it an essential tool for many material scientists working with carbon related materials.

Acknowledgements:

The authors would like to thank Prof. C. N. R. Rao, FRS (ICMS & JNCASR Bangalore) for constant support and encouragement. One of the authors Dr. Mukesh Pandey would also like to acknowledge Dr. S.M. Sharma, Associate Director Physics Group and Head, High Pressure & Synchrotron Radiation Physics Division (HP&SRPD) and Dr. R.J. Kshirsagar, Infrared Spectroscopy Section, HP&SRPD for their constant support and encouragement. One of the authors, Dr. D. J. Late, would like to thank DST (Government of India) for Ramanujan fellowship. The work was Partially supported by CSIR-NCL-MLP project grant 028626.

References:

1. C. N. R. Rao, A. K. Sood, K. S. Subrahmanyam and A. Govindaraj, *Angew. Chem. Int. Ed.* **48** (2009) 7752.
2. C. N. R. Rao, B. C. Satishkumar, A. Govindaraj, Manashi Nath, *Chem Phys Chem*, **2** (2001) 78.
3. D. K. Palit, A.V. Sapre, J. P. Mittal, C. N. R. Rao, *Chem. Phys. Lett.* **195**(1992) 1.
4. C. N. R. Rao, K. S. Subrahmanyam, H. S. S. R. Matte, B. Abdulhakeem, A. Govindaraj, B. Das, P. Kumar, A. Ghosh, D. J. Late, *Sci. Technol. Adv. Mater.* **11** (2010) 054502.
5. R. B. Sharma, D. J. Late, D. S. Joag, A. Govindaraj, C. N. R. Rao, *Chem. Phys. Lett.* **428** (2006) 102.
6. D. J. Late, A. Ghosh, B. Chakraborty, U. V. Waghmare, A. K. Sood, C. N. R. Rao, *J. Exp. Nanosci.* **6** (2011) 641.
7. D. J. Late, U. Maitra, L. S. Panchakarla, U. V. Waghmare, C. N. R. Rao, *J. Phys. Condens. Matter.* **23** (2011) 055303.
8. D. J. Late, A. Ghosh, K. S. Subrahmanyam, S. B. Krupanidhi, L. S. Panchakarla, C. N. R. Rao, *Solid State Commun.* **150** (2010) 734-738.
9. M. A. Pimenta, G. Dresselhaus, M. S. Dresselhaus, L. G. Cançado, A. Jorio and R. Saito, *Phys. Chem. Chem. Phys.* **9** (2007) 1276.

10. J. Robertson, *Prog. Solid State Chem.* **21**(1991) 199
11. J. Robertson, *Adv. Phys.* **35** (1986) 317.
12. M. S. Dresselhaus, G. Dresselhaus, and P. C. Eklund, *Science of Fullerenes and Carbon Nanotubes* Academic Press, New York **1996**.
13. D. S. Bethune, G. Meijer, W. C. Tang, H. J. Rosen, W. G. Golden, H. Seki, C. A. Brown, and M. S. De Vries, *Chem. Phys. Lett.* **179** (1991) 181.
14. S. A. Solin and A. K. Ramdas, *Phys. Rev. B* **1**, (1970) 1687.
15. M. A. Tamor and W. C. Vassel, *J. Appl. Phys.* **76**, (1994) 3823.
16. A. C. Ferrari and J. Robertson, *Phys. Rev. B* **61**, 14 095 (2000).
17. A. M. Rao, E. Richter, S. Bandow, B. Chase, P. C. Eklund, K. A. Williams, S. Fang, K. R. Subbaswamy, M. Menon, A. Thess, R. E. Smalley, G. Dresselhaus, and M. S. Dresselhaus, *Science* **75**, 187 (1997).
18. F. Tuinstra and J. L. Koenig, *J. Chem. Phys.* **53**, 1126 (1970).
19. R. J. Nemanich and S. A. Solin, *Phys. Rev. B* **20**, 392 (1979).
20. P. Lespade, A. Marchard, M. Couzi, and F. Cruege, *Carbon* **22** (1984) 375.
21. Joe Hodkiewicz, *Characterizing Carbon Materials with Raman Spectroscopy*, Application Note 51901, Thermo Scientific, **2010**.
22. J.C. Decius and R.M. Hexter, 'Molecular vibrations in crystals', Mc Graw Hill. New York, **1977**.
23. P. Bruesch, 'Phonon theory and experiments' vol 2, Springer-Verlag, Berlin, **1986**.
24. R. J. Nemanich, G. Lucovsky and S. A. Solin, *Solid State Commun.* **23** (1977) 117.
25. Andrea C. Ferrari and Denis M. Basko, *Nat. Nanotechnol.*, **8** (2013) 235.
26. P. C. Eklund, J. M. Holden, and R. A. Jishi, *Carbon* **33** (1995) 959.
27. A.C. Ferrari, *Solid State Commun.* **143** (2007) 47.
28. a) A.K. Sikder, A.P. Jacob, T. Sharda, D.S. Misra, M. Pandey, D. Kabiraj, D.K. Avasthi, *Thin Solid Films* **332** (1998) 98; b) T. Sharda, D.S. Misra, D.K. Avasthi, *Vacuum* **47** (1996) 1259; c) M. Pandey, A.K. Tyagi and R. D' Cunha, *J. Alloys Compd.* **333** (2002) 260.
29. N. Wada, P.J. Gaczi, A. Solin, *J. Non-Cryst. Solids* **35-36** (1980) 543.



Dr. Dattatray J. Late has completed his BSc, MSc and PhD (2008) degree in Physics from University of Pune (India). After completing his PhD with Prof. D. S. Joag, he joined as a DST Post-doctoral Fellow on Nanoscience & Technology with Prof. C. N. R Rao at JNCASR, Bangalore (2008-2010). Then he moved to Department Materials Science and Engineering, Northwestern University (USA) Chicago, as Postdoctoral Fellow to work with Prof. Vinayak P. Dravid (2010-2012). Currently he holds a position of DST Ramanujan National Fellow and AcSIR Assistant Professor at CSIR-National Chemical Laboratory. His current research interest includes "Synthesis of atomically thin nanosheets of graphene and 2D inorganic layered materials for Nanoelectronics device applications such as Transistors, Photodetector, gas sensors, supercapacitor, Light Emitting Diode, Field Emission, and catalyst for water splitting etc. and Raman spectroscopy". He has authored or co-authored more than 60 research papers in international journals. His current google scholar h-index is 18 with total citations >1250.



Dr. Mukesh Pandey is currently working as a scientific officer at High Pressure and Synchrotron Radiation Physics Division, Bhabha Atomic Research Centre (BARC), Mumbai. He did his M.Sc. in Physics from IIT Delhi and joined BARC through 37th Batch of Training School (1993). He carried out M. Tech in Materials science from IIT Kanpur and completed his Ph. D. from Mumbai University in the year 2003. Currently he is working on Raman and Infrared spectroscopy of Novel Materials. He has more than 50 papers in national, international journals and conferences.

Silicon Carbide Research and Development in Nuclear Industry: Silicon Carbide on Graphite Rod by Induction Assisted Chemical Vapor Deposition process using Hexamethyldisilane (HMDS) as a Single Source

J. Selvakumar¹, K. Ramadurai², D. Sathiyamoorthy²

¹KNRPC, NRB, BARCF, Kalpakkam 603102.

²Powder Metallurgy Division, Materials Group, BARC, Vashi, Navi Mumbai 400 703

E-mail: jselva@barc.gov.in

Abstract

Though energy flows constantly in and out of the earth's surface environment, it's the most significant challenge confronting mankind today. The scarcity of material and techniques, we couldn't mine her effectively. However, to get energy through nuclear reactions and the safe operation of reactors, various materials have been developed day by day. Since, next generation nuclear power plants will be exposed to very high temperature, intense neutron radiation, corrosive environments, and mostly all three at once. To safeguard the situation, among the materials, owing to the superior properties, silicon carbide (SiC) based materials are preferred. Insight of material development, here we depict the nanocrystalline SiC coating on graphite by induction assisted CVD using halogen free single source. The phase purity and surface morphology of the deposit will be hashed out in details. Prior to the deposition of SiC by CVD process, the scope, preferred properties, and the necessity of SiC in the nuclear industry is given emphasis.

Introduction

If there is a way you could save some lives a year and simultaneously halt global warming, reduce air and water pollution and develop strong, reliable energy sources, why wouldn't you serve it? Merely to go thither, we will need to substantially step-up our research and development into energy production and energy efficiency. This can be accomplished through acquiring more efficient materials, industrial operations and engineering sciences. In the future, energy program, with advanced renewable energy systems the next generation thermal nuclear reactor designs are also being pursued. In general, the challenges faced in designing and selecting materials for nuclear reactor applications are those associated with materials under the extreme conditions of high radiation flux, combined with high temperatures and chemical attack (corrosion) from coolant or from fission products. In high-temperature gas-cooled reactors (HTGRs), which are meant to provide nuclear-energy options for supplying high-temperature process heat, are graphite-moderated and helium-cooled. The focus here is on materials inside the reactor pressure vessel (RPV), specifically the clad and fuel. Nevertheless, on that point are significant materials issues outside of RPV as well. For example, in existing LWR's clad, the external surface is exposed to a corrosive, environment due to the steam reaction at elevated temperatures [1], while the internal surface is subjected to the rapidly changing fuel composition as the fissile material is converted into fission products of significantly different chemistry. Efforts are made to increase the efficiency of reactors at high

temperatures with higher burn-up and lifetime extension for future fuel cycles. Consequence, nuclear power has been a reliable source of electricity in many countries for decades and enabling global access to energy. Still, the materials are in search to build new reactors with improved safety (especially in the light of the Fukushima accident), reliability and efficiency.

Silicon carbide (SiC) is a semi-conductor material with suitable properties for high-power, high-frequency and high-temperature applications. This almost an opening statement may be found in many publications of SiC [2-5]. In addition, properties such as high thermal conductivity, high hardness and stiffness, mechanical strength at elevated temperature, low coefficient of thermal expansion, good dimensional stability under irradiation, small neutron capture cross sections, lower density than other ceramics and resistance to wear and abrasion make SiC ideally suited for a vast number of applications, especially in nuclear reactors and alternative energy sectors. Moreover, the SiC research findings reveal that the growth techniques and crystalline size of SiC play an important role in electronics and nuclear applications [3]. In support of this, computational studies have shown that the decrease in the grain size of SiC to the nanoscale can considerably increase the toughness and strength of the material. The outcomes indicate that under lower energy irradiations, nanocrystalline (nc-) SiC has superior radiation resistance than micrometer-scale textures. In the present article, the main perspective is devoted to the presentation of general considerations about SiC-chemical vapor deposition (CVD)

process and precursors, relevant chemistry, thin film- and nanostructure- material properties, and their real and prospects in future energy applications.

SiC: Material and Structure

Silicon carbide is one of the few compounds in nature made out by their strongly expressed one-dimensional polymorphism, termed polytypism. It exists in a variety of short- and long- period lattices with a different structure [6]. Most common short period polytypes (Fig. 1) are the cubic (3C-SiC), the hexagonal (2H-, 4H- and 6H- SiC) and the rhombohedral (15R-SiC). The chemical bonding in SiC is not only covalent but also slightly ionic due to the differential electro-negativity between silicon and carbon. Therefore, the stable SiC is obtained only at the stoichiometric composition of Si to C. The cubic form of β -SiC is believed to be more stable than α -SiC below 2373 K, although some studies dispute this finding. The SiC structure is composed of identical polar layers of Si_4C or C_4Si coordination tetrahedral linked through their vertices to form the SiC framework. The possibility of polytypism in SiC structures is due to the formation of various stacking sequences in the Si-C close- packed atomic planes.

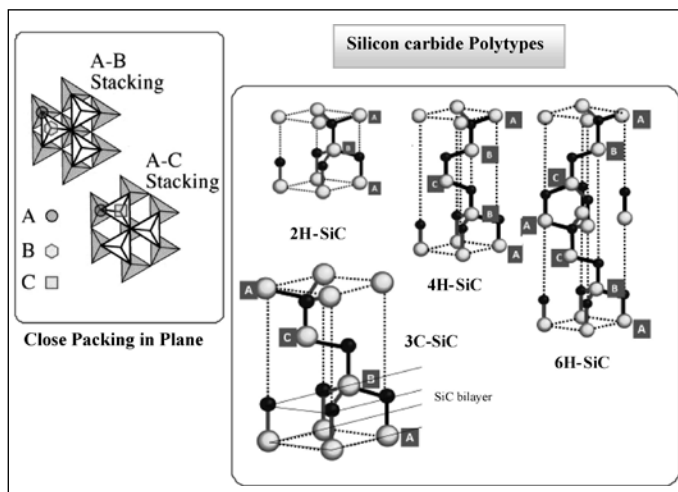


Fig. 1 Silicon carbide polytype structures. Polytypes of SiC are formed by those periodic stacking sequences of bilayers that produce tetrahedral sheets [7].

The primary concern on SiC at high temperature applications is the polytype transformations since their microstructure or properties change. Despite intense research, the transformations in SiC are still not properly read. For instance, the common $\beta \rightarrow \alpha$ (cubic to hexagonal) transformation at above 2373 K is noted. In contrast, Krishna et al. reported that 2H-SiC (α -SiC) can be easily transformed to 3C-SiC (β -SiC) on annealing in argon at a temperature above 1673 K [8]. Together with temperature

dependence, the effect of impurities or deviation from C:Si stoichiometry also plays a role in polytype stability. To bring SiC into real-time applications, it is indispensable to control polytypes during crystal or film growth. Various growth experiments were conducted using vapors or liquids as sources to set the stability region for SiC polytypes. Mostly, the resultant polytype was observed to depend on both the rate of growth and the temperature. Jepps and Page [9] stated the possible formation of β -SiC with high super saturation/non equilibrium conditions in the temperature range 1273–3023 K and subsequent transformation to α -SiC. In addition, they derived the stability diagram of polytype as a function of temperature and suggested that β -SiC is the initial polytype to appear during growth at almost all temperatures, no transformation inclination in the temperature range 1673–1873 K, and more stability than other polytypes. Table 1 lists main physical and chemical properties of various structural types of SiC at room-temperature. The lattice parameter and density of β -SiC at room-temperature is 0.4358 nm and 3.21 g/cm³, respectively. Except carbon, group IV elements have considerable energy differences between sp^2 and sp^3 bonds, which suppress the realization of graphite phase. SiC, in fact, also has a significant energy difference between the sp^2 and sp^3 bonds. Despite these facts, SiC nanotubes have been successfully synthesized by different groups.

Table 1 Physical and Chemical properties of selected polytypes of SiC

Polytype	2H	3C	4H	6H
Density	3.219	3.215	3.215	3.215
Band gap (eV)	3.300	2.390	3.263	3.023
Lattice parameter (nm)	a= 0.3081,	a=0.4358	a=0.3081,	a=0.3081,
Space group	c=0.5031		c=1.0061	c=1.5092
Hexagonality (%)	P6 ₃ mc	F4 ₃ m	P6 ₃ mc	P6 ₃ mc
Stacking order	100	0	50	33
Thermal conductivity (W cm ⁻¹ K ⁻¹)	AB	ABC	ABCB	ABCACB
Electron mobility (cm ² v ⁻¹ s ⁻¹ , 300K)	-	≤1000	≤850	≤450
Hole mobility (cm ² v ⁻¹ s ⁻¹ , 300K)	-	≤40	≤120	≤100

Existing SiC Sources and Development Processes

The key deposition techniques which have been frequently used in nanofabrication are the sol-gel, atomic layer deposition (ALD), electrochemical deposition (ECD) and chemical vapor deposition (CVD). Sol-gel was used for the manufacture of porous nanostructures for sensing applications, whereas ALD was handy in

realizing highly ordered, defect free layered structures. The conventional ECD was proven to be useful in the fabrication of nanowires and nanorods. The CVD has extensively been employed in the fabrication of nanotubes (NTs). Several methods have been employed to grow SiC nanomaterials, the most comfortable way is the CVD method. Nevertheless, conventional CVD process (Fig. 2) requires a high deposition temperature than sol-gel or carbothermal reduction processes. Thus, many research groups have tested and found suitable organosilane precursors for growing SiC nano- and thin film- materials. More importantly, CVD method found higher efficiency than NT-confined reaction, arc-discharge, sol-gel and high frequency induction heating.

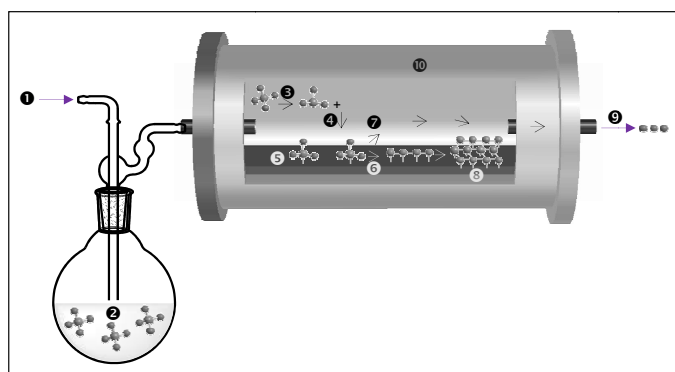


Fig. 2 Typical CVD process: ① Carrier Gas Inlet ② Source Material ③ Transport ④ Adsorption ⑤ Reaction ⑥ Diffusion ⑦ Desorption ⑧ Nucleation and Growth ⑨ Transport ⑩ CVD chamber

Gas-phase deposition is used for the nanocrystalline SiC film preparation in the known different physical and chemical version such as reactive magnetron sputtering, nonreactive magnetron sputtering, hybrid laser-magnetron synthesis, pulsed laser synthesis, plasma enhanced CVD, low pressure and hot-wire CVD, and other procedures. Typically, SiC homo epitaxial growth is done using CVD with silane (SiH_4) as the silicon source and light hydrocarbons as the C source. The growth temperature and pressure are usually between 1500 to 1650°C and 100 - 1000 mbar, respectively. In the SiC epitaxial growth process, the primary event is the formation of silicon droplets. These droplets fall down along the substrate, but normally evaporate quite quickly; nevertheless, their contact with the substrate will badly affect the growing epitaxial layer, making it useless for devices. A safer path is to use the rules of chemistry by preventing the formation of the silicon droplets by using the strange element that binds more strongly to silicon than hydrogen. The next option is to use here would be a halogen contain sources. The standard bond enthalpies for the Si-H, Si-Si, Si-F, Si-Cl, Si-Br, and Si-I bonds are 376, 376, 597, 400, 330, and 234

kJ mol^{-1} , respectively. Fluorine is not a serious prospect, since it would form HF in the operation, which etches the quartz glass in the CVD reactor; neither is iodine, since it forms too weak bonds to Si to form droplets effectively.

The fact that chlorinated compounds are already available in high purity and at depressed cost, due to their broad role in the silicon manufacture, makes chlorine the obvious choice than bromine also for SiC. However, up to ~8% free silicon co-deposition was reported when using methyltrichlorosilane (MTS) as the source. In addition, MTS decomposes under typical CVD conditions producing corrosive HCl, SiHCl_3 , SiCl_3 , SiCl_4 , and CH_4 , as well as other silanes and hydrocarbons. The high deposition temperature results in introducing structural defects in the layers and results in difficulties to work with the reactor in the field. As like fluorine, chlorine too etches the metallic-, silicon-substrates and CVD reactors. In nuclear perspective, the MTS CVD gas phase products of chlorine can attack the nuclear fuel kernel and result in uranium dispersion into the surrounding buffer. The primary failure mechanism in TRISO-coated particles is a metallic fission product attack of SiC. In fact, under a thermal gradient, rare earth metals move toward the cold side of the particle, concentrate and degrade the SiC. The traces of chlorine that originate from the MTS act as a path for the penetration of metallic products through the coating. In addition, the reactivity of chlorinated organosilane differs from simple organosilanes because Si-Cl bonds are stronger than both Si-H and Si-C (376 kJ mol^{-1}) bonds. On the other hand, MTS is more favored because it is liquid, inexpensive, has a favorable C to Si stoichiometric ratio, and is inherently safer than silane. It delivers an added advantage of containing chlorine, which can improve epitaxial growth. The disadvantage of MTS is its fixed ratios of Cl/Si=3 and Si/C=1. Since, the optimized growth of thin film may take independent control of these proportions. With all, there are nearly 100 different potential side reactions when decomposing MTS thermally in the presence of hydrogen at temperatures above 1400 K; the formation of trichlorosilane and methyl radicals are most thermodynamically plausible. The presence of chlorine during decomposition and nucleation is believed to suppress unwanted terrace growth, decreases gas phase nucleation of SiC, reduces the formation of silicon droplets on the surface, and improves the quality of the film. However, as summarized earlier, MTS has the disadvantages such as the formation of toxic gas phase intermediate, releasing and handling of by-products, possible chlorine migration and reaction with the kernel and requires high temperature for thermal decomposition. In addition, the hydrogen chloride production and adsorption on the surface at high temperature may increase

the porosity in the films. The chlorine co-deposition with SiC observed when using MTS as source even at 1373 K. The interaction of HCl with the SiC surface is of special interest since this species is a major byproduct of the deposition process. In addition, several studies provide evidence that HCl inhibits the deposition-based etching mechanism. On the other hand, at high temperatures (~ 1497 K), the effect of HCl disappears. Few reports suggest that Cl bonds to Si atom sites on the SiC surface and the major etching product is SiCl_4 with smaller amount of CCl_4 at high temperatures. Despite the advantages of HCl in SiC deposition, it drastically reduces the SiC growth rate at temperatures between 1310 and 1450 K. As of interest here and in nuclear materials development programs, it is better to avoid halogen-containing chemicals for any reaction. Consequently, it is worthy to use a source that is not pyrophoric, halogen free, and contains both silicon and carbon atoms as single molecules and decomposes at low temperatures into the film of stoichiometric SiC.

A foremost factor in the development of interest in polycarbosilanes in recent years has been the potential for their use as sources to SiC, mainly as precursors of continuous ceramic fiber. The polymer to ceramic transformation process enabled significant technological breakthroughs in ceramic science and technology, such as the development of ceramic fibers, coatings, or ceramics stable at ultrahigh temperatures (up to 2000°C) with respect to decomposition, crystallization, phase separation, and creep. The polymer precursors represent inorganic/organometallic systems that provide ceramics with a tailored chemical composition and a closely defined nanostructural organization by proper thermal treatment (curing and thermolysis processes) under a controlled atmosphere. More interestingly, the silicon carbide polymer precursor shows the ability to generate crystalline single-phase with 1:1 Si to C ratio. Thanks to Whitmarsh and Interrante^[10] for the synthesis of a polycarbosilane that had a 1:1 Si to C ratio, with H as the only other component. The precursor was obtained by Grignard coupling of chloromethyltrichlorosilane, followed by reduction with LiAlH_4 , which had a relatively low molecular weight, hyper-branched with an overall composition of " $[\text{SiCH}_4]_n$ ". The precursor, called AHPCS, commercially usable and is under evaluation as a coating material, a binder for ceramic powder, and a matrix source for polymer-derived, ceramic matrix composites through polymer infiltration and pyrolysis. Preparation of linear polycarbosilane with hydrogen as the only main chain substituent has also been achieved by the ring opening polymerization (ROP) of 1,1,3,3-tetrachloro-1,3-disilacyclobutane (TCDS CB), followed by reduction with

LiAlH_4 . Like its hyperbranched analogue AHPCS, this can also be used to produce nanocrystalline SiC (1:1) in high yield at 1000°C . Alas, its high cost and difficult synthesis precludes its effective use as a SiC source. More recently, polymethylsilane (PMS; Fig. 3), $-\text{[MeSiH]}_n-$, was found to provide access to phase and chemically pure SiC fibers. In addition, because the worldwide area of SiC polymer precursors has been reviewed in detail, we concentrate here only on those precursors and processing methods (let us say CVD) that provide pure SiC. In fact, two precursor type, such as polymethylsilane (PMS) and polysilaethylene (PSE), have been identified and these precursors can give nearly phase pure SiC. Unfortunately, in some forms these polymers are highly susceptible to air oxidation.

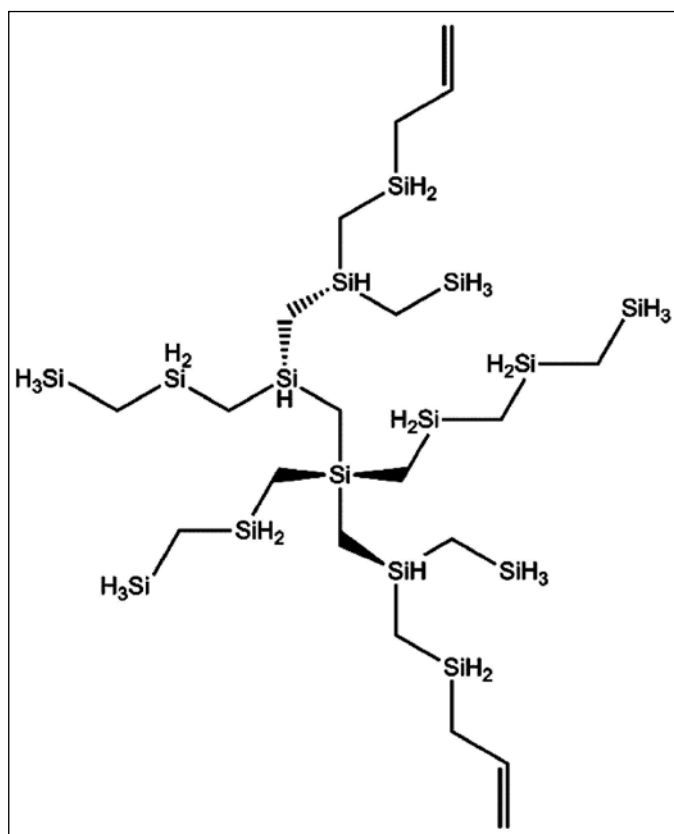


Fig. 3 Molecular structure of polymethylsilane (PMS)

The above said approaches, chlorinated and polycarbosilane, are merely a promising means to grow SiC, but it is not the ultimate way to grow SiC. The standard pattern is needed to fix using an ideal source of SiC in near future. When I started my research in the field of SiC, dream to have a compound such as 1,3,5-trisilabenzene ($\text{C}_3\text{Si}_3\text{H}_6$) for the preparation of SiC thin films, which is derived by Gordon and coworkers^[11] using effective core potentials and a polarized basis set for geometry optimization. The synthesis of 1,3,5-trisilabenzene was not yet successful and the hunt is still on. Since, compared to the conventionally-

Table 2. Bond dissociation energy of few silanes

Bond	D/kJ mol ⁻¹	Bond	D/kJ mol ⁻¹	Bond	D/kJ mol ⁻¹
H ₃ Si-H	384±2	H ₃ Si-CH ₃	375±5	H ₃ Si- SiH ₃	321±4
MeSiH ₂ -H	388±5	MeSiH ₂ - CH ₃	381±7	H ₃ Si- Si ₂ H ₅	313±8
Me ₂ SiH-H	391±5	Me ₂ SiH- CH ₃	387±7	Me ₃ Si- SiMe ₃	332±12
Me ₃ Si-H	397±2	Me ₃ Si- CH ₃	394±8		

used separate sources for silicon (silanes or chlorosilanes) and carbon (hydrocarbons), alkylsilane molecules are less hazardous and much safer to operate. Meanwhile, SiC communities have been used various alternative vapor sources, including monomethylsilane (CH₃SiH₃), dimethylsilane [(CH₃)₂SiH₂], trimethylsilane [(CH₃)₃SiH], tetramethylsilane [(CH₃)₄Si], tripropylsilane [(C₃H₇)₃SiH], hexamethyldisilane [(CH₃)₆Si₂], dimethylisopropylsilane [(CH₃)₂CHSiH(CH₃)₂], 1,2-bis(dimethylsilyl)ethane, H₃SiCH₂CH₂SiH₃, 1,3-disilabutane (CH₃SiCH₂SiH₂CH₃), and silacyclobutane (c-CH₆SiH₂) to demonstrate pure SiC formation by CVD. A prior knowledge of chemical bond dissociation energies has always been seen as central to the understanding of gas phase process in CVD method. It is worth emphasizing the bond-dissociation values of the few organosilanes (Table 2).

Various research groups have also developed high quality β -SiC using halogen-assisted or halogen-free vapor phase as the source gas on different substrate materials. The gas phase thermodynamics and kinetics of few selected precursors and deposits are described elsewhere. However, the research is open for the reaction mechanism of halogen-free vapor sources and relevant transport properties. The relevant properties of the polytype, including CVD-grown β -SiC, are reviewed elsewhere and confirmed that CVD-grown β -SiC is a better candidate than SiC derived from other techniques [12-14]. When considering nuclear applications based on the strength of the SiC, it is important to differentiate between stoichiometric and non-stoichiometric ceramics.

The SiC CVD from halogen-free monomer sources (let us say methylsilane) offers a number of advantages over other techniques using halogenated organosilane compound (primarily MTS) or mixture of silane with hydrocarbons. For example, SiC CVD from methylsilane is a safe and environmentally appropriate process, since it involves no aggressive chlorine-containing compounds (CH₃SiCl₃, HCl); besides, methylsilane does not self-ignite in air in contrast to silane and does not disproportionate during long-term storage unlike polysilanes (let us say Starfire CVD-4000). In addition, the derivatives of 1,3-

disilabutane has been shown to produce stoichiometric SiC in an inert atmosphere of argon at a relatively low deposition temperature. The correct SiC stoichiometry is designed into the four-membered - (SiC)₂- ring structure, which contains a considerable amount of ring-strain and aids in obtaining a relatively low decomposition temperature. Upon decomposition, this ring opens with the possible formation of reactive species, where both the silicon and carbon can serve as reactive atomic centers. This assists in the incorporation of both the silicon and carbon into the growing film, thereby utilizing more effectively both the Si and C of the disilacyclobutane ring.

Among the range of alkylsilane compounds, including methylsilanes, hexamethyldisilane (HMDS), and silacyclobutane (SCB), that has been utilized for SiC film deposition, HMDS contains a weak Si-Si linkage, and therefore, it should be more susceptible to decomposition and film deposition relative to monosilicon based precursors. Development of SiC thin films from HMDS has been reported using plasma-enhanced CVD (PECVD), low pressure CVD (LPCVD) and laser CVD (LCVD). There have been many studies on the decomposition pathways in the pyrolysis and photolysis of HMDS. The rupture of Si-Si bond has been shown to be the main initial decomposition step in both processes. The existences of a weak Si-Si bond in HMDS, indicating that the more Si-Si bond connections in the gas-phase reaction products than other alkylsilane. This suggests a more active involvement of the reactive silane intermediates in the gas-phase chemistry when using HMDS as source. The aforementioned alternative CVD process for depositing SiC is under consideration, operating at both atmospheric and sub-atmospheric pressure.

Silicon carbide coating on Graphite Rod

HMDS as a single source: Thermal Stability

Prior to deposition, the thermogravimetric (TG) analyses of HMDS were carried out in nitrogen atmosphere at heating rates of 0.17 K s⁻¹ (Fig. 4a) and 0.03 K s⁻¹ (Fig. 4b). Both the TG curves inferred that the chosen precursor is ideal for the deposition of SiC films on

various substrate materials using the CVD technique. Interestingly, complete evaporation of the precursor at very low temperature (< 340 K) revealed that the precursor need not be heated or need very low temperature (~ 323 K) on the precursor port in the CVD system.

Atmospheric pressure *i*-CVD process: SiC deposition and Characterization

Silicon carbide thin film was deposited in a house-built induction assisted CVD set-up (Fig. 5). In this procedure, the vapor of HMDS was used as the exclusive source of SiC. The substrate material of graphite tube was loaded through a detachable top of indigenously designed vertical graphite reactor. The reactor was purged with Ar (by-pass) at the start and at the end of the process, in order to maintain the system in an inert atmosphere. Prior to the deposition, the graphite tube was heated at a temperature of 1150 - 1200°C by an induction coil exactly adjacent to the exterior of the reactor wall.

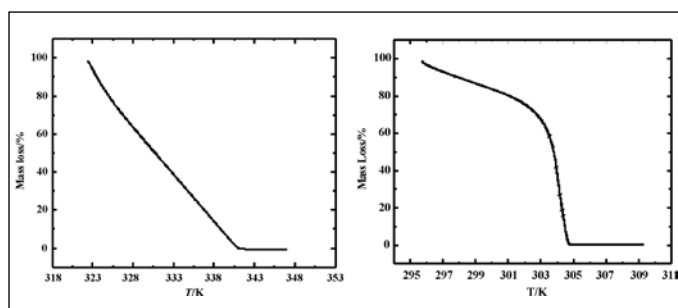


Fig. 4a. TG curve of HMDS in nitrogen atmosphere (0.17 K s^{-1}) Fig. 4b. TG curve of HMDS in nitrogen atmosphere (0.03 K s^{-1})

The induction coil will be driven by a generator to emit a high frequency alternating current such that only the substrate to be coated will be heated. In order to introduce vapor source into a CVD reaction chamber, the HMDS was charged in a bubbler. The carrier gas (Ar) bubbles ascend through the HMDS while allowing the precursor to be vaporized into and become mixed with the carrier gas. The material gas, thus obtained was introduced into the reaction chamber with the carrier gas, when the temperature sufficient to decompose the precursor and deposit the desired SiC on the substrate. The CVD chamber was then cooled to atmosphere to avoid further transport of vapor into the deposition zone. When the chamber temperature reached below 50°C , the Ar flow and the substrate heater were switched off. The coated material was discharged when they completely cooled to room temperature. The phase purity and surface or cross-sectional morphology of the deposits was appraised using XRD and SEM techniques.

X-ray Diffraction and SEM of coated sample

The orientations and degrees of crystallinity in the SiC film were analyzed by XRD. The deposited ~ 150 micron SiC films on graphite rod, with (111) face growth having the most intense reflection at 36.3° (Fig. 6). The average crystallite size was evaluated using Scherer's equation and was found to be ~ 1 nm. The value of the grain size suggested that the coating is composed of nanocrystalline SiC.

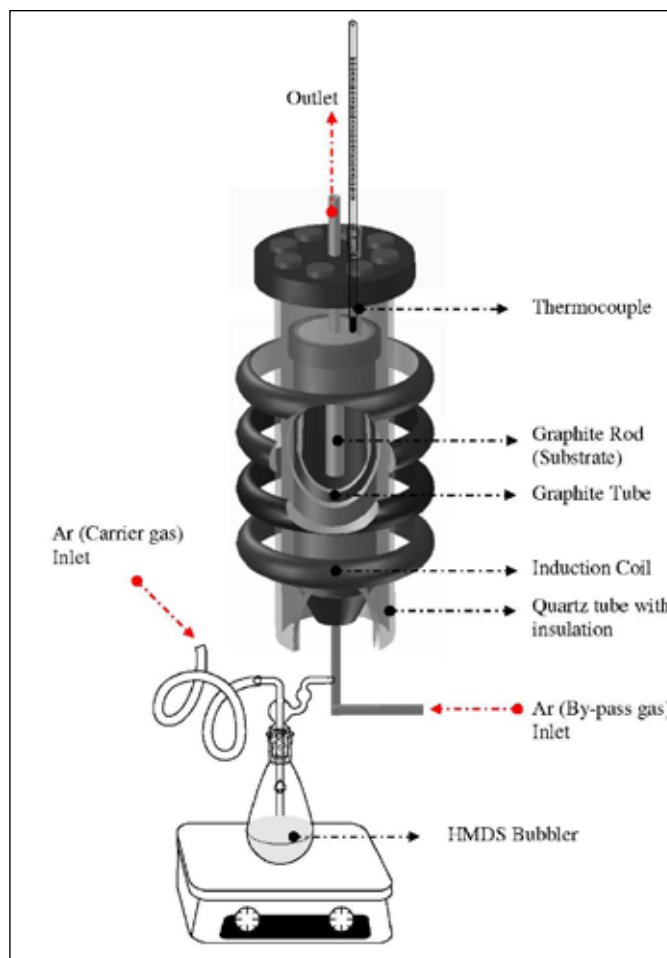


Fig. 5 CVD experimental set-up

The surface morphology of the as-deposited SiC film on graphite rod was analyzed by scanning electron microscopy (SEM). Cross-sectional SEM analysis (Fig. 7a-d) of the SiC-coated graphite rod reveals that the deposits are thick, dense and are in regions of columnar and smooth deposition. The surface morphology (Fig. 7e-h) of the deposited film exhibits growth with good uniformity and a better thickness with the growth rate. The adhesion on the surface was strong, as no detachment of the film was visible after the coating. Nevertheless, later on the SEM images Fig. 7 d and g, one can undervalue the quality of the coatings due to its microcracks.

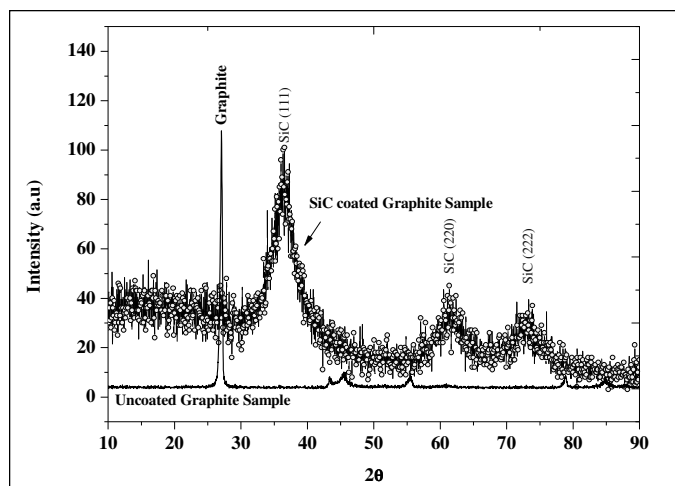


Fig. 6 X-ray diffraction pattern of as deposited SiC on Graphite at 1150°C

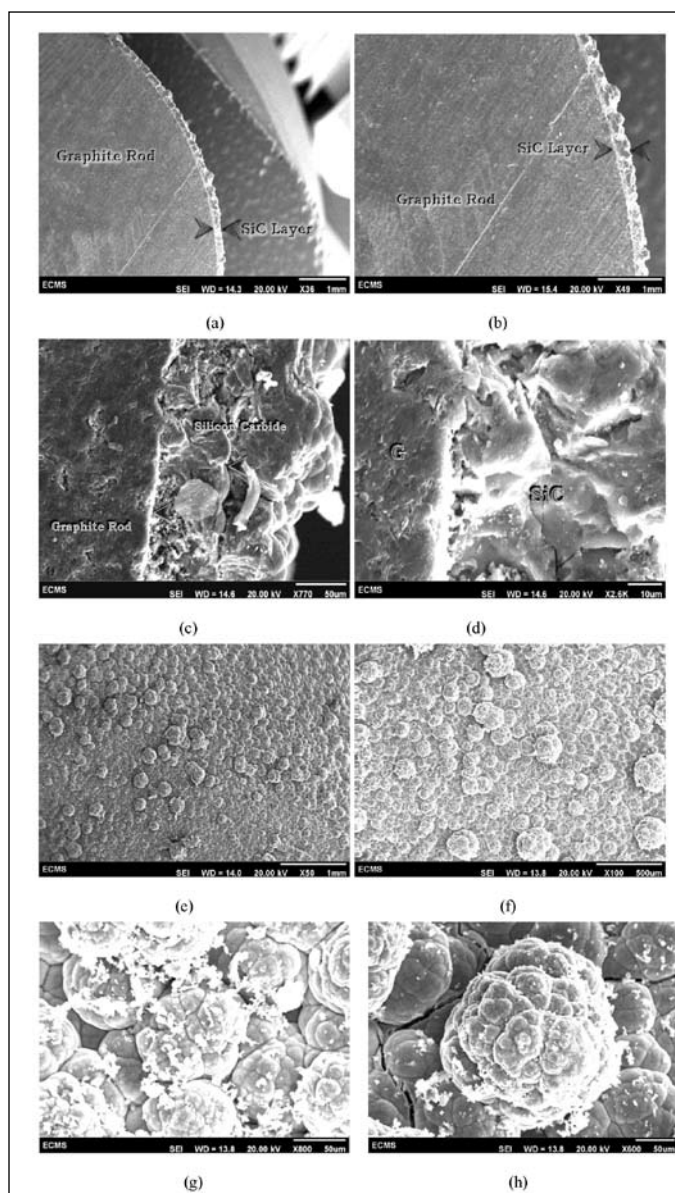


Fig. 7 SEM images of deposited SiC on Graphite rod at 1150°C

Discussion and Recommendations

The deposition of SiC was successfully demonstrated using halogen-free single source precursors. Leave out the presence of micro-cracks, the film morphology revealed that the deposited thin films over graphite substrates show compact structure free from pores, uniformity, and a better thickness with a satisfactory growth rate. More interestingly, the HMDS yielded coatings are relatively good quality film as MTS does. However, the properties and functions of the layer from halogen-free sources need further investigation before being recommended for use.

The similar microstructure was observed by Lloyd and Howard [15], while fabricating large-diameter tubes and coatings in pyrolytic SiC. The SiC was deposited by the thermal breakdown of MTS at 1400°C using RF induction. It was pointed out that, due to cooling of the deposition temperature, large stresses arose in the coatings which often cracked when the restraint of the substrate was removed. These tensions might be caused partly from the conflict in the thermal expansion differences between various SiC stoichiometries occurring in the bands with excess carbon materials. Since in the present study, we developed polycrystalline cubic SiC (due to the presence of (220) face in XRD). Microcrack free thick SiC films will be produced by coating a thin layer of carbon (PyC) film on the substrate before SiC deposition and believed that layer of carbon will eliminate the cracks induced by the different expansion coefficients of SiC coating and graphite substrate. The future experiments are carried out by adopting a fluidized bed based CVD process, for better outcome.

SiC: Applications in Future Nuclear Energy Systems

Revolutionary advancements in materials, including lightweight alloys, high-temperature engine materials and advanced composites, have been a critical part of improving the capability, safety and energy efficiency of our future energy systems. Advancing our science and technology, from fundamental breakthroughs in materials and chemistry in improving manufacturing processes, is critical to our energy future and to establishing new businesses that drive economic prosperity. This part of the article provides examples that illustrate how materials research and development, contribute, especially on SiC based materials, for today's energy technologies, especially for nuclear, and the challenges we need to address to meet tomorrow's energy needs.

SiC as TRISO Layer [3]

The three designs of coated fuel particles in chronological order are: (1) laminar, (2) BISO and (3) TRISO. The TRISO

(Tristructural Isotropic) coated fuel particle was created in the UK as part of the DRAGON project. Current high temperature gas reactor designs use tri-isotropic TRISO-coated particles as fuel. The TRISO-coated particle consists of a fuel kernel and coating layers of porous pyrolytic carbon (PyC), inner high-density PyC (IPyC), silicon carbide (SiC) and outer high density PyC (OPyC). The porous buffer layer provides a free volume of gaseous fission products without causing excessive pressure buildup, and isolates the structural coatings from the mechanical interactions caused by kernel swelling that accompanies fission product accumulation. It also protects the structural coatings by stopping fission fragment recoil atoms ejected from the fuel core. The inner dense PyC layer (IPyC) protects the SiC layer by stopping many fission products (i.e. rare earth elements) that might otherwise chemically attack it. It also prevents reaction between the UO_2 kernel and chlorine containing materials released during the deposition of SiC. IPyC undertakes part of the internal pressure produced by CO_2 , CO and gaseous fission products. The silicon carbide layer (SiC) enhances the mechanical stability of the pressure vessel to retain gaseous fission products, and is the major containment barrier for fission products. The outer PyC (OPyC) layer gives the particle a higher temperature capability of preventing the vaporization of the SiC layer. It also protects the SiC from mechanical damage during fuel manufacture and is an extra barrier for gaseous fission products in case of perturbation of the SiC layer. The usage of TRISO fuel has been explored in HTR by virtue of their promising high burn up capability and good neutronic performance. TRISO particles contain the nuclear fuel inside porous pyrolytic carbon (PyC), concerned to as the buffer layer, where the highly radioactive fissile products and actinide waste will be accommodated safely over very long stops. Despite great progress over the years, there are still a few important issues concerning the TRISO layer growth process, which require to be addressed. In order to comply with the environmental concerns, from the selection of precursors for the deposition of each layer and the conversion of CVD byproducts to the usable applications, special care is to be taken. In quest for knowledge, in pursuit of perfection, and for contributing to science and society, the new generation eco-friendly nuclear research must be further supported.

SiC as Fuel Cladding [16]

Based on the evidence from both Fukushima and TMI-2, the key to achieving accident resistance in commercial nuclear fuel is the fuel cladding, which is intended to contain the fuel and the fission products as the first line of defense against the release of fission products to the environment during accidents. In addition,

investigations of the Three Mile Island accident found that a stronger cladding material would have better handled the incident's core-melting conditions, and might have averted some of the problems that arose during shutdown. An improved cladding material could therefore provide better safety margins and reduced maintenance, while also leaving a larger percentage of the uranium fuel to be burned safely – a movement that could cut waste. As long as zircaloy is used as a cladding material, with its inherent poor properties above normal operating temperatures, it will remain to be the base cause of fission product release during loss of coolant or other core overheating accidents. The root cause of the excessive heat and hydrogen release during the accident (at Fukushima: Boiling Water Reactors) is the zircaloy and steam reactions, and hence released about half the heat and hydrogen during the hours following the accidental core uncovering. Silicon carbide (SiC) has emerged as an outstanding candidate to succeed zircaloy; SiC fibers can be wound onto a hollow “monolithic” tube of SiC and cemented in place with an external layer of SiC. This results in a composite tube that is the same size and shape as traditional zircaloy cladding. SiC's working qualities include excellent strength at high temperatures, an order of magnitude less chemical reactivity with water or steam, very low neutron absorption, and resistance to radiation damage. Monolithic silicon carbide has shown excellent mechanical performance in harsh, high temperature environments and too offers excellent radiation resistance. Nevertheless, its inherent brittle nature limits its application. Recently, high purity, high quality SiC fiber-reinforced composites have been developed to address this limitation. On the other hand SiC ceramic matrix composite (CMC) shows little chemical reaction at elevated temperatures compared to zirconium. Even at very high temperatures the major reaction is exchange of carbon for oxygen in the SiC structure. This reaction produces a less reactive silicon dioxide layer. The conductivity of SiC can exceed the value of zirconium before irradiation. Extended irradiation tends to lower the conductivity to a value half to one-third that of zirconium. Material property optimization and design details, final SiC CMC thickness, can help mitigate the penalty created by the reduced thermal conductivity. The ultimate strength of a CMC is made by the SiC fibers which cause a very high modulus. The soft but bonding interface layer between the matrix and fibers allows cracking in the matrix and stress distribution to the included fibers. This attribute allows the CMC to display a more graceful failure and increased apparent ductility compared to a pure ceramic. The hardness of SiC will also reduce susceptibility to fretting failures that currently affect the reliability of

nuclear fuel during operation. The details of SiC CMC fiber orientation, interface layer design and matrix properties affect the final properties of the engineered cladding. In these composites, a silicon carbide matrix is deposited within a preform composed of unidirectional or woven high purity silicon carbide fibers, such as Tyranno-SA fibers (Ube Industries, Ube, Japan) or Hi-Nicalon type S fibers (Nippon Carbon Co., Ltd., Tokyo, Japan). These materials have greatly improved fracture toughness compared to monolithic materials, and thus are now being seriously considered in nuclear applications. Several techniques have been developed to fabricate SiC matrix composite materials, including melt infiltration, polymer infiltration and pyrolysis and chemical vapor infiltration (CVI). Yet, of these approaches, CVI is the most reliable to produce a matrix composed of very high purity, β -phase SiC that is necessary to provide good radiation resistance for nuclear applications.

SiC in Spent Fuel Waste Management [17]

In order to fulfill safety requirements for the biosphere, the multi-barrier concept – technical (glass and metal, mainly steel and cast iron with spherical graphite) and natural (salt, clay or granite) barriers form an integrated whole – plays a vital role. Knowing that metallic canisters will lose their retention capability after a time which is short in comparison to the storage period, redundancy in the multi-barrier concept is lost quite soon. After 500 to 1,000 years the multi-barrier retention system is reduced to one barrier only – the host rock. Since there is no ideal host rock existing due to solubility or water ingress, the elementary safety principles in nuclear technology, redundancy and diversity, are fed up. For the long-term safety analysis an average lifespan of 500 years is currently proposed as a conservative value for the German Pollux container. Thus, a great deal more attention must be yielded to the long-term stability of the technical barrier.

A comparison of the properties of all questionable materials reveals that silicon carbide (SiC) is predestined for applications as inner canister material under extreme weather. The retentiveness of the SiC canister wall is shown in Fig. 8. The encapsulation of nuclear waste – especially of HLW – in solid state sintered SiC (SSiC) is more than just increasing the redundancy of the multiple barrier concept. Moderate wall thicknesses provided long breakthrough times and small source terms already. Additional potting with a special compound result in a further advancing of the canister properties. Thus a new quality of long-term stable immobilization can be accomplished. The available know-how and the technical-technological state-of-the-art meet the prerequisites for the industrial production

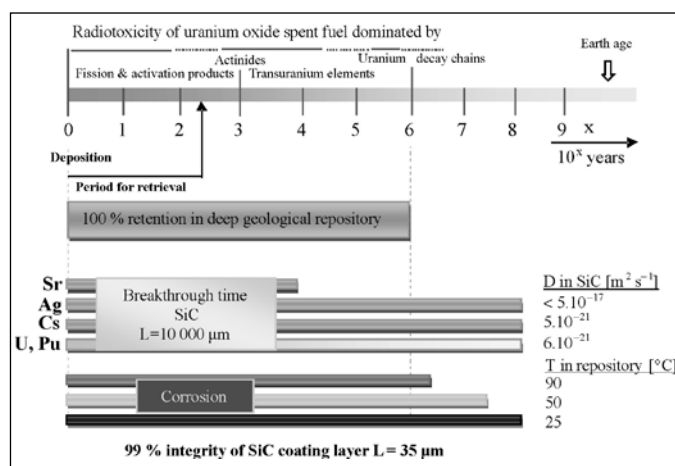


Fig. 8 Retentiveness of the SiC canister wall: diffusion and corrosion

of SSiC canisters for the different HLW types. The SSiC encapsulation as a supplementary retention barrier offers new options for repository sites since the host rock alone cannot assure the safety essentials.

SiC as Neutron Detectors [18]

Silicon carbide neutron detectors are ideally suited for nuclear reactor applications where high-temperature; high-radiation environments are typically run across. Semiconductor detectors such as those based on Si or Ge cannot withstand such high fast neutron fluences and would be unsuitable for this application. Other potential reactor monitoring applications are in-vessel neutron detector, monitoring in proposed advanced power reactors and monitoring of reactors aboard outer space vehicle. SiC detectors have also been used to monitor neutron exposures in Boron-Capture Neutron Therapy as well as the thermal-neutron fluence rates in prompt gamma neutron activation of waste drums. SiC detectors have proven useful for neutron interrogation applications to detect concealed nuclear materials for Homeland Security applications. An application that is particularly well suited for SiC detectors is monitoring of spent nuclear fuel. Spent-fuel environments are characterized by very high gamma-ray intensities of the order of 1,000 Gy/hr and very low neutron fluence rates of the order of hundreds per cm^2 per second. Measurements were conducted out in simulated spent fuel environments, which proved the excellent neutron/gamma discrimination capability of SiC detectors. Long-term monitoring measurements were posted out on spent fuel assemblies over a 2050 hour period, and regardless of the total gamma-ray dosage to the sensing element of over 6000 Gy, the detector successfully monitored both gamma-rays and neutrons with no movement or changes in sensitivity over the entire monitoring period. SiC detectors have been shown to operate well after a cumulative ^{137}Cs

gamma-ray dose of 22.7 MGy. This gamma-ray dose exceeds the full dose that a spent fuel assembly can deliver after discharge from the reactor indicating that cumulative gamma-ray dosage to a SiC detector will never be a factor for spent-fuel monitoring applications. The rapid pace of SiC detector development and the large number of research groups involved worldwide bode well for the future of SiC detector applications.

SiC/SiC Composites in Fusion Reactors [3]

Every bit the key technological challenge to create an attractive and competitive fusion reactor, silicon carbide (SiC) fiber reinforced SiC matrix (SiC/SiC) composites process developments have been extensively examined in these years. One of the important accomplishments is based along the liquid phase sintering (LPS) process modification, where the novel process called Nano-powder Infiltration and Transient Eutectoid (NITE) Process has been modernized. To increase the toughness and reliability, SiC for potential usage in the structural divisions of the first wall blanket in fusion reactors, is reinforced with continuous SiC fibers woven into three-dimensional (3D) fabric. SiC-fiber reinforced SiC composites (SiC_f/SiC) have been introduced since decades for applications in aerospace, advanced friction systems, thermal protection, etc., where the requirements were achieved to a great extent. Thus, the idea to use the same composite as a structural material in fusion reactors was based on expectations that optimization will help to adapt the material's properties to such as required for use in fusion application. All the same, this appeared more difficult as expected, since in comparison to the earlier applications the use of SiC_f/SiC composite as a structural material in fusion application demands for much more stringent set of properties. The main yet unsolved issues remained large and open voids typical for the composites produced by chemical vapor infiltration (CVI) and polymer infiltration and pyrolysis (PIP), and in particular consecutive insufficient thermal conductivity. These properties were therefore placed into focus in many ongoing investigations. The porosity is to the large extent eliminated with the NITE process where, in addition to the pre-ceramic polymer, Al₂O₃ and Y₂O₃ are added as sintering additive. However, the oxide secondary phase limits the thermal conductivity and increases the neutron activation of the material.

Conclusions

The following conclusions can be drawn from this experience:

(i) SiC is a promising candidate material in nuclear reactors to maintain the structural integrity of high temperature




components, includes fuel, cladding, canister for spent fuel, sensors, and so on.

- (ii) Among the polytypes, β -SiC is an ideal candidate for nuclear applications, due to its smaller band gap, high surface area, good stability, Si:C stoichiometry, irradiation stability, and low density.
- (iii) Primary issues on MTS-CVD derived SiC films are the formation of laminated microstructure containing free silicon or porosity, which facilitates/enables permeation by metallic fission products and chemical attack. More significantly, the MTS-CVD gas phase products of chlorine can attack the nuclear fuel kernel and result in uranium dispersion into the surrounding buffer. The main failure mechanism in TRISO-coated particles is a metallic fission product attack on the SiC. In fact, under a thermal gradient, rare earth metals move toward the cold side of the particle, concentrate and degrade the SiC. The traces of chlorine that originate from the MTS act as a path for the penetration of metallic products through the coating. Hence, chlorine-free, nontoxic precursors are to be developed.
- (iv) Reports on the development of nanocrystalline SiC using halogen-free sources by our R&D [19, 20] and from few other research groups in the globe show a fresh path for the parentage of an ecofriendly deposition process as well as to raise the long-term function of the deposit on various applications, particularly in nuclear reactors.
- (v) We successfully demonstrated and developed polycrystalline cubic SiC. Microcrack free thick SiC films will be produced by coating a thin layer of carbon (PyC) film on the substrate before SiC deposition and believed that layer of carbon will eliminate the cracks induced by the different expansion coefficients of SiC coating and graphite substrate. The future experiments are carried out by adopting a fluidized bed based CVD process, for better outcome.
- (vi) However, the understanding of fundamental irradiation effects phenomena, including irradiation creep, various transmutation effects, void swelling, and the underlying physical processes of the ecofriendly CVD-derived deposit is the key to further promoting the science and technology of SiC-based ceramic composites for fusion and advanced nuclear applications. Future SiC-based devices or materials need to be grown using halogen-free solid/liquid sources to avert the low/high temperature corrosion and relevant damages to the materials and to enhance the lifetime of the

materials. In nuclear applications, the scientist should be able to bring forth and make available the properties of down payments for implementation in real-time applications.

References

1. C. J. Rhodes, Science Progress 97 (2014) 72.
2. Y. Katoh and A. Cozzi: Ceramics in Nuclear Applications: Silicon Carbide and Carbon-Based Materials for Nuclear Energy Applications (John Wiley & Sons, Inc., Publication, Vol. 30, Hoboken, NJ, 2010).
3. L. L. Snead, T. Nozawa, Y. Katoh, T-S. Byun, S. Kondo, and D.A. Petti, J. Nucl. Mater. 371 (2007) 329.
4. S. E. Saddow and A. Agarwal, Advances in Silicon Carbide: Processing and Applications. (Artech House, Inc., Norwood, MA, 2004).
5. G.L. Harris, Properties of Silicon Carbide (INSPEC, London, UK, 1995).
6. O. Kordina and S.E. Saddow: Advanced in silicon carbide processing and applications, edited by S.E. Saddow and A. Agarwal. (Artech House, Inc., Norwood, MA, 2004); p. 8.
7. P. Melinon and A. San Miguel, From silicon to carbon clathrates: "Clusters and Fullerenes" The Handbook of Nanophysics (Taylor & Francis, 2010).
8. P. Krishna, R. Marshall, and C.E. Ryan, J. Cryst. Growth, 8 (1971) 129.
9. N. W. Jepps and T.F. Page, J. Micro. 119 (1980) 177.
10. C. W. Whitmarsh and L. V. Interrante, US Patent 5153295 (Oct. 1992).
11. N. Matsunaga and M.S. Gordon, J. Am. Chem. Soc., 116 (1994) 11407.
12. H. T. Chiu and P.F. Wu, J. Chin. Chem. Soc. 38 (1991) 231.
13. J. S. Goela, L.E. Burns, and R.L. Taylor, Appl. Phys. Lett. 64 (1994) 131.
14. R.J. Price, Nucl. Technol. 35 (1977) 320.
15. D.E. Lloyd and V.C. Howard, Special Ceramics, British Ceramics Research Association, 1968, 103.
16. <http://newsoffice.mit.edu/2013/better-cladding-for-nuclear-reactors-0726>.
17. A. Kerber and J. Knorr, atomwirtschaft-atomtechnik (atw) 58. Jg. (2013) Heft 1.
18. H.S. Kim, J.H. Ha, S. Park, S. W. Lee, M. K. Moon, G. Sun and C. H. Lee, J. Nuc. Sci. Technol. 48 (2011) pp 1343-1347.
19. J. Selvakumar and D. Sathiyamoorthy, J. Mater. Research 28 (2013) pp 136-149.
20. J. Selvakumar and D. Sathiyamoorthy, J. Mater. Chem. 22 (2012) pp 7551-7558.

	<p>Dr. J. Selvakumar, Scientific officer at BARCF, Kalpakkam, completed his PhD in chemistry and joined DAE-BARC as Dr. KS Krishnan Research Associate (KSKRA) fellow. His research interests include Chemistry of chemical vapor deposition (CVD) precursors and thin film deposition. He is mainly involved in the development of CVD precursors and processes. His current research activities in BARCF are focused on CVD of mixed metal oxide thin films and their relevant applications. The other research areas and plant works include reprocessing and vetrification of nuclear spent fuel.</p>
	<p>Dr. Krishna Ramadurai, Scientific Officer at BARC, Vashi, Navi Mumbai, received PhD at University of Colorado, Boulder, USA and joined Bhabha Atomic Research Centre. His research interests include carbon materials development and processes. His current research activities in BARC are focused on the development of carbon nano-materials and silicon carbide thin films and their relevant applications.</p>
	<p>Dr. D. Sathiyamoorthy, Outstanding Scientist, Former Head, PMD, BARC, obtained his PhD in Chemical Engineering at IITB, Mumbai and received post-doc at University of Queensland, Australia (Research Fellow), Technical University, Clausthal, Germany (AvH Fellow), and Tokyo University, Japan (JSPS Fellow). Joined BARC at 1974 as Officer Trainee and he is life member of various scientific societies in India. His research interests include fluidization engineering, nanomaterials, particle technology, material processing, extractive metallurgy, fusion reactor materials etc.</p>

Novel Carbon Composites for Nuclear Application

Ramani Venugopalan¹, Kinshuk Dasgupta², Mainak Roy³ and A. K. Tyagi³

¹Powder Metallurgy Division, ²Rare Earths Development Section, Materials Group,

³Chemistry Division, BARC, Mumbai 400 085

E-mail: rvg@barc.gov.in

Abstract

Graphite and carbon-based materials are used in nuclear reactors and continuously there is an upsurge of interest in developing these materials for advanced fission and fusion reactors. Carbon is used as moderator and reflector due to its neutron interaction characteristics, heat transfer properties, corrosion resistance, mechanical strength and stability under irradiation especially at high temperatures. For high temperature reactors, graphite is generally used as moderator. However, for thermal reactors operating at temperature around 200°C, use of graphitic carbon as a moderator involves the risk of sudden release of stored Wigner energy. Carbon black and carbon fiber reinforced composites are new class of novel amorphous materials that aim at reducing the risk of using them in thermal reactors. The present article provides an overview on the different methods of synthesis and characterization of amorphous carbon-carbon composites. The paper also highlights on some of the important thermo mechanical properties of the material and discusses on how they could be improved by different processing/densification methods with suitable reference to the literature.

1. Introduction

Off late there is a tremendous upsurge of interest in exploring carbon and carbon-based materials for nuclear applications. Carbon exists in different allotropic modifications. Each form of carbon has unique properties and hence is of tremendous scientific and technological importance. Graphite is the most abundant crystalline form of carbon and exhibit very high density of 2200 kg/m³. It also possesses tremendous mechanical strength (1.2GPa), even at a high temperature of 1500°C (under inert atmosphere). It is chemically inert, resistant to corrosion and thermal shock [1] and hence finds application as an excellent structural material. In addition to its mechanical properties, exceptional neutronic properties of graphite make it an obvious choice as a moderator material for high temperature nuclear reactors [2]. However, graphitic carbon may not be recommended as a moderator for nuclear reactors operating below 300°C, since there may be accidental release of Wigner energy [3], despite its successful demonstration in Magnox reactors at 150°C. When subjected to irradiation by fast neutrons, carbon atoms in graphite get displaced from its normal lattice positions that results in the accumulation of potential energy in its lattice. Energy as high as 2720J/g may be stored during normal operation of the reactor that may be released accidentally under adiabatic conditions and increase the temperature of graphite to ~1300°C thereby leading to a possible structural burn up. Such a condition is likely to be less probable under high temperature operation at ~1000°C since the radiation induced defects tend to

get annealed at high temperature. Moreover, graphite may undergo post-irradiation densification resulting in changes and thereby causing failure in the fabricated nuclear structures. Irradiation effects on graphitic materials have been discussed at length in the literature [4-6]. To solve this ensuing safety problem regarding the use of graphitic carbon as a moderator for thermal reactors, a new class of carbon is being sought after that would have mechanical properties comparable to that of graphite but at the same time would be amorphous in nature, so that there is minimum accumulation of stored energy. Fibre reinforced carbon-carbon composite is one of the materials of choice. Carbon fiber reinforced carbon matrix composites or briefly termed as carbon-carbon (C/C) composites are synthetically prepared material. Density of these materials varies over a wide range (1600–2000 kg/m³). Their light weight, high mechanical strength even at high temperature (under non-oxidizing atmospheres), high thermal conductivity (greater than Ag and Cu), low coefficient of thermal expansion, high thermal shock resistance make them a true alternative to graphite for moderator applications. Interestingly, mechanical strength of C/C composites increases with temperature, in contrast to that of metals and ceramics. One major drawback of the composites is their low density as compared to graphite which is why composites need to be densified before they could be finally used for nuclear application. Currently, carbon composites are being tested for their prospective nuclear applications. Fig. 1 shows the photograph of a channel tube fabricated with amorphous carbon

composite. Apart from thermal reactors, such carbon-based materials are also being projected for the futuristic high temperature nuclear reactors and fusion reactors. In the following sections, we describe different synthetic routes to producing carbon-carbon composites, principal tools for characterizing them, the densification techniques and some important thermo mechanical properties of the composites.



Fig. 1. Photograph of a channel tube fabricated with carbon-carbon composite

2. Preparation of Carbon-Carbon Composites

Till date, carbon-carbon composites have been prepared using a large number of raw materials such as petroleum coke, phenol formaldehyde resin, polyacrylonitrile (PAN), carbon black etc. A few important processes have been highlighted in this article.

Petroleum coke: Conventionally, petroleum coke is the raw material for preparing carbon-carbon composites. Standard recipes are widely available in the literature [2]. According to one such recipe, phenol formaldehyde binder is mixed with nuclear grade petroleum coke, pelletized and heated in inert atmosphere at $\sim 1000^{\circ}\text{C}$ for obtaining the desired product. Effect of binder on the different physical properties of the composites has been studied extensively [7].

PAN fibers: Non-graphitizing PAN fibers are first chopped, matted and stacked into two dimensional (2D) preforms which are subsequently soaked with phenol formaldehyde resin in different volume fractions. The preforms provide rigidity and also modify other physical properties of the composites. The green preforms are then cut into rectangular pieces of 1' x 1' x 0.4' size and carbonized by slowly heating the preforms at 1000°C , under inert atmosphere and with heating rate of $6^{\circ}\text{C}/\text{h}$. Carbon-carbon composites produced by this technique

are generally highly porous and requires several cycles of densification before desired density of the material is achieved. Further details of sample preparation are discussed elsewhere [7-8].

Carbon black: The first step involves curing of the phenol formaldehyde resin (liquid resol type) at 200°C . The cured resin was then broken into small pieces which were carbonized at 1000°C in inert atmosphere. Quick heating was done at a constant rate of $100^{\circ}\text{C}/\text{h}$ especially in the intermediate temperature range (200°C – 750°C). Subsequently, the carbonized product was powdered yielding fractions of different sized particles having size of less than $75\mu\text{m}$ were sieved off. Metallic impurities were then removed by leaching in hydrochloric acid and the powder was mixed in different proportions with nuclear grade carbon black (N330 grade with surface area $83\text{m}^2/\text{g}$) and phenol formaldehyde as binder. The composite powder was pelletized in a uniaxial press and heated to 1000°C in inert atmosphere. The composites were densified by impregnation technique. A comprehensive treatise on sample preparation is provided in the literature [7]. Carbon black and phenol formaldehyde binder plays a key role in modifying the mechanical and thermal properties of the carbon-carbon composites and will be discussed in the subsequent sections.

3. Thermo Mechanical Properties of Carbon Composites

Effect of fiber-matrix combination: Different relative weight fractions of the carbon fiber have decisive effect on the thermo-mechanical properties of the carbon composites. Typically, 40wt% PAN fiber yields composites with high degree of non-graphitic carbon. It has been found that density of carbon composites increases monotonically with fiber content i.e., decreasing resin matrix element. Higher percentage of fiber improves fiber-matrix binding which decreases open porosity in the samples and results in their improved density. While density of $\sim 900\text{kg}/\text{m}^3$ was achieved with 50% fiber in the matrix. Similarly, compressive strength (CST) increases, while the mean specific heat of the composites decreases with increasing fiber content. Composites produced with the same composition (50% fiber) are found to exhibit CST of $\sim 45\text{MPa}$ [7]. Again, with increasing fiber content, coefficient of thermal expansion parallel to the axis (CTE^{\parallel}) increases consistently and that perpendicular to the axis (CTE^{\perp}) increases first but then decreases.

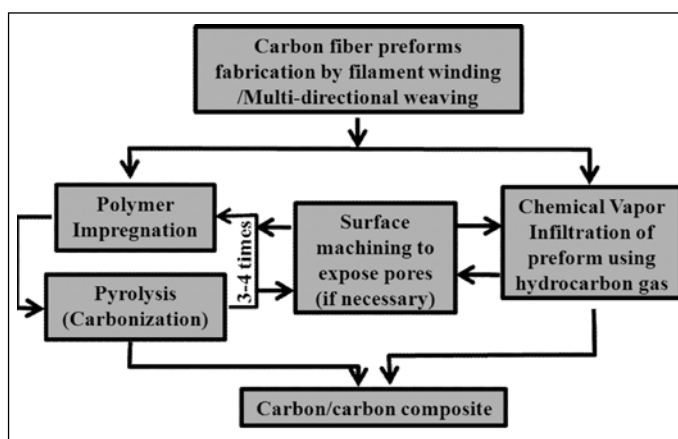
Effect of carbon black and binder: Because of lower porosity, density of carbon-black based composites is usually higher than that of the carbon fiber but lower than that of the petroleum coke based samples. Density

of petroleum coke-based and composite increases initially with binder weight-fraction reaches a maximum of $\sim 1710 \text{ kg/m}^3$ @ 1000°C for 25wt% binder and then decreases steadily. It is believed that the binder initially decreases the inter-particular gap, thereby decreasing the density of the carbon composite. Excess binder, on the other hand, increases porosity due to the volatile residues formed during its carbonization. Density of carbon black based composites does not change systematically with its content in the samples. However, the binder effect on the density of the composites is quite predominant. Similar effect of carbon black and binder is observed for compressive strength of the composites prepared from carbon black. CTE⁺ systematically increases whereas mean specific heat decreases as a function of carbon black content in the composites.

4. Densification by Impregnation Method

Densification of the porous composites may be achieved via two different impregnation routes namely gas phase impregnation and liquid phase impregnation route.

Liquid phase impregnation: It is economically more viable of the two techniques and is commonly used for impregnating carbon composites. The process is carried out in successive cycles for improving density and other mechanical and thermal properties. In this process, the liquid precursor for carbon is forced into the fine pores of the porous composites by applying positive pressure followed by carbonization of the impregnated composites at high temperature under inert atmosphere.



Scheme-I. Schematic representation of the densification process

A typical setup that has been used in our laboratories is shown in Fig. 2. Density of composites increases by almost 20-40% upon several cycles of liquid impregnation. Consequently, open pores in the samples decrease after every cycle. After residual porosity drops down to $\sim 1\%$,

density does not increase appreciably [7]. But during high-temperature processing, there is a possibility that stress may be developed in the samples due to unequal expansion of the core and the matrix and as a result cracks may be formed in the composites.

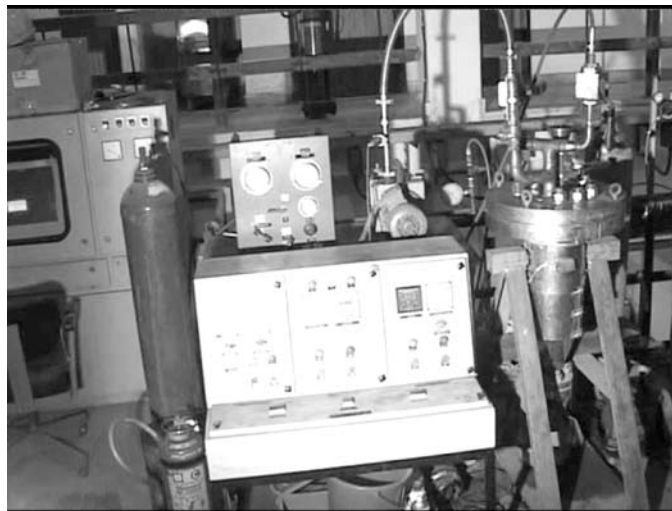


Fig. 2. Laboratory setup for liquid impregnation of carbon-carbon composites

Gas phase impregnation: The vapor phase densification is often used in conjunction with liquid phase impregnation technique. Initially, the composites are impregnated as described in the previous section and then by chemical vapor infiltration technique (CVI) [9]. A vertical tubular reactor typically maintained at 1000°C is used for cracking of the carbon precursor by CVI. Acetylene is used as the common carbon source and nitrogen gas as inert diluent. The cracking temperature is optimized for maximum deposition of the pyrocarbon inside the pores of the composites. Fig. 3 shows a typical setup used for CVI. It has been reported [9] that flow rate and precursor dead time plays an important role in determining the microstructure and density of the composites. The complete process of densification comprising of liquid and vapor phase techniques is schematically represented below (Scheme I).

Effect of impregnation pressure and time: Impregnation pressure is an important parameter that influences the formation of the secondary carbon phases at the interface of fiber and matrix, hence distribution of open pores in the samples and eventually densification of the composites [8]. Pure carbon particles that are formed from the resin get into the pores that transforms into secondary carbon during carbonization. Obviously, at higher pressures (typically 7MPa) extensive pore filling takes place that results in agglomerates with uniform and efficient packing and ultimately composites without any visible void in

them. Even the morphology gets modified with pressure. Whereas at lower pressure (e.g. 3MPa) spherical particles with distinct octahedral voids in between are formed, at higher pressures (5MPa and above) irregular shaped agglomerates are formed along with spherical particles. Formation of secondary phase is more at lower pressures that reduces the number of pores in the composites.



Fig. 3. Setup for chemical vapor infiltration

Fig. 4 shows the scanning electron micrograph of a composite densified by liquid impregnation method. Effect of impregnation pressure and time of impregnation on the nature and distribution of small and large pores as has been extensively investigated using small angle neutron scattering (SANS) and mercury porosimetry [8]. Irrespective of large and small pores, the pore diameter shrinks with increasing pressure of impregnation but neither the pore diameter nor their distribution changes significantly with impregnation time at a moderate pressure

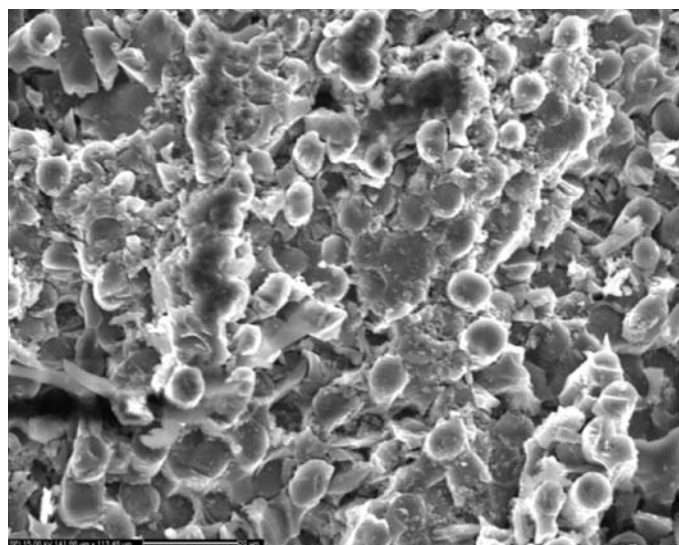


Fig. 4. SEM micrograph of composite after densification by liquid phase impregnation

of 5Mpa. Formation of cracks following high-temperature carbonization process has been studied by X-ray microtomography. The study clearly shows uniformity of contrast at higher impregnation pressure implying that lesser number of cracks is formed at high pressure due to better matrix-resin bonding in the composites.

5. Graphitization and Isotropic Nature

The primary objective behind preparation of carbon-carbon composites for nuclear applications lies in retaining their isotropicity and amorphous nature. Optical polarized microscopy with cross-polarizers and a retarder plate (λ -plate) has been used to investigate the extent of anisotropy in the composites. Due to difference in the phase shift, the anisotropic graphitic crystals appear either greenish blue or deep yellow depending on the orientation of its aromatic planes. The isotropic phase appears blurred magenta under a retarder λ -plate that introduces a shift of 551nm. Appearance of bright green/ yellow coloration in the sample is often termed as optical activity [3-10]. Details of the technique are available in the literature [10]. Fig. 5 shows the polarized optical micrograph of a typical carbon-carbon composite with a degree of anisotropy (yellow patch). It is observed that high-temperature treatment enhances the size of anisotropic graphite crystals and hence extent of activity in the composites. Similar observations were made on PAN fiber based samples from XRD and Raman spectroscopic studies (to be discussed in details subsequently). It has been reported [7] that heat treatment of the composites at $\sim 1800^{\circ}\text{C}$ leads to a change of amorphous carbon content by $\sim 2\%$ and significant short range ordering along the c-axis. Sample density has also changed by 10-17% in this process. PAN

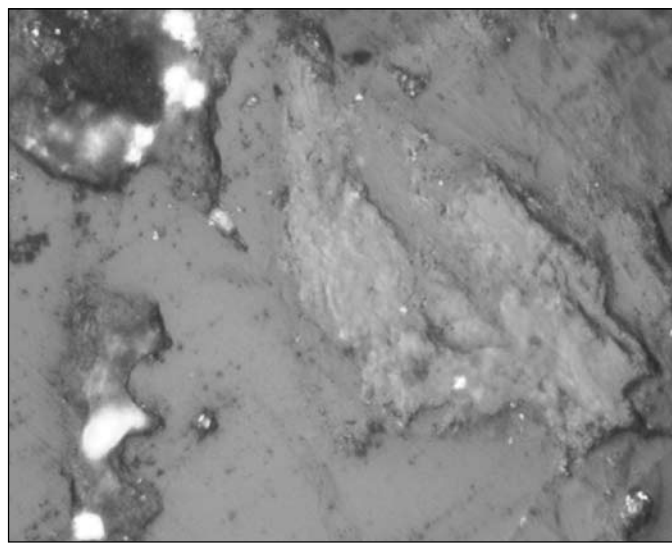


Fig. 5. Optical micrograph of a typical carbon-carbon composite

fiber based samples with higher fiber percentage exhibits higher optical activity. Here, graphitization is induced by the stress developed at the fiber ends. During high temperature treatment, uneven distribution of stress along the length of fiber with maximum stress at the end and minimum at the center [3] due to fiber matrix interaction leads to the development of anisotropic graphite phase in the sample. Carbon black based composites on the other hand, has nearly spherical geometry which relieves the stress. X-ray diffraction is yet another technique that has been employed to approximately evaluate the extent of graphitization in amorphous composites by making use of turbostratic model [11]. XRD patterns of composites exhibit a broad peak at $\sim 27^\circ$ due to reflection from the 002 planes of graphite. Accordingly, % graphitization is given by

$$\% \text{ graphitization} = \{(3.44-d_{002}) / (3.44-3.354)\} * 100 \dots\dots (i)$$

where d_{002} denotes the inter-planar spacing as determined from the peak position using the Bragg's law. The inter-planar spacing for a pure graphite sample is expected to be 3.354Å and that for a completely amorphous sample it is expected to be 3.34Å. A large number of composites have been prepared using different starting materials and with a wide range of compositions [7]. It has been reported that a petroleum coke based sample with 25% binder exhibits 25% graphitization whereas carbon black based composites with 0-15% carbon black content and fiber based samples with 0-50% binder do not exhibit graphitization at all.

Effect of impregnation pressure and time influences the extent of ordering in the composites. It has been observed that d_{002} decreases almost linearly with pressure indicating that there is an increase of ordering in the samples. The ordering is also manifested in the grain growth along c-axis as calculated using the Scherer equation [12-13] as given below

$$L_c = k\lambda / \beta \cos\theta \dots\dots\dots (ii)$$

Where β and θ represents the full width at half maximum (FWHM) and Bragg's angle for the 002 peak respectively. For (002) plane, the constant k is usually taken as 0.89. Again, the effect of impregnation time is not so significant on the formation of anisotropic graphite phase as compared to that of impregnation pressure. Further, amorphous carbon content of the composites may be approximately estimated from the reduced (002) peak intensity using mathematical models given in the literature [14-15]. A recent analysis shows that PAN fiber based samples impregnated at 3-5MPa pressure exhibits very high (over 90%) amorphous carbon content. Raman spectroscopy and X-ray photoelectron spectroscopy (XPS)

are the two techniques that have been used to estimate sp^2 -C/ sp^3 -C ratio and hence the extent of graphitization. Raman spectra of amorphous carbon exhibits two peaks, one at $\sim 1350\text{cm}^{-1}$ and the other at $\sim 1580\text{cm}^{-1}$ respectively called the D-band and the G-band. Intensity ratio of D-band to G-band (D/G ratio) denotes the extent of disorder and hence amorphization in the samples [8]. It is observed from Raman spectroscopy and XPS studies that impregnation pressure for densification process and also the time of impregnation influence the long range ordering in the composites. D/G ratio initially decreases with the time of impregnation and then tends to remain constant with time. The initial decrease of the D/G ratio is more prominent at higher pressures. At higher pressures, local clustering of sp^2 bonded carbon atoms at open pores is more due to the generated stress and hence the steep decline in D/G ratio. Similarly, C1s XPS spectra exhibits two principal peak at $\sim 284.3\text{eV}$ and 285eV respectively attributed to the sp^2 and sp^3 bonded carbon atoms. Therefore, ratio of the two peaks represents the sp^2/sp^3 carbon fraction in the samples. It has been observed that the ratio is higher for samples impregnated at higher pressures corroborating the previous observation from Raman spectroscopy.

6. Irradiation Studies

Research on the development of carbon-carbon composites developed using polyacrylonitrile (PAN) and their irradiation stability studies are scanty. Ramani *et al.* [16] in their investigations, carried out neutron irradiation of the carbon fiber reinforced composite. These samples were irradiated in a flux of 10^{12} n/cm²/s at temperature of 40 °C. The fluence was 2.52×10^{16} n/cm². These samples have been characterized by XRD and Raman spectroscopy before and after neutron irradiation. From the XRD analysis of the irradiated and unirradiated samples it is found that the values of d_{002} peaks for the unirradiated samples are higher than that of the irradiated samples indicating the tendency to get ordered structure which was also inferred from the Raman spectroscopy. The stored energy was found to be 82 J/g at fluence of 2.52×10^{16} n/cm² and 185J/g for a fluence of 7.2×10^{16} n/cm².





7. Summary

Carbon-carbon composites have come up as a new class of nuclear materials that possess very high mechanical strength, good thermal conductivity and reasonably high density. The advantage of carbon-carbon composite is that the microstructure and the properties can be tailor made by controlling the volume fraction of carbon fibre and changing the heat-treatment temperature. Therefore, they can be used in low temperature reactors where disordered structure is required and also in high temperature reactors

where graphitic structure is required. A review of the principal thermo-physical properties of carbon-carbon composites clearly shows that the material is versatile to be used as a moderator material for current as well as futuristic reactors.

References

1. Kelly. B. T, Burchell. T. D., Carbon 32, (1994) 499.
2. Nuclear Graphite; Academic Press: New York and London, 1962.
3. Oberlin A, B. S, Lafdi K. In Carbon Fibers; Donnet J. B, W. T. K., Rebonillat S, Peng J. C. M., Ed.; Dekker: New York, 1998, p 85.
4. Simmons. J. W. S. Radiation Damage in Graphite; Pergamon Press, 1965.
5. Burchell. T. D, Fission Reactor Applications of Carbon; Elsevier Science 1999.
6. Burchell. T. D, MRS Bulletin 1997, XXII 29.
7. Dasgupta. K, Roy. M, Tyagi. A. K, Kulshreshtha. S. K, Venugopalan. R, Sathiyamoorthy. D, Composites Science and Technology 67(2007)1794.
8. Venugopalan. R, Roy. M, Thomas. S, Patra. A. K, Sathiyamoorthy. D, Tyagi. A. K, Journal of Nuclear Materials 433(2013)494.
9. Dasgupta. K, Prakash. J, Tripathi. B. M, Journal of Nuclear Materials 445 (2014) 72.
10. Dasgupta. K, Sathiyamoorthy. D, Materials Science and Technology 19(2003) 995.
11. Pacault A. In: Walker Jr PL, editor. Chem. Phys. Carbon, Vol. 7. New York: Marcel Dekker; 1971. p. 107-54.
12. Scherrer. P. Nachr. Ges. Wiss Gottingen, 2 (1918)98.
13. Cullity. B. D. Elements of X-ray diffraction; Addison-Wesley, 1978.
14. Franklin. R. Acta Crystallographica, 3(1950)107.
15. Sarkar. A. Dasgupta. K, Barat. P, Mukherjee. P, Sathiyamoorthy. D, International Journal of Modern Physics B 22(2008)865.
16. Venugopalan. R, Sathiyamoorthy. D, Acharya. R, Tyagi. A. K, Journal of Nuclear Materials 404(2010)19.

	<p>Dr. (Smt.) Ramani Venugopalan did her graduation and post graduation in Chemistry from University of Bombay. Subsequently she joined Bhabha Atomic Research Centre and is presently working in Powder Metallurgy Division, Bhabha Atomic Research. She completed her PhD from Homi Bhabha National Institute (Deemed to be University), Mumbai, India in 2011. She has worked in the field of extractive metallurgy and process metallurgy of rare and refractory metals. She is working presently on the development of advanced carbon materials especially on carbon-carbon composite and on the TRISO particle development for upcoming CHTR.</p>
	<p>Dr. Kinshuk Dasgupta is from 43rd batch of BARC Training School and joined Materials Group of BARC in 2000. Since then he has been working in the field of carbon based materials including carbon-carbon composite and carbon nanomaterials. He has made significant contributions towards synthesis and characterization of composites as well as carbon nanotubes (CNTs) by catalytic chemical vapour deposition (CCVD) method, for which he was awarded Young Metallurgist of the Year 2007 by Ministry of Steel and Young Engineer 2011 by Department of Atomic Energy.</p>
	<p>Dr. M. Roy joined Chemistry Division in 1999 from the 42nd batch of BARC-Training School. He completed his PhD from the Mumbai University in 2005. His fields of interest are nanoparticles, carbon composites, surface enhanced resonance Raman spectroscopy and Raman studies of carbon allotropes. Dr. Roy worked as a visiting scientist at the Technische University, Chemnitz, Germany. He has also worked as a post-doctoral researcher in Max-Planck Institute for Polymer Research, Mainz, Germany. He has authored 50 scientific articles in national and international journals. He has also authored two book chapters and edited one book.</p>
	<p>Dr. A. K. Tyagi is presently heading the Solid State Chemistry Section of Chemistry Division, BARC and is also a Professor of Chemistry at HBNI. His research interests are in the field of nanomaterials, functional materials and nuclear materials. He has been conferred with several awards such as ISCAS-Dr. Laxmi Award; Rheometric-ITAS Award; MRSI Medal; CRSI, Medal; Gold Medal of Indian Nuclear Society; DAE-Homi Bhabha Science and Technology Award, IANCAS-Dr Tarun Datta Memorial Award; ICS-R.D. Desai Memorial Award; Rajib Goyal Prize in Chemical Sciences; DAE-SRC Outstanding Research Investigator Award; CRSI-Prof. CNR Rao National Prize for Chemical Sciences; ISCB Excellence Award in Chemical Sciences, DAE-Group Achievement Award; and MRSI-ICSC Materials Science Senior Award. He is a Fellow of the Maharashtra Academy of Sciences; Royal Society of Chemistry (FRSC); National Academy of Sciences, India (FNASc); Indian Academy of Sciences (FASc); and Asia Pacific Academy of Materials (FAPAM).</p>

Structures and energetics of alkali and alkaline earth metal ion complexes of sumanene and corannulene: A systematic understanding of cation- π interactions

Chinagandham Rajesh¹, Chiranjib Majumder²

¹RMC, ²Chemistry Division, BARC, Mumbai, India

E-mail: chimaju@barc.gov.in

Abstract

Using *state of the art* density functional theory we report the equilibrium geometries and electronic properties of M-Sumanene/Corannulene (M = Li⁺, Na⁺, K⁺, Be²⁺, Mg²⁺, Ca²⁺) complexes. The results show that the bowl-depth or curvature of the Sumanene/Corannulene molecules and the size of the metal ion play very crucial role to decide the favored binding site. The binding energy between the metal ions and the π -conjugated molecules is found to follow the trend Be²⁺ > Mg²⁺ > Ca²⁺ > Li⁺ > Na⁺ > K⁺. A good correlation between the polarizability of the metal ion and the binding energy was observed, with the highly polarizing metal ions binding the π -system strongly. It is further observed that the binding strength of the M⁺-sumanene complexes is weaker as compared to the corannulene, implying that the cations bind more strongly on flat surfaces. The bowl-to-bowl inversion barriers of the Sumanene/Corannulene molecules and their corresponding cation-complexes have been evaluated. It is found that the metal ion complexation to the bowl molecules results in increasing the inversion barrier. Energy decomposition analysis suggests that the orbital interactions is larger in magnitude than the electrostatic component and is ultimately responsible for the overall stabilization of the pre-relaxed fragment interactions. The Mulliken charge analysis of various complexes suggests that the strength of the interaction is linearly proportional to the amount of charge transfer from the π -system to the M⁺ ion.

1. Introduction

Cation- π interactions play an important role in molecular recognition [1]. These interactions are important to understand various systems like (1) protein structure [2], (2) substrate-enzyme binding [3], (3) catalytic processes [4], and (4) in host-guest complexes [5]. In the coordination chemistry of fullerene fragments, called bucky-bowls, the smallest C_{5v} and C_{3v} symmetrical subunits of the C₆₀-fullerene, namely corannulene (C₂₀H₁₀) and sumanene (C₂₁H₁₂) have served as the primary models for theoretical and experimental coordination studies and one of the intriguing issues is the preference for metal binding to the convex surface versus the concave one.

Convex binding, including η^1 , η^2 , and η^6 -coordination modes, were found in the X-ray crystal structures of some mono-metalated corannulene complexes. Sieders *et al* reported and established spectroscopically, the first transition metal complex of corannulene [Cp*₂Ru(η^6 -C₂₀H₁₀)](O₃SCF₃), in which Cp* is η^5 -C₅Me₅, where η^6 -coordination of a metal atom to a curved poly-nuclear aromatic hydrocarbon (PAH) surface was found [6]. X-ray structural characterization of the above complex which was subsequently established by Vechhi *et al* [7], unveiled the effect that transition metals can show on bowl-shaped

poly-aromatic ligands. Buckybowl complexes of Iridium have been synthesized and characterized by Alvarez [8]. Subsequent studies resulted in the increase of these classes of compounds [9]. The first η^2 -coordinated transition metal complexes of corannulene were reported by Petrukhina *et al* [10]. Further complexes of rhodium (II) and ruthenium (I) having isolated and 1D and 2D structures with various binding modes including terminal η^2 , and bridging μ^2 - η^2 : η^2 and μ^3 - η^2 : η^2 : η^2 coordination to the rim, have been synthesized and characterized [11]. Caraiman and co-workers [12] have investigated the gas-phase reactivity of C₆₀Fe⁺ and C₂₀H₁₀Fe⁺ using the selected-ion flow tube technique. The first hub-bound corannulene complex where Ruthenium (I) center is η^1 coordinated to a single interior carbon atom on the convex surface of C₂₀H₁₀ was synthesized by consciously softening the electrophilic properties of the metal [13]. The above observations have established the general preference of the single metal atom complexation to the convex face of the corannulene and diminished the hope of using buckybowl to access inclusion metal complexes. Accordingly, except in *ab initio* studies on the binding of alkali-metal cations and Ga⁺ to hemifullerene [14], a concave-selective coordination complex has never been isolated or predicted by molecular calculations.

Various coordination modes, including η^1 , η^2 , η^4 , η^5 , and η^6 , are conceivable with sumanene. However, very little has been done to explore the coordination chemistry of this class of molecules except for a computational study that predicts convex binding of $\{\text{Pt}(\text{PH}_3)_2\}$ in an η^2 fashion has been done by Kamenko *et al* [15]. In this background, Ameya *et al* [16] have reported the first synthesis of the concave-binding complex of sumanene with $\{\text{CpFe}\}^+$ ($\text{Cp}=\text{C}_5\text{H}_5$). Encouraged by these results, Sakane *et al* [17] have successfully synthesized and characterized two monoalkyl-substituted $[\text{CpFe}(\eta^6\text{-sumanene})]^+$ which exhibited concave-face selective coordination. Further it was the first chiral π -bowl complex to be reported. A study on the dynamic bowl-to-bowl inversion behavior of $[\text{CpRu}(\eta^6\text{-sumanene})]\text{PF}_6$ has shown that it is a thermodynamically controlled process rather than being kinetically controlled [18]. These works have several important implications including the fact that concave carbon faces can also be engaged in metal binding.

Substantial efforts have been put in studying the reactivity and binding properties of buckybowls using various computational techniques to compensate for the restricted number of their metal complexes that have been synthesized and structurally characterized by single crystal X-ray diffraction. From the theoretical studies on the electrostatic potential on the surface of the curved aromatic hydrocarbons, it has been envisaged that these molecules would be polarized because of the unsymmetrical nature of their π orbitals [19]. According to Klarner *et al*, cation- π complexation should be favored inside the bowl rather than outside since the concave surface shows the more negative electrostatic potential [20]. The computational studies on $(\eta^6\text{-corannulene})\text{Ru}(\text{C}_5\text{H}_5)^+$ complexes predict exo-binding preference of the Ru-ligand over endo binding. Modeling studies of the complexes of Li^+ with corannulene have shown preferential complexation on the six-member ring over the five-member ring and convex face over the concave face binding [21]. Dunbar [22] has carried out calculations on the binding of a few alkali (Li^+ , Na^+ , and K^+) and transition-metal (Ti^+ , Cr^+ , Ni^+ , and Cu^+) ions to corannulene and coronene. Density functional theory calculations performed on the Li^+ and Na^+ π -complexes of native and heteroatom substituted analogues of corannulene/sumanene showed a consistent metal preference towards the convex surface [23]. Kandalam *et al* have shown that the on-top site of the six-member ring (η^6) of corannulene molecule is the most preferred binding site for both Fe atom and Fe^+ ions [24].

Though, there has been a surge in the experimental front to synthesize and characterize the transition metal-bucky bowl complexes, studies on alkali and alkaline

earth metal complexes with these extended curved π systems is in scarce. In this work we have carried out a theoretical investigation to study the cation- π interactions of corannulene and sumanene molecules with alkali (Li^+ , Na^+ and K^+) and alkaline earth (Be^{2+} , Mg^{2+} , Ca^{2+}) metal ions. In particular, our results on M-Sumanene/Corannulene complexes focus on the ground state geometries, electronic structures, binding energy and the charge transfer from/to the metal ions. The structural preference of different metal ions to adsorb on the bowls along with the trends in the binding energy has been analyzed systematically. Elucidation of structural and electronic properties influencing the binding energy and bowl depth has been carried out. Bond decomposition and charge transfer analysis have been carried out to underscore the bonding contributions from various sources and to understand the origin of stabilizing and destabilizing interactions.

2. Computational methods

All calculations reported in this article were performed using Density Functional Theory as implemented in Amsterdam Density Functional (ADF 2004) program [25]. A generalized-gradient-approximation (GGA) functional consisting the exchange expression proposed by Becke and the correlation expression proposed by Lee, Yang and Parr, were utilized [26]. Uncontracted Slater-type orbitals (STOs) were used as basis functions for the total energy calculations [27]. Triple- ζ -basis sets augmented by one and two sets of polarization functions were used separately to undermine the basis set effects of TZP and TZ2P respectively. In order to realize the most preferred site of adsorption, the dopant alkali and alkaline earth metal ions are allowed to adsorb at several sites with different types of coordination. In the case of corannulene the dopants are allowed to interact on the convex and concave faces which included the η^5 and η^6 co-ordinated sites on the five and the six member rings respectively. In case of sumanene, η^6 co-ordinated sites over the six member rings and η^4 coordination over the five membered rings were considered. No local minima on the bridge site (η^2) were observed with the initial structures collapsing to one of the higher coordinated geometries. To verify the stability of the optimized structures on the potential energy surface, we calculated the vibrational frequencies at the stationary points. The nature of the bonding between the metal and bowl fragments has been analyzed by means of the energy decomposition analysis (EDA) implemented in the ADF code, which is based on the EDA method of Morokuma [28] and the extended transition state (ETS) partitioning scheme developed by Ziegler and Rauk [29].

3. Results and Discussion

3.1 Equilibrium Geometries

Initial calculations were carried out on bare corannulene and sumanene molecules. The bowl-depth of corannulene and sumanene are found to be 0.83 Å and 1.08 Å respectively, which are consistent with the previously

obtained results [23]. These results reflect that corannulene is more planar than sumanene. In order to identify the most preferred site of adsorption, the dopant alkali and alkaline earth metal ions are allowed to adsorb on the convex and the concave faces at several sites. Two types of competitions (i) face: convex vs concave (ii) co-ordination preference (among $\eta^2:\eta^4$ $\eta^5:\eta^6$) seems to direct the site preference.

Table 1: This table summarizes the binding energy (BE is in Kcal/mol using TZP and TZ2P basis sets) of the metal-corannulene/sumanene complexes along with the optimized geometrical parameters (R_1 and R_2) and charges on the metal ions. While R_1 represents the vertical distance of the metal ions from the central ring, R_2 gives the average distance between the metal ion and the atoms of the central ring of the respective metal (M^+/M^{2+}) bound corannulene and sumanene complexes.

System		Corannulene					Sumanene				
		BE (TZP)	BE (TZ2P)	R_1	R_2	Charge	BE (TZP)	BE (TZ2P)	R_1	R_2	Charge
Li ⁺	Convex	-1.89	1.89	1.93	2.21	0.63	1.66	1.64	1.79	2.28	0.69
	Concave	-1.63	1.60	1.95	2.30	0.74	1.64	1.63	1.82	2.31	0.79
Na ⁺	Convex	-1.27	1.26	2.42	2.71	0.77	1.09	1.06	2.40	2.79	0.74
	Concave	-1.05	1.04	2.50	2.77	0.86	1.23	1.22	2.34	2.74	0.83
K ⁺	Convex	-0.91	0.90	2.84	3.09	0.89	0.78	0.77	2.82	3.16	0.89
	Concave	-0.78	0.77	2.90	3.14	0.92	0.88	0.88	2.80	3.14	0.92
Be ⁺²	Convex	-12.08	12.10	1.31	1.78	0.67	11.68	11.77	1.24	1.84	0.63
	Concave	-11.74	11.70	1.39	1.84	0.69	11.61	11.65	1.34	1.89	0.64
Mg ⁺²	Convex	-6.93	6.47	1.92	2.27	1.16	6.88	6.42	1.81	2.31	1.10
	Concave	-6.16	6.18	1.93	2.29	1.24	6.86	6.12	1.83	2.32	1.19
Ca ⁺²	Convex	-5.15	5.20	2.25	2.56	1.11	5.23	5.29	2.16	2.59	1.06
	Concave	-5.04	4.88	2.30	2.60	1.34	5.09	5.16	2.21	2.63	1.31

Table 2: Decomposition of the bonding energy (eV) for the metal ion-corannulene/sumanene complexes

System	Sumanene			Corannulene		
	Pauli Repulsion (eV)	Electro-Static (eV)	Orbital (eV)	Pauli Repulsion (eV)	Electro-Static (eV)	Orbital (eV)
Convex						
Li ⁺	0.25	-0.21	-1.72	0.4	-0.32	-1.97
Na ⁺	0.31	-0.38	-1.17	0.32	-0.45	-1.13
K ⁺	0.37	-0.42	-0.84	0.4	-0.46	-0.84
Be ⁺²	1.49	-0.37	-12.92	1.73	-0.45	-13.52
Mg ⁺²	1.19	-0.56	-7.60	1.26	-0.84	-7.45
Ca ⁺²	1.69	-0.93	-5.97	1.72	-1.09	-5.85
Concave						
Li ⁺	0.42	-0.11	-1.96	0.37	-0.10	-1.89
Na ⁺	0.26	-0.04	-1.30	0.23	-0.16	-1.12
K ⁺	0.38	-0.11	-1.04	0.34	-0.14	-0.97
Be ⁺²	2.15	-0.33	-13.65	2.23	-0.27	-13.79
Mg ⁺²	1.33	-0.24	-7.75	1.31	-0.18	-7.37
Ca ⁺²	2.03	-0.30	-7.12	1.93	-0.28	-6.50

Table 3. The bowl-to-bowl inversion barriers (in kcal/mol) of the corannulene/sumanene and their metal ion complexes obtained at the BLYP level using TZ2P basis. The numbers in the bracket indicate the number of imaginary frequencies.

System	Corannulene					Sumanene				
	Concave		TS	Convex		Concave		TS	Convex	
	ΔE	BD	ΔE	ΔE	BD	ΔE	BD	ΔE	ΔE	BD
--	0.0	0.83	0.436 (1)	0.0	0.83	0.0	1.08	0.62 (1)	0.0	1.08
Li ⁺	0.284	0.85	0.56 (1)	0.0	0.89	0.01	1.15	0.82 (1)	0.0	1.112
Na ⁺	0.221	0.85	0.58 (1)	0.0	0.90	0.16	1.18	0.84 (1)	0.0	1.136
K ⁺	0.13	0.92	0.633 (1)	0.0	0.98	0.11	1.21	0.86 (1)	0.0	1.150
Be ²⁺	0.395	0.88	0.478 (1)	0.0	0.91	0.0	1.15	0.69 (1)	0.118	1.016
Mg ²⁺	0.29	0.93	0.55 (1)	0.0	0.98	0.0	1.213	0.88 (1)	0.30	1.121
Ca ²⁺	0.38	0.99	0.57 (1)	0.0	1.03	0.0	1.28	0.93 (1)	0.134	1.187

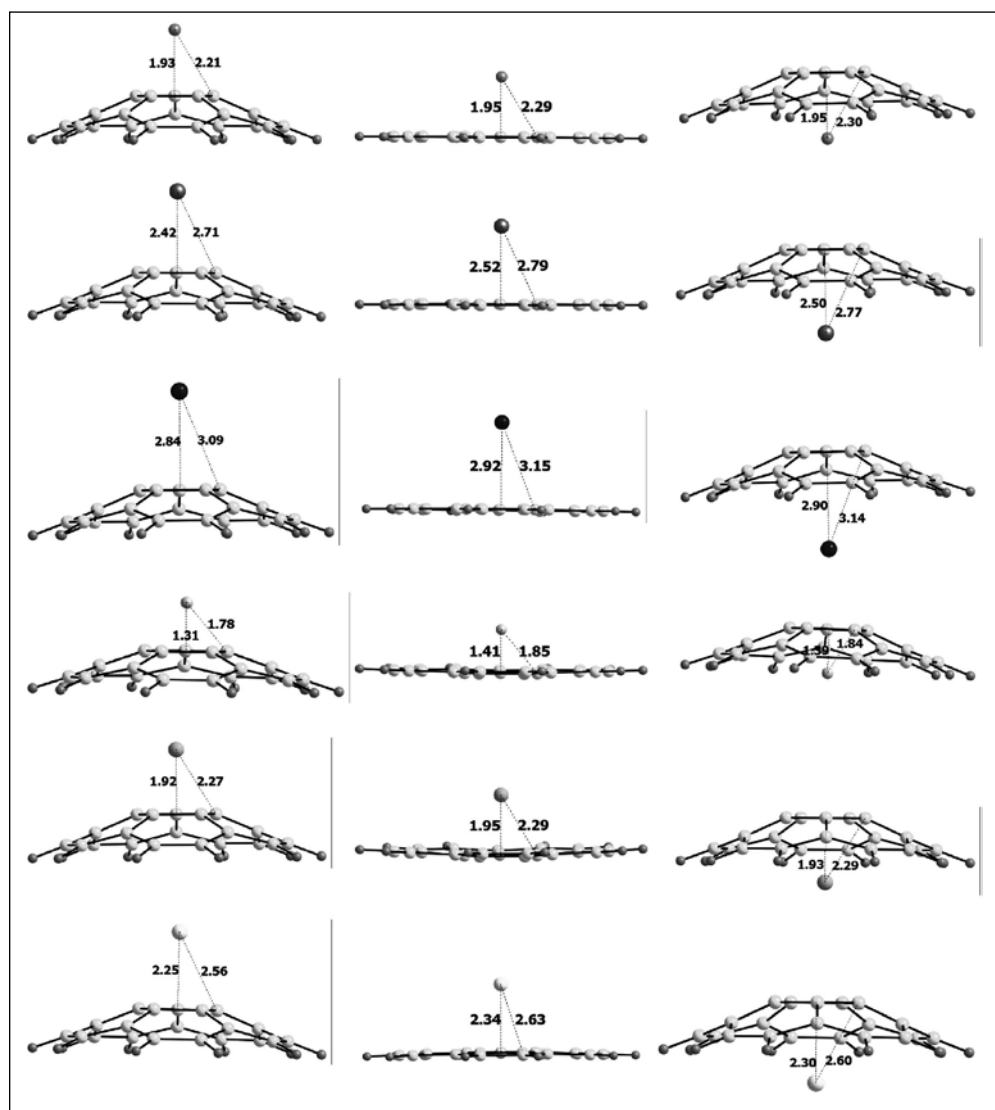


Figure 1. The optimized geometries of the metal ion-corannulene complexes in three different conformations: (a) metal ions bound on the convex plane, (b) the metal ions are on the planar surface representing the transition state, and (c) the metal ions bound on the concave face.

In the case of corannulene the dopants are allowed to interact via a η^5 co-ordination on the central pentagonal ring and through η^6 co-ordination on the peripheral six member rings. It needs a mention that no local minima on the bridge site (η^2) were observed. The lowest energy structures of the M^+ -corannulene complexes are given in Fig.1 and the energetics are listed in table 1. In general it was observed that the η^5 co-ordinated site on the convex face in the most preferred site of adsorption for all the six cations considered in this study. In the case of Li⁺, Na⁺ and K⁺, the metal ions favor the η^5 co-ordinated site on the central ring of the corannulene on the convex surface and are bound at an equilibrium distance of 1.93 Å, 2.42 Å and 2.84 Å respectively. It is further noticed that concave bound cation- π complexes are slightly elongated. The dications, Be²⁺, Mg²⁺ and Ca²⁺ ions, are bound on the convex face of corannulene at an equilibrium distances of 1.31 Å, 1.92 Å and 2.25 Å via η^5 co-ordination. The η^6 co-ordinated monocation complexes on the six membered rings along the

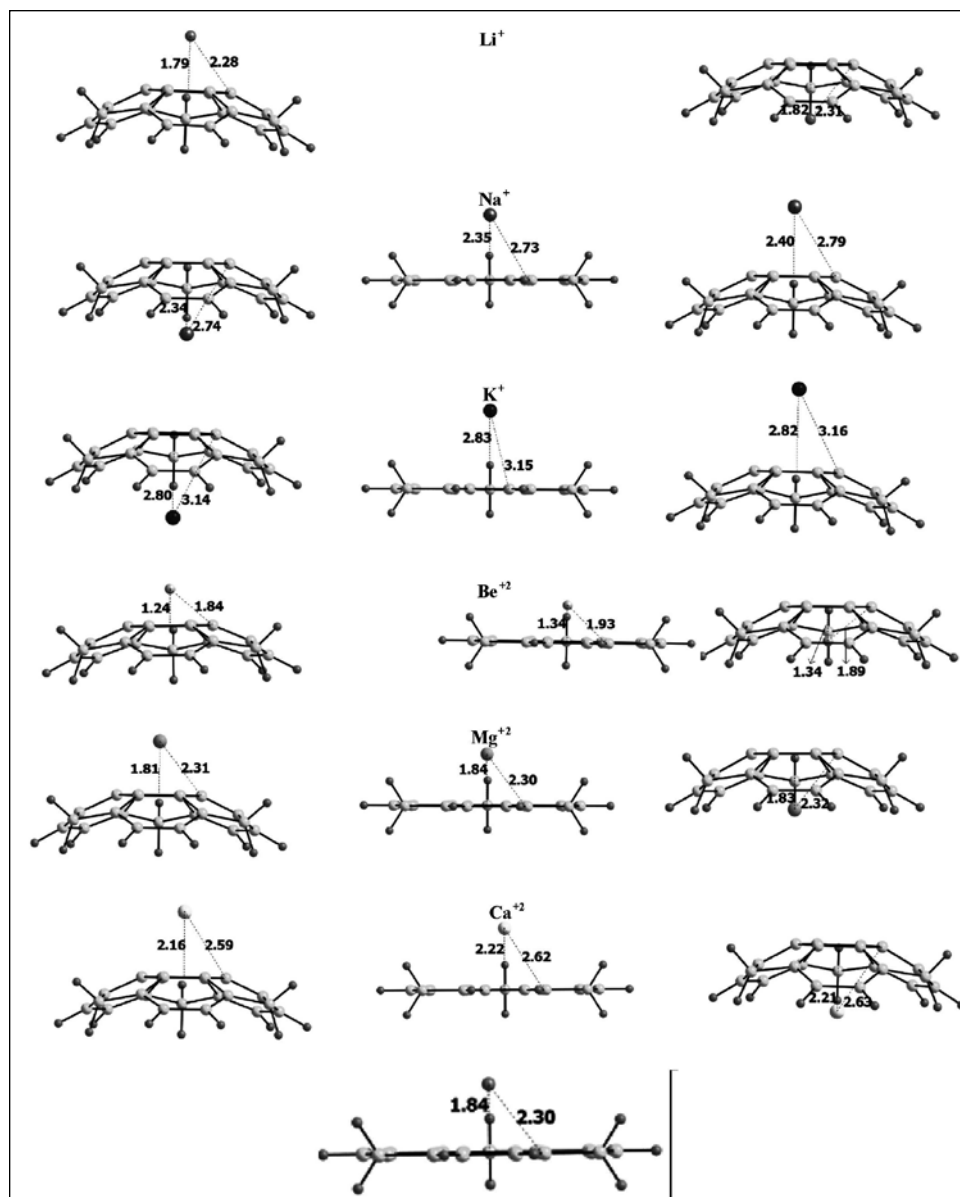


Figure 2. Geometries of the metal atom (M^+/M^{2+}) bound complexes on the (a) convex face (b) Transition state and (c) concave face over the six-member ring of sumanene

rim of the bowl were found to be stable on the PES, but higher in energy.

In case of sumanene, three preferential adsorption sites on each faces were observed, which includes (i) the η^6 site on the central six membered ring (ii) the η^6 site on the outer-rim six membered ring and (iii) η^4 coordination over the five member ring. No local minima on the bridge site (η^2), was observed with the initial structure rearranging to one of the higher coordinated geometries. Moreover, we notice that unlike corannulene, the preferential binding face of sumanene is highly sensitive to the size of the metal ion (Figure 2 and Table-1). For example, while the smaller ions (~ 114 pm) like Be^{2+} , Mg^{2+} , Ca^{2+} prefer to bind

at the η^6 site on the convex face of the central six membered ring, the larger cations like Na^+ and K^+ prefer to bind on the concave face of the sumanene. However, for Li^+ , both the faces seem to be equally probable with a slight preference towards the convex face. The total energy difference between both faces is found to be very small (~ 0.01 eV). While the equilibrium distance of the mono cations from the concave surface is found to be 2.34 Å and 2.80 Å for the Na^+ and K^+ respectively, Li^+ binds to the convex surface at a distance of 1.79 Å. It needs a further mention that the two initial structures, wherein K^+ and Na^+ are bound to the rim-six member ring or the five member ring on the concave face collapsed to the geometry similar to the η^6 site on the central six membered ring, giving confidence in the search of the preferential adsorption sites. The Be^{2+} , Mg^{2+} and Ca^{2+} ions are bound at an equilibrium distance of 1.24 Å, 1.81 Å and 2.16 Å through η^6 co-ordination to the central six-member ring on the convex face of sumanene. The metal ions were found to bind over the five member rings on the rim of sumanene through η^4 fashion since the carbon atom at the vertex is fully saturated and does not participate in bonding.

The η^4 co-ordinated cation complexes were found to be local minima on the PES, but higher in energy. Vibrational frequency calculations were carried out on all the optimized structures to ensure them to be stationary points on their respective PES. From these results it can be inferred that the bowl-depth i.e., the curvature of the bucky bowls and the size of the metal ion play a very crucial role to decide the favored binding site. Further analysis on the effect of the metal ion complexation has been carried out by looking at the bowl depth/curvature and bowl-to-bowl inversion barrier of the buckybowls [fig. 2]. A general increase in the bowl-depth was observed in case of both the bucky bowls, the larger the metal ion size, the deeper was the bowl depth. K^+ and Ca^{2+} exhibited

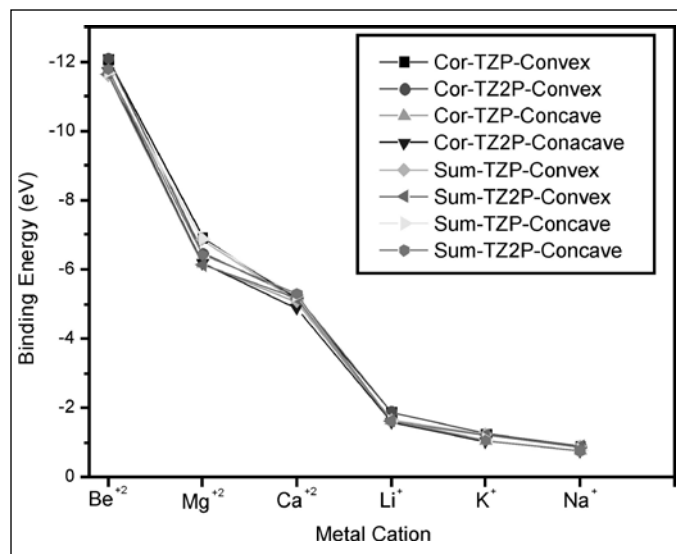


Figure 3. The binding energies of the M^+/M^{2+} bound complexes of the corannulene and sumanene molecules obtained at the BLYP level using TZP and TZ2P basis sets.

the deepest bowl depth among the mono and the di-cations respectively (Table 2).

3.2 Binding Energies

The binding energy of the mono-cations (Li^+ , Na^+ and K^+) and di-cations (Be^{2+} , Mg^{2+} and Ca^{2+}) with the corannulene and sumanene is calculated by eq.1 and the energetics are listed in Table 1. Qualitatively, the trend in the binding energies obtained using the TZP and a TZ2P basis set is same [Fig. 3]. However, the binding energies are over-estimated when TZP basis set was used, emphasizing the importance of employing TZ2P quality basis set. For corannulene, the binding to the convex surface is more favored compared to the concave surface. The dications are found to bind with corannulene better than the mono cation. For example, while the binding energy of Be^{2+} , Mg^{2+} and Ca^{2+} ranges from 12.08 eV to 5.15 eV, for K^+ to Li^+ this ranges varies from 1-2 eV. For sumanene, BE of the metal ions bound on the convex surface is found to follow $\text{Li}^+ < \text{Ca}^{2+} < \text{Mg}^{2+} < \text{Be}^{2+}$ trend, while for concave bound ions the trend is $\text{K}^+ < \text{Na}^+$. It is further observed that the binding strength of the M^+ -sumanene complexes is weaker as compared to the corannulene, implying that the cations are bound more strongly on flatter surfaces. To summarize these results a comparison of the interaction energies of all the compounds considered in this study is given in Figure 3. Based on the results it is envisaged that two factors are responsible for the binding pattern and binding energies (i) the curvature of the bucky-bowls fragments and (ii) the electronic polarization caused by the binding metal ions. The electrostatic potential surface has been

generated in order to map the surface of the bucky bowls. The bowls seem to be more negative on the outside face than the inside face [20], and have large dipole moment pointing towards the concave side. This factor favors the convex face for binding, which is indeed manifested for the smaller cations. However, larger cations like Na^+ and K^+ interact with a larger area on the π - surface through polarization interaction and tend to favor binding on the concave face. So, in contrast to the preferential η^2 binding of small metal ions over C_{60} [30], which was attributed to the unfavorable orientation of the p_z orbitals of the rings for the binding to the metal ion at either the η^5 or η^6 ring sites, higher coordinated binding sites on the corannulene/sumanene surfaces seem to be preferred. This can be ascribed to the less curvature of corannulene and sumanene as compared to C_{60} . In order to rationalize the binding energy trend of the metal ions we have calculated the polarizability (charge/radius) of the metal ions that are considered in the present study. The polarizability of the cation follows the trend of $\text{Be}^{2+} > \text{Mg}^{2+} > \text{Ca}^{2+} > \text{Li}^+ > \text{Na}^+ > \text{K}^+$. A good correlation between the polarizability of the metal ion and its binding strength was observed, with the higher polarizing metal atom binding to the π -system strongly. The present observation further substantiates the importance of polarizability in defining the metal- π interactions.

3.3 Bowl to Bowl inversions

The curved conjugated structures of hydrocarbons are known to play an important role to study the electrical conductance [31]. Therefore, locking the bowl structure of corannulene has been a focus of interest to underscore its electrical behavior. In order to assess the effect of the binding of the metal ion on the inversion barrier of the bucky bowls, the transition states during the bowl-to-bowl inversion of the bare and metal ion bound buckybowls were obtained and frequency calculations were carried out to establish their nature on the PES. The flipping of the bare bucky bowl is known to pass through a planar intermediate as the transition state. The structural parameters of the metal-ion bound TS are given in Fig.1 and 2 and the bowl-to-bowl inversion barriers are listed in Table 2. It is clear that metal ion complexation to the bowl molecules results in increasing the bowl to bowl inversion barrier. In case of corannulene, a systematic increase in the TS barrier is observed from Li^+ to K^+ and Be^{2+} to Ca^{2+} . The inversion barrier of corannulene increases by about 0.2 eV upon Li^+ to K^+ complexation and a maximum increase of 0.14 eV in the inversion barrier is observed for Ca^{2+} . Similar trend is observed for sumanene where a systematic increase in the energy barrier of Li^+ to K^+ and Be^{2+} to Ca^{2+} was observed. Therefore, the inversion barrier corresponding to the bowl-

to-bowl inversion process is controlled mainly by metal ions bound to the bucky bowl fragments.

3.4 Charge Analysis

The Mulliken charges of the cations (Li^+ , Na^+ , K^+ , Be^{2+} , Mg^{2+} , Ca^{2+}) in various cation complexes have been computed and summarized in Table 1. It is observed that the binding strength of these cations is linearly proportional to the amount of charge transfer from the π system to the M^+ ion. In case of monovalent cations, the order of charge transferred follows $\text{K}^+ < \text{Na}^+ < \text{Li}^+$. Further, the strength of interaction decreases as the ionic radius increases from lithium to potassium. For dications, the amount of charge transfer is higher than monocation complexes. Among the dication complexes, the highest interaction energy is observed for Be^{2+} complexes. The order of charge transfer is found to be $\text{Ca}^{2+} < \text{Mg}^{2+} < \text{Be}^{2+}$.

3.5 Energy Decomposition Analysis

The interaction energy (ΔE_{int}) between the metal ions and the bucky ball fragments is further analyzed in the conceptual framework provided by Kohn-Sham molecular orbital model by decomposing the ΔE_{int} into three physically meaningful terms using the quantitative energy decomposition scheme developed by Ziegler and Rauk as implemented in ADF.

$$\Delta E_{\text{int}} = \Delta E_{\text{elstat}} + \Delta E_{\text{Pauli}} + \Delta E_{\text{oi}}$$

The ΔE_{elstat} term corresponds to the classical electrostatic interaction between the unperturbed charge distributions of the fragments and is usually attractive. The destabilizing interaction comprising the steric repulsion between the occupied orbitals gives rise to Pauli repulsion (ΔE_{Pauli}). The orbital interaction ΔE_{oi} accounts for electron pair bonding, charge transfer (interaction between occupied orbitals on one moiety with unoccupied orbitals on the other, including the HOMO-LUMO interactions) and polarization (empty/occupied orbital mixing on one fragment due to the presence of another fragment). The bond energy decomposition of all the lowest energy configuration of the complexes has been summarized in Table 3. It is seen that while the Pauli repulsion is destabilizing, the electrostatic and orbital interactions contribute to the overall stability of the complexes. Quantitatively it is observed that orbital interactions contribute majorly towards the bonding energy in all the cation-complexes and the degree of orbital contribution to the total stabilizing interaction is a qualitative function of the polarizability of the respective cation in their respective groups. While the orbital interaction is found to be maximum for Li^+ -corannulene, with a contribution of ~86% to the stabilizing energy, it contributes 71% and 64%

for Na^+ and K^+ complexes, respectively. In case of dication-corannulene complexes, the orbital contribution is about 96%-84% as we go down the group (Be^{2+} to Ca^{2+}) with a maximum for the Be^{2+} -corannulene complex. Similar trend was observed in case of metal complexes of sumanene. For the mono cations-sumanene complexes the orbital contribution was observed to be approximately 89%, 75% and 66% for Li^+ , Na^+ and K^+ respectively, but for dications the orbital contribution is found to be 97% to 95% of the stabilizing energy (table-3).

4. Conclusions

In this work, we present the density functional theory based analysis of M^+ -Sumanene/Corannulene complexes, focusing on the ground state geometric and electronic structures. The structural preference of the binding faces of the metal ions with the respective bucky bowls depends on the size of the cation. While in case of corannulene the binding to the convex surface is more favored, for sumanene, the preferential binding face of the metal ions is highly sensitive to the size of the metal ion. While the smaller ions (Li^+ , Be^{2+} , Mg^{2+} and Ca^{2+}) prefer to bind to the convex surface, the larger cations Na^+ and K^+ prefer to bind to the concave surface. The binding energy is found to follow $\text{Be}^{2+} > \text{Mg}^{2+} > \text{Ca}^{2+} > \text{Li}^+ > \text{Na}^+ > \text{K}^+$ trend, wherein a good qualitative correlation between the polarizability of the ion and BE was observed; with the highly polarizing metal atom binding to the π -system strongly. The bowl-to-bowl inversion barrier is controlled mainly by metal ions bound to the bucky bowl fragments leading to an increase in the inversion barrier. Bond decomposition analysis shows that the charge transfer and polarization interactions contribute mainly to the overall stabilizing character of the pre-relaxation fragment interactions.

Acknowledgements:

The authors wish to thank the members of the Computer Division, BARC for the supercomputing facility.

References:

1. J. C. Ma, D. A. Dougherty, *Chem. Rev.*, **97**, 1303 (1997).
2. S. K. Burley, G. A. Petsko, *FEBS Lett.*, **203**, 139 (1986); D. A. Dougherty, *Science* (1996); 271, 163, N. S. Scrutton, A. R. C. Raine, *Biochem. J.*, **319**, 1 (1996).
3. J. L. Sussman, M. Harel, F. Frolow, C. Oefner, A. Goldman, L. Toker, L. Silman, *Science*, **256**, 872 (1991); A. R. Ortiz, T. Pisabarro, J. Gallego, F. Gago, *Biochemistry*, **31**, 2887 (1992); A. R. Ortiz, T. Pisabarro, J. Gallego, F. Gago, *J. Med. Chem.*, **36**, 1866 (1993); J. L. Galzi, F. Revah, A. Bessis, J. P. Changeux, *Annu. Rev. Pharmacol.*, **31**, 37 (1992).
4. D. A. Stauffer, R. E. Barrans, Jr., D. A. Dougherty, *Angew. Chem. Int. Ed. Engl.*, **29**, 915 (1990); A. McCurdy, L.S. Jiménez, D. A. Stauffer, D. A. Dougherty, *J. Am. Chem. Soc.*, **114**, 10314 (1992); Z. Shi, C. J. Butel, J. H. Griffin, *Proc.*

- Natl. Acad. Sci. USA, **91**, 7370 (1994); L. Heginbotham, R. MacKinnon, *Neuron*, **8**, 483 (1992).
5. T. J. Shepodd, M. A. Petti, D. A. Dougherty, *J. Am. Chem. Soc.*, **108**, 6085 (1986); T. J. Shepodd, M. A. Petti, D. A. Dougherty, *J. Am. Chem. Soc.*, **110**, 1983 (1988); M. A. Petti, T. J. Shepodd, R. E. Barrans, D. A. Dougherty, *J. Am. Chem. Soc.*, **110**, 6825 (1988); R. Arnecke, V. Bohmer, R. Cacciapaglia, A. D. Cort, L. Mandolini, *Tetrahedron*, **53**, 4901 (1997).
 6. T. J. Seiders, K. K. Baldrige, J. M. O'Connor, J. S. Siegel, *J. Am. Chem. Soc.*, **119**, 4781 (1997).
 7. P. A. Vecchi, C. M. Alvarez, A. Ellern, R. J. Angelici, A. Sygula, R. Sygula, P. W. Rabideau, *Angew. Chem. Int. Ed.*, **43**, 4497 (2004).
 8. C. M. Alvarez, R. J. Angelici, A. Sygula, R. Sygula, P. W. Rabideau *Organometallics*, **22**, 624 (2003).
 9. J. S. Siegel, K. K. Baldrige, A. Linden, R. Dorta, *J. Am. Chem. Soc.*, **128**, 10644 (2006); B. Zhu, A. Ellern, A. Sygula, R. Sygula, R. J. Angelici *Organometallics*, **26**, 1721 (2007).
 10. M. A. Petrukhina, K. W. Andreini, V. Mack, L. T. Scott *Angew. Chem.*, **115**, 3497 (2003); *Angew. Chem. Int. Ed.*, **42**, 3375 (2003).
 11. M. A. Petrukhina, K.W. Andreini, L. Peng, L. T. Scott *Angew. Chem.*, **116**, 5593 (2004); *Angew. Chem. Int. Ed.*, **43**, 5477 (2004); M. A. Petrukhina, Y. Sevryugina, A. Yu. Rogachev, E. A. Jackson, L. T. Scott *Organometallics*, **25**, 5492 (2006); M. A. Petrukhina *Coord. Chem. Rev.*, **251**, 1690 (2007).
 12. D. Caraiman, G. K. Koyanagi, L. T. Scott, D. V. Preda, D. K. Bohme, *J. Am. Chem. Soc.*, **123**, 8573 (2001).
 13. M. A. Petrukhina, Y. Sevryugina, A. Yu. Rogachev, E. A. Jackson, L. T. Scott, *Angew. Chem.*, **118**, 7366 (2006); *Angew. Chem. Int. Ed.*, **45**, 7208 (2006).
 14. A. Sygula, P. W. Rabideau, *J. Chem. Soc. Chem. Commun.*, 2271 (1994); J. Plater, H. S. Rzepa, F. Stoppa, S. Stossel, *J. Chem. Soc. Perkin Trans. 2*, 399 (1994).
 15. Y. Kameno, A. Ikeda, Y. Nakao, H. Sato, S. Sakaki, *J. Phys. Chem. A*, **109**, 8055 (2005).
 16. T. Amaya, H. Sakane, T. Hirao, *Angew. Chem. Int. Ed.*, **46**, 8376 (2007).
 17. H. Sakane, T. Amaya, T. Moriuchi, T. Hirao, *Angew. Chem. Int. Ed.*, **48**, 1640 (2009).
 18. T. Amaya, W.-Z. Wang, H. Sakane, T. Moriuchi, T. Hirao, *Angew. Chem. Int. Ed.*, **49**, 403 (2010).
 19. K. K. Baldrige, J. S. Siegel, *J. Am. Chem. Soc.*, **121**, 5332 (1999); Y.-T. Wu, T. Hayama, K. K. Baldrige, A. Linden, J. S. Siegel, *J. Am. Chem. Soc.*, **128**, 687 (2006); L. T. Scott, H. E. Bronstein, D. V. Preda, R. B. M. Ansems, M. S. Bratcher, S. Hagen, *Pure Appl. Chem.*, **71**, 209 (1999).
 20. F.-G. Klärner, J. Panitzky, D. Preda, L. T. Scott, *J. Mol. Model.*, **6**, 318 (2000); S. Melchor, J. A. Dobado, A. J. Larsson, J. C. Greer, *J. Am. Chem. Soc.*, **125**, 2301 (2003).
 21. M. V. Frash, A. C. Hopkinson, D. K. Bohme, *J. Am. Chem. Soc.*, **123**, 6687 (2001).
 22. R.C. Dunbar *J. Phys. Chem. A*, **106**, 9809 (2002).
 23. U. D. Priyakumar, G. N. Sastry, *Tetrahedron Lett.*, **44**, 6043 (2003); U. D. Priyakumar, M. Punnagai, G. P. K. Mohan, G. N. Sastry, *Tetrahedron*, **60**, 3037 (2004).
 24. A.K. Kandalam, B.K. Rao, P. Jena, *J. Phys. Chem A*, **109**, 9220 (2005).
 25. Amsterdam Density Functional (ADF) Package, Scientific Computing and Modelling NV (SCM), Theoretical Chemistry, Vrije Universiteit, Amsterdam, The Netherlands. Available via the Internet at [http:// www.scm.com](http://www.scm.com), C. Fonseca Guerra, J. G. Snijders, G. te Velde, E. J. Baerends, *J. Theor. Chem. Acc.*, **99**, 391 (1998); G. te Velde, F. M. Bickelhaupt, S. J. A. van Gisbergen, C. Fonseca Guerra, E. J. Baerends, J. G. Snijders, T. Ziegler, *J. Comput. Chem.*, **22**, 931 (2001).
 26. A.D. Becke, *Physical Review A*, **38**, 3098 (1988); C. Lee, W. Yang, R.G. Parr, *Physical Review B*, **37**, 785 (1988).
 27. J. G. Snijders, E. J. Baerends, P. Vernooijs, *At. Data Nucl. Data Tables*, **26**, 483 (1982).
 28. K. Morokuma, *J. Chem. Phys.*, **55**, 1236 (1971).
 29. T. Ziegler, A. Rauk, *Theor. Chim. Acta*, **46**, 1 (1977); T. Ziegler, A. Rauk, *Inorg. Chem.*, **18**, 1558 (1979); T. Ziegler, A. Rauk, *Inorg. Chem.*, **18**, 1755 (1979).
 30. J. R. Rogers, D. S. Marynick, *Chem. Phys. Lett.*, **205**, 197 (1993); H. Fujimoto, Y. Nakao, K. Fukui, *J. Mol. Struct.*, **300**, 425 (1993).
 31. D. M. Forkey, S. Attar, B. C. Noll, R. Koerner, M. M. Olmstead, A. L. Balch, *J. Am. Chem. Soc.*, **119**, 5766 (1997); K. Imamura, K. Takimiya, Y. Aso, T. Otsubo, *Chem. Commun.*, 1859 (1999).



Mr. C. Rajesh joined Bhabha Atomic Research Centre as a scientific officer in 2003 after graduating through 46th batch of training school of BARC. Since then he has been actively involved in the field of computational chemistry. At present he is working on theoretical studies of small clusters deposited on oxide surfaces and their catalytic behavior.



Dr. Chiranjib Majumder joined Chemistry Division, Bhabha Atomic Research Centre as a scientific officer in 1992 after graduating through 35th batch of training school of BARC. He received his Ph.D. degree in 2000. His current research interest is to design novel materials for catalysis by tuning the electronic properties of nano-materials and to underscore the mechanism of cluster-molecule interactions on a support matrix

Achievements, honours and awards received by the SMC members

Name of the member and affiliation	Name of the award/honour	Conferred by
Prof. Bhalchandra M. Bhanage Institute of Chemical Technology, Mumbai, India.	Fellow of the Royal Society of Chemistry, UK	Royal Society of Chemistry, UK
Ms. Lagnamayee Mohapatra, IMMT, Bhubaneswar, Odisha, India	DST-DFG awards for participation in the "Meeting of Nobel Laureates & students" held on Lindau, Germany	DST & German Research Foundation.
Mr. Muhammad Faisal PES Institute of Technology- Bangalore	Ph. D in physics	Visvesvaraya Technological University, Belgaum,
Dr. K. Nagarajan, Director, Chemistry Group, IGCAR	MRSI Medal 2013	Materials Research Society of India, Bangalore
Dr (Ms) Bina N. Wani Chemistry Division, BARC	NETZSCH - ITAS Award 2013	Indian Thermal Analysis Society
Dr. S. M. Yusuf, Solid state Physics Division, BARC, MUMBAI	P. K. Iyengar memorial award for excellence in experimental physics, 2012	The Indian Physics Association
Dr. Sarat Chandra Das, Former Principal and Head of the department of Chemistry, Salipur College, Salipur, Orissa	Professor V.S.R.Gupta chemistry teacher of the year award	Orissa chemical society, Orissa
Dr. Kartik N. Shinde, N.S.Science and Arts College, Bhadrawati,	International Association of Advanced Materials (IAAM) Scientist Award 2013	Advanced Materials World Congress-2013, İzmir, Turkey
Dr. Sandip Dey, Chemistry Division, BARC	Scientific & Technical Excellence Award	Department of Atomic energy
Dr. Vinod Kumar Tiwari, Department of Chemistry, Banaras Hindu University	1 st Tatva Scientist of the Year Award-2014	International Academy of Physical Sciences
Dr. D. Debabrata Chattaraj PDD, BARC	Mettler Toledo Best Oral Presentation Award	Indian Thermal Analysis Society

Printed by:

Ebenezer Printing House

Unit No. 5 & 11, 2nd Floor, Hind Service Industries

Veer Savarkar Marg, Shivaji Park Sea-Face, Dadar (W), Mumbai - 400 028

Tel.: 2446 2632 / 2446 3872 Tel Fax: 2444 9765 E-mail: outworkeph@gmail.com

In this issue

Feature articles	Page No.
1. Carbon Composite Materials for high temperature Structural applications <i>L. M. Manocha</i>	1
2. Micro to Macroporous Carbon Materials <i>Satish M. Manocha</i>	8
3. Chemical Vapor Deposited Diamond Thin Films: A Brief Overview on Synthesis and Characterization <i>J. Nuwad, Dheeraj Jain, C. G. S. Pillai and V. Sudarsan</i>	15
4. Raman Spectroscopic Studies of Carbon Related Materials <i>Dattatray J. Late and Mukesh Pandey</i>	26
5. Silicon Carbide Research and Development in Nuclear Industry: Silicon Carbide on Graphite Rod by Induction Assisted Chemical Vapor Deposition process using Hexamethyldisilane (HMDS) as a Single Source. <i>J. Selvakumar, K. Ramadurai, D. Sathiyamoorthy</i>	35
6. Novel Carbon Composites for Nuclear Application <i>Ramani Venugopalan, Kinshuk Dasgupta, Mainak Roy and A. K. Tyagi</i>	46
7. Structures and energetics of alkali and alkaline earth metal ion complexes of sumanene and corannulene: A systematic understanding of cation-π interactions <i>Chinagandham Rajesh and Chiranjib Majumder</i>	52

Published by

Society for Materials Chemistry

C/o. Chemistry Division Bhabha Atomic Research Centre, Trombay, Mumbai, 400 085 (India)

E-mail: socmatchem@gmail.com,

Tel: +91-22-25592001